

LASER INDUCED FLUORESCENCE  
AS A PROBE OF DETAILED REACTION DYNAMICS:  
CONVENTIONAL TECHNIQUES AND  
FOURIER TRANSFORM DOPPLER SPECTROSCOPY

by

EDMOND JOSEPH MURPHY, JR.  
B.S., Boston College  
(1976)

SUBMITTED IN PARTIAL FULFILLMENT OF  
THE REQUIREMENTS FOR THE  
DEGREE OF  
DOCTOR OF PHILOSOPHY  
at the  
MASSACHUSETTS INSTITUTE OF TECHNOLOGY  
May 1980

Copyright: Massachusetts Institute of Technology 1980

Signature of Author

Department of Chemistry  
May 1980

Certified by

James L. Kinsey  
Thesis Supervisor

Accepted by

Glenn A. Berchtold  
Chairman, Department Committee on Graduate Students

ARCHIVES  
MASSACHUSETTS INSTITUTE  
OF TECHNOLOGY

JUN 10 1980

LIBRARIES

This doctoral thesis has been examined by a committee of the Department of Chemistry as follows:

Professor Robert J. Silbey \_\_\_\_\_  
Chairman, Thesis Committee

Professor James L. Kinsey \_\_\_\_\_  
Thesis Supervisor

Professor Robert W. Field \_\_\_\_\_

LASER INDUCED FLUORESCENCE  
AS A PROBE OF DETAILED REACTION DYNAMICS:  
CONVENTIONAL TECHNIQUES AND  
FOURIER TRANSFORM DOPPLER SPECTROSCOPY

by

EDMOND JOSEPH MURPHY, JR.

Submitted to the Department of Chemistry  
in May 1980 in partial fulfillment of the requirements  
for the degree of Doctor of Philosophy

ABSTRACT

A detailed experimental investigation of energy disposal in the chemical reaction  $D(H) + NO_2 \rightarrow OD(OH) + NO$  is reported. Molecular beams and laser induced fluorescence are used to determine vibrational, rotational and fine structure partitioning in the OD(OH) product. Information theory is used to analyze the data and to extrapolate to unobserved levels. For the OD reaction we find  $\langle f \rangle = .27$  and  $\langle f \rangle = .17$  and for the OH reaction,  $\langle f \rangle = .24$  and  $\langle f \rangle = .20$ . Both reactions produce statistical spin state distributions and both preferentially populate the higher energy lambda doublet state.

Angular and velocity distributions are determined for three OD and four OH product states in the first experimental utilization of Fourier Transform Doppler Spectroscopy. The OD(OH) product is scattered very slightly forward along the initial D(H) direction in the center of mass coordinate system. The angular distributions are essentially independent of isotope and internal state and  $\langle f \rangle = 0.25$  for both reactions.

A reaction scheme which involves formation of a planar intermediate and which is consistent with all of the observed data is presented and discussed.

Thesis Supervisor: James L. Kinsey  
Title: Professor of Chemistry

To Kathy and my parents

### ACKNOWLEDGEMENTS

I wish to express my gratitude to many members of the M.I.T. Chemistry Department for their part in this work. Professor J.L. Kinsey has consistently provided necessary insight and incentive throughout my graduate student days. Professor R.W. Field cheerfully discussed many facets of this work and generously donated his time to help get me through the horrors of 5.73. Thanks go to G.S. Arnold, J.H. Brophy and W.L. Dimpfl who acclimated me to this lab and to T. Anderson, J. Cordova, C. Reiser, C.T. Rettner and A. Sinha who have humored me for the past few years. An additional note of thanks goes to Professors P. Davidovits and D.L. McFadden of Boston College who first interested me in physical chemistry and in graduate school and who have kept in contact since my graduation.

The expertise of the machine and electronics shops within the Chemistry Department and the Research Laboratory for Electronics has been very helpful.

I gratefully acknowledge the support of the John A. Lyons Memorial Fellowship.

In addition, I must thank friends outside of the M.I.T. community especially my wife, Kathy, and my parents who have supplied more than enough moral support. Finally, I acknowledge my four month old nephew, Jim; but for his timely birth, this thesis might never have been typed.

## TABLE OF CONTENTS

	<u>Page</u>
Chapter I INTRODUCTION.....	10
Chapter II APPARATUS.....	13
A. Introduction.....	13
B. Molecular Beam System.....	13
1. The Vacuum System.....	13
2. Atomic Reagent Beam Source (H,D).....	20
3. Molecular Reagent Beam Source (NO <sub>2</sub> ).....	24
C. Laser and Detection System.....	26
1. Laser Line Width.....	26
2. Etalon Position in Laser Cavity.....	30
3. Laser Path Through the Apparatus.....	34
4. Fluorescence Detection.....	34
D. Signal Processing and Data Collection.....	37
E. Apparatus Alignment.....	41
F. Operational Details.....	42
Chapter III INTERNAL STATE DISTRIBUTIONS.....	43
A. Data Acquisition and Analysis.....	43
B. Fine Structure Partitioning.....	45
C. Internal State Distributions and Information Theoretic Analysis.....	49
1. Conventional Information Theoretic Analysis.....	49
2. Relaxation Question Resolved.....	59
3. Modified Information Theoretic Analysis.....	62
4. Results of Surprisal Analysis .....	67
Chapter IV FOURIER TRANSFORM DOPPLER SPECTROSCOPY.....	74
A. Introduction.....	74
B. The Technique.....	75
1. The Doppler Effect.....	75
2. FTDS.....	76
3. Number density to fluxes; coordinate system transformation.....	77

TABLE OF CONTENTS (continued)

	<u>Page</u>
C. Data Analysis.....	81
1. Analyzing the Doppler Profiles.....	81
2. Gaussian fits to the Doppler Profiles.....	89
3. Polynomial fits to the Doppler Profiles.....	100
D. Results.....	105
1. Doppler Profile Inversion.....	105
2. Velocity Distributions.....	106
3. Average Translational Energy.....	115
4. Angular Distributions.....	121
E. Comparison to other Data.....	122
Chapter V CONCLUSIONS.....	129
A. Background.....	129
B. Reaction Scheme.....	131
C. Discussion.....	132
REFERENCES.....	135
APPENDIX A Orientation and Polarization Effects in Laser Induced Fluorescence Experiments.....	139
1. Transition Moment Dependence on Orientation and Polarization.....	139
2. Spatial Distribution of Emitted Fluorescence Intensity..	141
3. Effect of Transition Moment Orientation - Polarization Dependence on an Unoriented Sample.....	143
4. Orientation - Polarization Effects and the FTDS Experiments.....	145
APPENDIX B Computer Programs.....	147
1. Calculation of Prior Distributions.....	148
2. Doppler Normalization and Moment Calculations.....	150
APPENDIX C Suppliers of Materials.....	153
BIOGRAPHICAL NOTE.....	155

## LIST OF FIGURES

<u>Figure Number</u>	<u>Page</u>
II-1 Apparatus - Side View.....	14
II-2 Apparatus - Top View.....	16
II-3 Pumping System.....	18
II-4 H(D) Atom Source.....	21
II-5 Laser Bandwidth.....	27
II-6 Laser Cavity Schematic.....	32
II-7 Mirror System.....	35
II-8 Processing Electronics.....	39
III-1 Spin State Distribution.....	47
III-2 OD Internal State Distribution.....	50
III-3 OH Internal State Distribution.....	52
III-4 Conventional Surprisal Plots .....	57
III-5 Surprisal and Prior Plot for OD $v=0$ .....	63
III-6 Modified Surprisal Plot .....	68
IV-1 Doppler Effect Schematic.....	78
IV-2 Average Scattering Velocity Vectors.....	84
IV-3 Gaussian Data Fit for OH $R_1$ 17 (0,0).....	90
IV-4 Vector Definition.....	94
IV-5 Gaussian Fit Flux Plot for OD $R_2$ 14 (0,0).....	96
IV-6 $f(y)$ from Gaussian Fits.....	98
IV-7 Polynomial Data Fit for OD $R_2$ 14 (0,0).....	103
IV-8 Polynomial Fit Flux Plots for Four States.....	107
IV-9 Symmetry Problem Schematic.....	112
IV-10 $f(y)$ from Polynomial Fits.....	116
IV-11 Average Energy in Translation.....	119
IV-12 $f(\theta)$ from Polynomial Fits.....	123
IV-13 Haberland's Angular Distributions.....	126

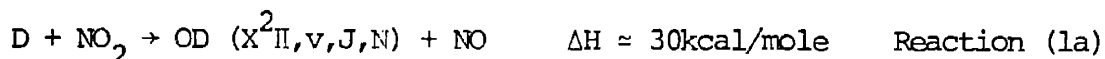


LIST OF TABLES

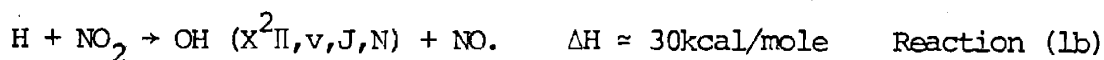
<u>Table Number</u>		<u>Page</u>
II-1	UV Laser Linewidth.....	31
III-1	Constants for Energy Level Calculations.....	56
III-2	Parameters for Conventional Surprisal Analysis .....	60
III-3	Parameters for Modified Surprisal Analysis .....	71
IV-1	Moments of Doppler Profiles.....	87
IV-2	Parameters for Polynomial Fits.....	102
IV-3	Average Translational Energies.....	118

## Chapter I - Introduction

This work represents the third and probably the last of a series of theses <sup>(1,2)</sup> produced in this laboratory which have attempted to unravel the details of energy disposal in the two simple chemical systems:



and



These studies have centered around the use of laser induced fluorescence to probe the relative probabilities for the production of OD and OH in particular rotational, vibrational, fine structure and translational energy states. These reactive systems have also been studied extensively by other techniques in other laboratories. References to this other work will be made as necessary in later chapters.

Often, the discussion herein will apply equally to Reactions 1a and 1b. As a matter of convenience, in all such sections, the symbols D and OD will be used to represent both D, H and OD, OH respectively.

The technique of laser induced fluorescence (LIF) <sup>(21,22)</sup> is by now a well documented tool in studies of molecular properties and of collisional dynamics. Our interest in the method stems from the fact that by monitoring fluorescence intensity as a function of laser wavelength we determine the product state distribution of reactive collisions and thus, obtain a handle on the reaction dynamics. Due to the high exoergicity of these reactions, a large number of vibrational-rotational states are populated and we measure a large set of probabilities which characterize the product state distribution. Information theoretic concepts <sup>(23)</sup> have been used to reduce this large data set to a small, manageable set of parameters. In principle this set of parameters provides meaningful physical insights by eliminating the inherent redundancy of the large data set. <sup>(24,25)</sup> Although the theory does suffer from a lack of generality (no given set of constraints is applicable to all reactive systems) and from a lack of

uniqueness (there is no definitive way to go from the parameters to a reaction model or vice versa), it has proven quite useful in the parameterization of experimental and theoretical data sets. Here we have used the information theory approach in a novel way to add credence to a reaction model suggested by other experimental data.

Studies of isotope effects in reactive systems are of interest because they provide additional insights into the dominant forces effecting chemical interactions. Comparison of reaction attributes among isotopic systems can determine whether energy or momentum constraints influence the system more strongly. Moreover, in going from a hydrogen to a deuterium system there is a higher density of accessible states which enables one to obtain a larger and possibly more informative data set.

This thesis also presents the first successful experiments which utilize a new technique that is closely wed to LIF. Fourier Transform Doppler Spectroscopy <sup>(15,16)</sup> ( FTDS ) takes advantage of the velocity information inherent within the Doppler profile of a single LIF spectral feature. By deconvolving this information the angle and speed distributions of reactively scattered products are determined. The ease with which this technique generates very detailed data is demonstrated. However, we have only tapped the well. With the single mode, widely tuneable, high power dye lasers currently commercially available ( Coherent, Spectra Physics, etc. ) and with the well understood technology of supersonic nozzle beam sources <sup>(8)</sup> FTDS can be used to measure heretofore unresolved details of many scattering processes. It seems that an experiment that closely specifies initial reactant translational and internal energy ( by virtue of the supersonic expansion ) and resolves the product's translational and internal degrees of freedom ( through LIF-FTDS ) is not far in the future. In fact, such a study on an inelastic scattering process has produced some preliminary results. <sup>(26)</sup>

In addition to the dependence on energetic degrees of freedom alluded to above, scattering processes can also depend strongly on the orientation of the collisional partners. This aspect of the scattering problem has been discussed in the literature and will be referred to in more detail in Chapter V. During the course of this work we have addressed the question of how one might measure the alignment of product molecules and how such consid-

erations might affect these measurements even if the molecules are not aligned. Some of this work is presented and discussed in Appendix A.

The understanding of reaction dynamics suffers to some extent in that there is a large gap between systems that are amenable to experimental studies and systems that are amenable to theoretical studies. Part of the problem arises from the inability of experimentalists to measure cross sections that are detailed enough to provide direct probes of the potential surface. The theorist must average his calculated cross sections over unspecified or unresolved reaction attributes thereby masking the influence of the potential surface. It is hoped that through techniques such as LIF-FIDS and through techniques sensitive to the orientation of reactants and products, this gap will someday be bridged.

## Chapter II - Apparatus

### IIA. Introduction

This chapter contains all details of the apparatus pertinent to both the internal state distribution measurements and to the FTDS measurements. The crossed-beam laser induced fluorescence apparatus discussed herein is a modification of a system described previously. <sup>(1,2,3)</sup> The purpose of the new design is to utilize the significant increase in beam collimation and number densities inherent in a differentially pumped source. <sup>(8,9)</sup> Thus, the major modifications are to the vacuum system and to its configuration. Other minor changes will be discussed.

Diagrams of the apparatus are shown in Figures II-1 and II-2.

### IIB. Molecular Beam System

#### 1. The Vacuum System

A schematic diagram of the entire pumping system is shown in Figure II-3. The main chamber is evacuated by an NRC 10" diffusion pump which is backed by an Edwards 330 mechanical pump. Additionally, the chamber is cryo-pumped (at Liquid Nitrogen temperature) by a chevron baffle above the diffusion pump and by a large copper plate directly opposite the  $\text{NO}_2$  source (approximately 400  $\text{cm}^2$  total of  $\text{LN}_2$  cooled surface). A 4" Stokes diffusion pump (backed by an Edwards 330 mechanical pump) provides the differential pumping for the molecular reactants. This pumping line also contains a Liquid Nitrogen cold trap which acts as a very efficient cryo-pump. A third mechanical pump (GCA-VacTorr) is used to evacuate the gas handling system and to pump condensable reactants to a removable cold trap after an experiment.

The vacuum chamber is equipped with a rotating lid, which facilitates altering the direction of propagation of the laser radiation relative to the molecular beam sources. This

Figure II-1

Cross sectional diagram of the molecular beam apparatus. For reasons of clarity, the  $\text{NO}_2$  source is not shown. It is situated behind the plane of the paper and the molecules flow toward the viewer. Other features of the apparatus are discussed in the text.

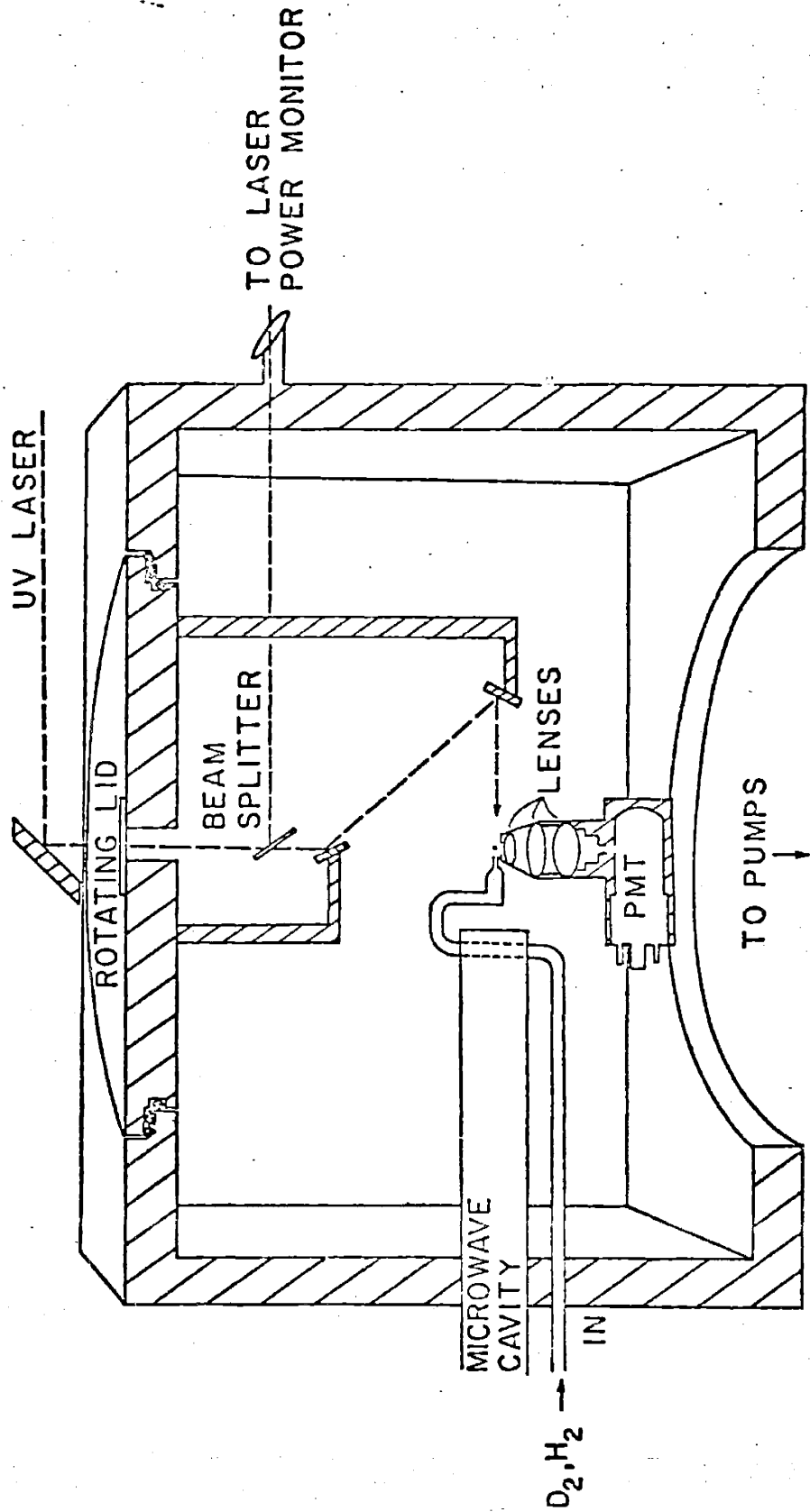


Figure II-2

Top view of the molecular beam apparatus depicting the orientation of the beam sources. Laser propagation is illustrated for one angle and the arrows indicate other propagation directions used in these experiments. See text for further discussion.



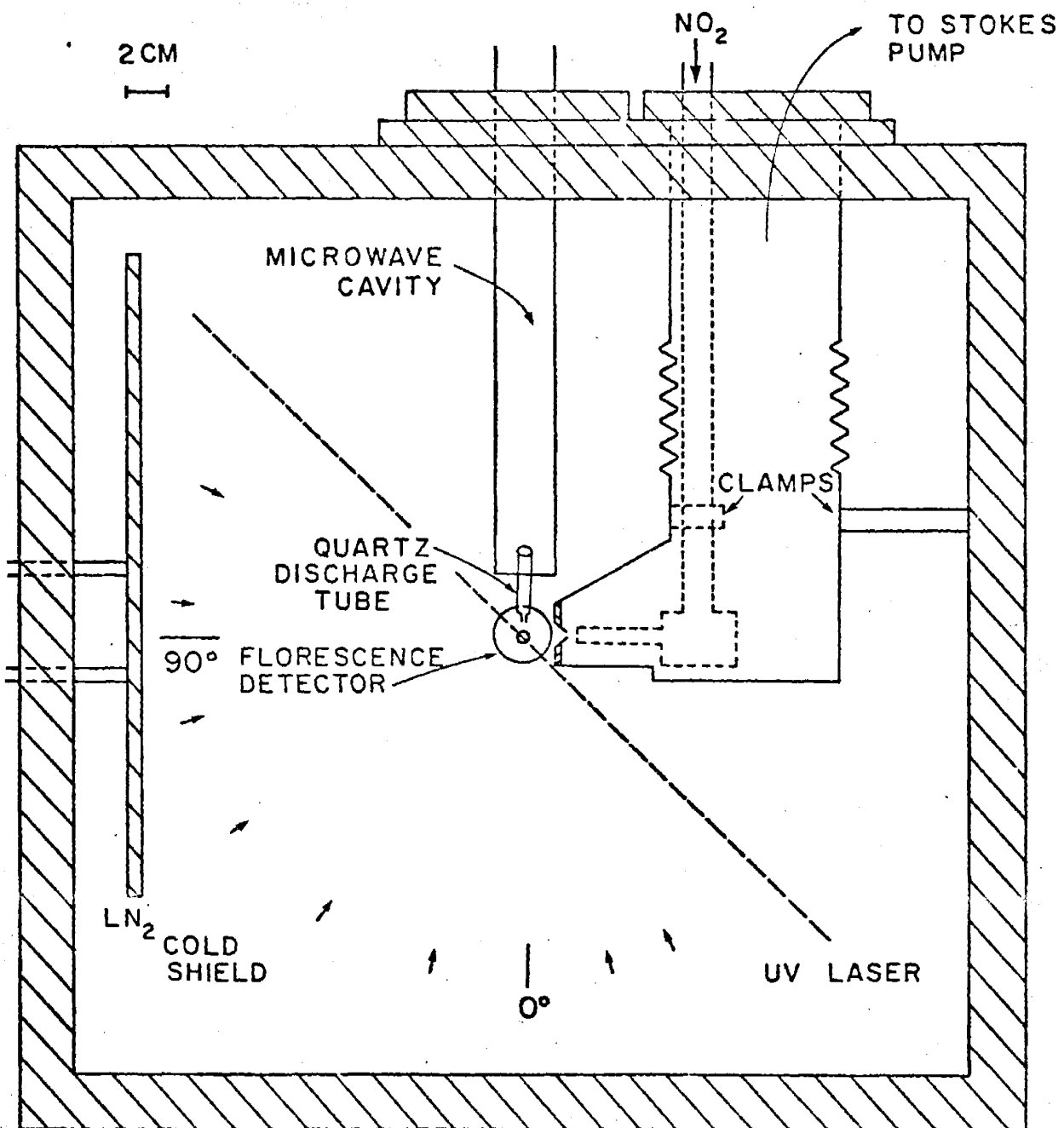
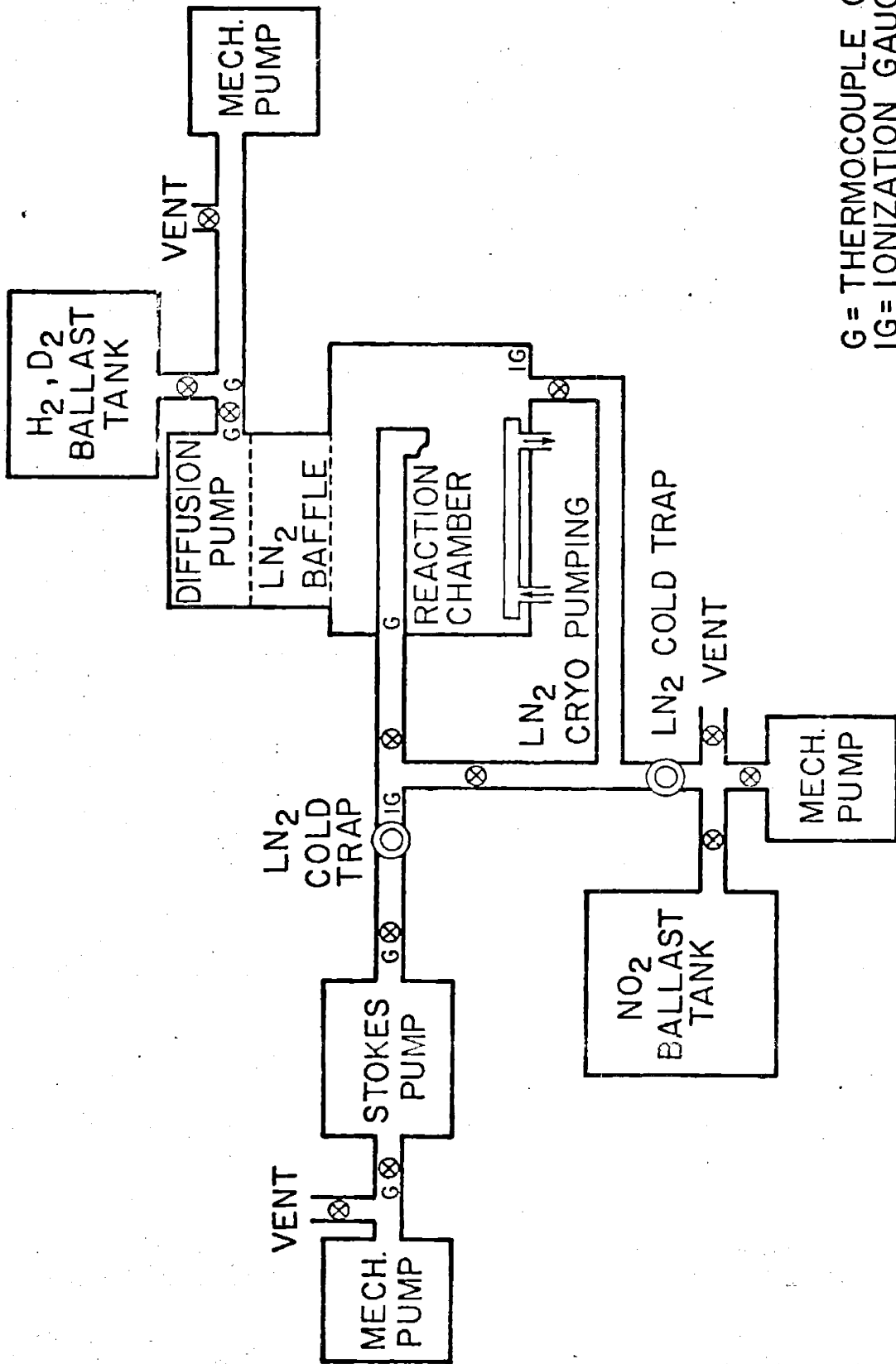


Figure II-3

Schematic diagram (not to scale) of the pumping system.



G = THERMOCOUPLE GAUGE  
 IG = IONIZATION GAUGE  
 ⊗ = VALVE

feature is discussed later in this chapter and its utility will become apparent in Chapter IV.

## 2. Atomic Reagent Beam Source ( H, D Atoms)

The microwave discharge offers a convenient means of producing intense beams of atomic, radical and metastable species without the problems of high temperature and exotic materials associated with thermal dissociation. In the case of atoms, the high degree of dissociation in the discharge can be offset by wall recombination losses downstream. Therefore, the discharge should be operated as close as possible to the source nozzle, ideally in the vacuum chamber.

The atomic source used in these experiments has been described in the literature.<sup>(4)</sup> The source (shown in Figure II-4) has been designed to maximize the flux of atomic species without relying on any extensive engineering. The source incorporates much of the "traditional wisdom" in this field into a convenient, extended cavity microwave discharge design.

The microwave cavity is a modified Evenson design<sup>(5)</sup> in which the original quarter wave resonance length is extended by adding on a suitable length of heavy walled brass tubing. Total cavity length is governed by the resonance condition

$$\frac{2\pi L}{\lambda} = \tan^{-1} \left( \frac{1}{Z_0 w C_0} \right)$$

where  $Z_0$  is the impedance,  $C_0$  the capacitance,  $\lambda$  the wavelength,  $w$  the frequency and  $L$  the cavity length. For  $Z_0 w C_0 \ll 1$ , this leads to values of  $L$  given by

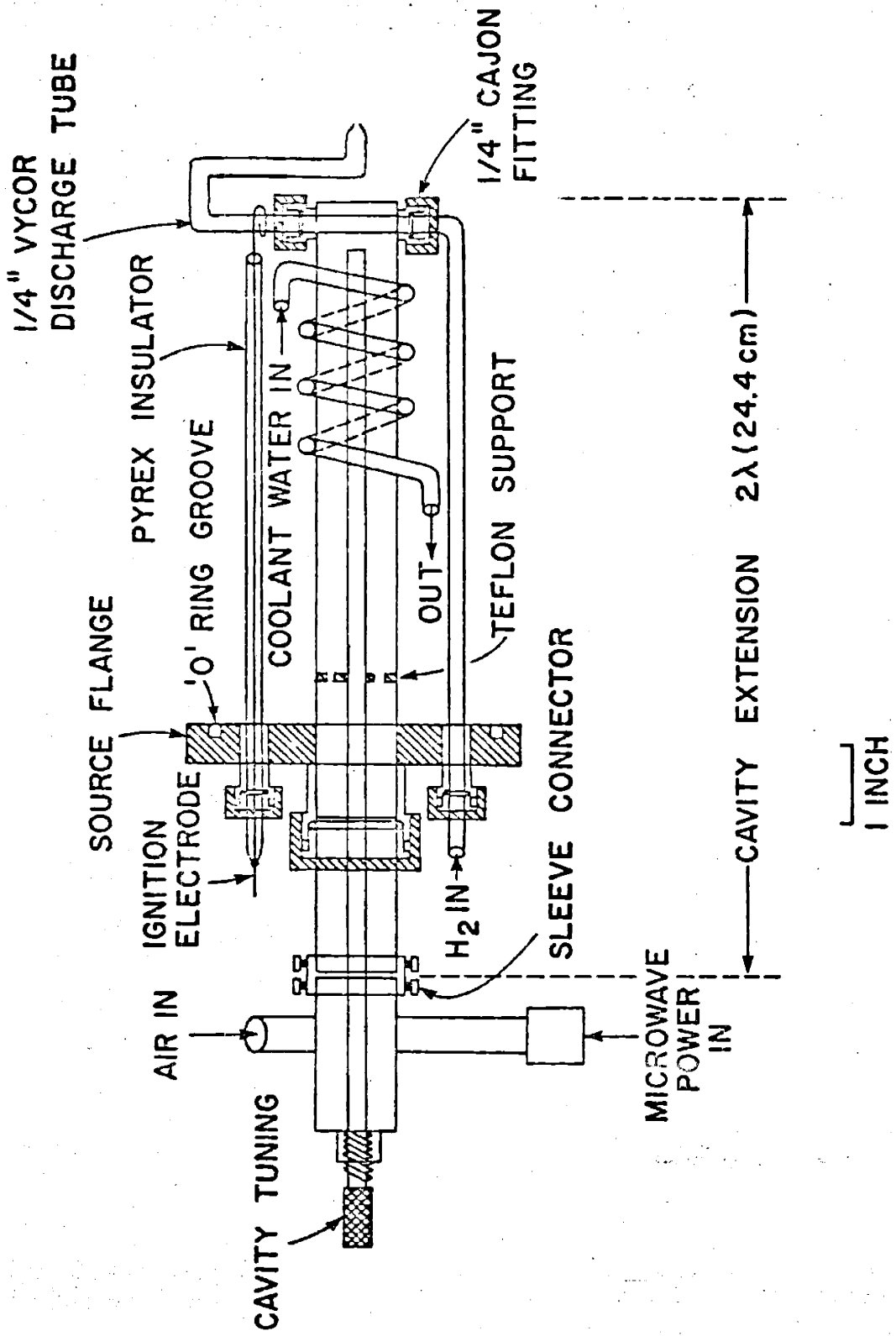
$$L = \frac{1}{2} \left( n + \frac{1}{2} \right) \quad n=0,1,2, \dots$$

The cavity length therefore can be extended by an integral number of half wavelengths to suit the apparatus.<sup>(6)</sup>

The cavity extension used here is a length of 1" diameter heavy walled brass tube connected to the standard Evenson cavity by a brass collar. The ability to break the cavity in this way is convenient in assembling the source in the flange. Tuning of the cavity is accomplished by extending the standard

Figure II-4

Extended cavity microwave discharge source assembly.



tuning stub by the same amount and supporting it along the cavity axis by a teflon spacer.

A one inch Cajon fitting is used to seal the vacuum at the source flange and two  $\frac{1}{4}$ " fittings provide the seal through which the Vycor discharge tube passes.

Stable cooling of the discharge is important since the efficiency of atom production is known to be a function of temperature of the discharge source. To this end, the cavity is cooled by a closed loop system circulating water from an ice temperature heat exchanger through a copper coil soldered around the brass cavity extension. Cooling of the Vycor discharge tube is supplemented by a flow of compressed air at a regulated constant pressure. After flowing around the discharge tube, the cooling air leaves the vacuum system via a tube soldered to the cavity end and passing through the source flange. For reasons of clarity, this is omitted in the diagram.

Microwave power is supplied by a Raytheon (PGM-10) 2450 MHZ magnetron source via a standard coaxial cable and connectors. After adjusting the cavity tuning elements the supply operates typically at 40% of full power (full power = 85 watts). The discharge is ignited remotely by the spark from a Tesla coil conducted along a copper wire to the discharge tube.

The discharge tube is constructed from 7 mm (O. D.) Vycor tubing, turned through three right angles and drawn down to a nozzle diameter of approximately 0.5 mm. The bends in the tubing act to extinguish light from the discharge which otherwise would be internally reflected in the walls of the tube and would generate unwanted background light near the phototube. Additionally, light from the discharge is screened from the detector region by a blackened sheet of aluminum foil and by coating the outside of the discharge tube with colloidal graphite.

As shown in Figure II-4, the source is mounted on one six inch diameter vacuum flange with all cavity tuning ele-

ments, power input coupling, and power connections outside the vacuum.

The discharge tube is cleaned periodically by rinsing alternately with concentrated HF and distilled water. A small gas flow is maintained through the tube at all times to minimize pump oil contamination. Additionally, it is found that bubbling the  $H_2(D_2)$  through water upstream from the discharge enhances atom production. The discharge is typically backed by a pressure of 1 to 5 torr  $H_2(D_2)$  in a ballast tank.

In comparison to previous sources used in this laboratory, this source requires less care and cleaning and produces at least a factor of 50 increase in atomic hydrogen flux.

### 3. Molecular Reagent Beam Source ( $NC_2$ )

As previously mentioned, the molecular reagent source was built to take advantage of the improved flux densities and collimation typical of differentially pumped sources. It consists of two parts, one of which carries the reagent to the nozzle and the second of which provides the differential pumping. The source is shown in Figure II-2.

The reactant gas handling system is constructed entirely of stainless steel. The gas flows from a ballast tank, through a flexible bellows and into a  $\frac{1}{2}$  inch C.D. heavy walled tube which passes into the vacuum chamber through a  $\frac{1}{2}$  inch Cajon fitting. This length of tubing also helps to support the differentially pumped section. This tube is a tight press fit into a machined block of stainless steel. A  $\frac{1}{4}$  inch tube is silver soldered into this block perpendicular to the  $\frac{1}{2}$  inch tube. Finally, a cap is soldered on to the end of the  $\frac{1}{4}$  inch tube. A .5 mm hole (.5 cm length) drilled in the center of this cap serves as the source orifice. Additionally, a tapped hole (4-40) positioned at the rear of the block (coaxial with the nozzle) serves as an important alignment aid (see Section II-E).

The stainless steel block and nozzle assembly are heated



by passing current through conventional heating tape wrapped around the oven or through coaxial heating wire silver soldered to the oven. Temperature control is effected by an iron-constantan thermocouple held into the back end of the oven with a set screw. Typical operating temperature of the oven is 60°C. Electrical feedthrus are mounted on the same flange as the Cajon feedthru.

The differential pumping system is mounted on an eight inch brass flange which provides ports for (1) the molecular source flange, (2) an outlet to the Stokes pump and (3) the atom source flange. The differentially pumped chamber which extends from this flange into the main chamber consists of three sections. First, a length of three inch copper pipe is soldered to the brass flange at the port for the molecular source flange. A two inch copper elbow is soldered around a hole cut in the side of this pipe and to the outlet port on the brass flange. This provides a connection to the Stokes pumping system. Next, three inch stainless steel bellows tubing is attached to the end of the copper pipe (tight press fit, secured by set screws) in order to allow flexibility in positioning the final source assembly.

The third section, machined from aluminum, is attached to the bellows by an o-ring seal. This section contains a clamp to which the  $\frac{1}{2}$  inch tube carrying the reactant is attached and provides the housing to which the collimator is attached. This section is fitted with a removable aluminum cap which allows access to the oven and alignment hole. The entire assembly is supported from a wall of the vacuum chamber by a clamp fitted around this section.

The collimator is screwed into a tapped hole at the front of this final section. This arrangement allows ease in changing the collimator orifice diameter. The collimators themselves are machined from aluminum. An orifice diameter of approximately 0.5 mm was used in all experiments. The

nozzle to collimator distance is approximately 0.5 cm.

The vapor pressure over a reservoir of liquid  $N_2O_4$  (at  $0^\circ C$ ) feeds the ballast tank through a needle valve. The pressure in the ballast tank is typically maintained between 40 and 150 torr. The pressure in the differentially pumped chamber (measured 10" from nozzle) is typically 0.1 torr. Under these source conditions, the source does not operate as a true supersonic nozzle source nor simply as an effusive source from the collimator orifice. Rather, the collimator and differentially pumped region serve to select a directional component from the intense hydrodynamic flow emanating from the source orifice.

## IIC. Laser and Detection System

### 1. Laser Line Width

The laser used in these experiments has been described in detail in two previous theses from this laboratory (1,2). Basically, a commercial laser system (Chromatix 1000 - 1050 YAG/DYE laser system) has been modified by insertion of a 1 mm, 55% reflective etalon in the dye laser cavity. This has the effect of narrowing the lasing (visible) line width to 1.21GHz FWHM as shown in Figure II-5. (See Reference 2 for a more detailed discussion.)

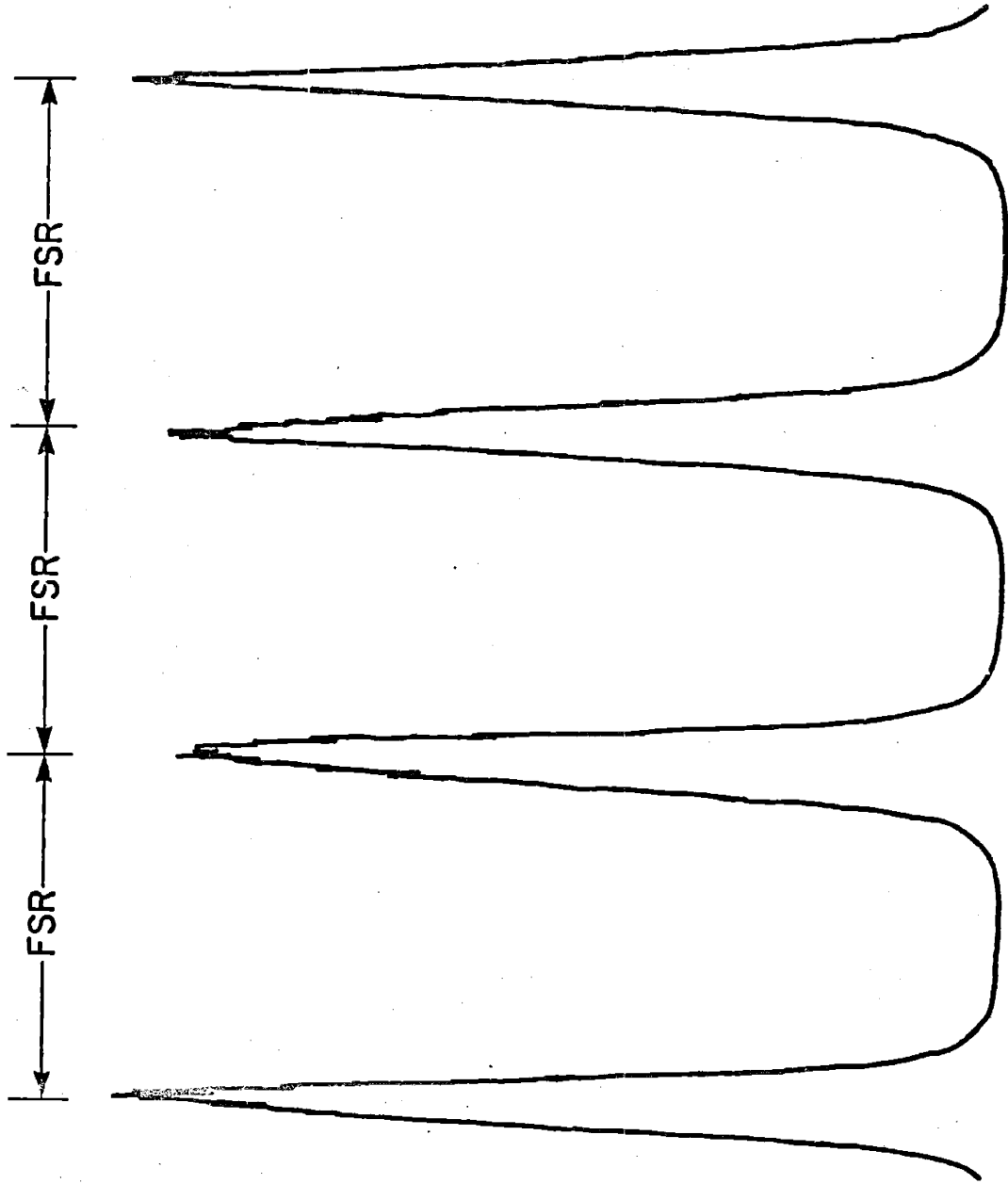
Since a spectrum analyzer capable of measuring the frequency doubled UV laser output is not available, the lineshape in the UV must be calculated. The intensity as a function of frequency,  $I(\nu_{uv})$  for the frequency doubled output is simply proportional to the square of the visible intensity, <sup>(7)</sup>  $I(\nu_{vis})$ ,

$$I(\nu_{uv}) \propto [I(\nu_{vis})]^2. \quad \text{Equation II-1.}$$

The form of  $I(\nu_{vis})$  is determined from spectrum analyzer traces to be made up of a series of spikes (separated by approximately 333 MHz) due to longitudinal cavity modes. The

Figure II-5

Repetitive visible spectrum analyzer trace of laser output. 1 mm, 55% reflective etalon in laser cavity. The trace does not resolve individual laser cavity modes. The free spectral range of the analyzer is 7.50GHZ. From this figure, the bandwidth (full width at half maximum) of the visible laser output is determined to be 1.21 GHZ.



envelope over these spikes is accurately described by a gaussian with  $\text{FWHM}_{\text{vis}} = 1.21\text{GHz}$ . Using this functional form, one can apply the following analysis to determine  $I(\nu_{\text{uv}})$ .

The Fourier series expansion of the visible intensity about  $\nu_0$  is given by:

$$i(t | \nu_0) = \sum_{\ell} \exp[-a(\ell \cdot \Delta\nu - \nu_0)^2 + i\ell \cdot \Delta\nu t] \quad \text{Equation II-2}$$

where  $\Delta\nu$  is the separation between cavity modes and  $\ell$  is the summation index over these modes ranging from  $-\infty$  to  $\infty$ .

Applying Equation II-1, we have:

$$i^2(t | \nu_0) = \sum_{\ell \ell'} \exp[-a[(\ell \cdot \Delta\nu - \nu_0)^2 + (\ell' \cdot \Delta\nu - \nu_0)^2] + i(\ell + \ell') \Delta\nu t].$$

We let  $L = \ell + \ell'$  and  $J = \ell - \ell'$  and define  $Z = \sum_J \exp\left(-\frac{a}{2} (J \cdot \Delta\nu)^2\right)$

$= 2\left(\frac{2\pi}{a}\right)^{\frac{1}{2}} \left(\frac{1}{\Delta\nu}\right)$  then we have:

$$i^2(t | \nu_0) = Z \sum_L \exp\left[-\frac{a}{2} (L \cdot \Delta\nu - 2\nu_0)^2 + iL \Delta\nu t\right]$$

$I(\nu_{\text{uv}})$  is composed of the real Fourier components of  $i^2(t | \nu_0)$ :

$$I(\nu_{\text{uv}}) = Z \exp\left[-\frac{a}{2} (L \cdot \Delta\nu - 2\nu_0)^2\right] = Z \exp\left[-\frac{a}{2} (\omega - \omega_0)^2\right].$$

Since, for a gaussian, the full width at half maximum is given by  $2\left(\frac{\ln 2}{a}\right)^{\frac{1}{2}}$  we find  $\text{FWHM}_{\text{uv}} = \sqrt{2} \text{FWHM}_{\text{vis}}$ .

Since our laser cavity is not stabilized, the longitudinal cavity modes change from pulse to pulse. The etalon serves as a stable frequency selector and the time average of the mode hopping serves to generate a smooth frequency profile defined by the bandwidth of the etalon.

Note that if lasing occurs on more than one cavity mode, the doubling crystal generates frequencies not only at  $2\nu_{\text{vis}}$  but

also at the sum frequencies of each pair of visible frequencies.

In practice, the sum in Equation II-2 is not infinite and the uv line width is narrower than predicted. In order to get a numerical estimate of this effect, the sum in the real part of Equation II-2 is truncated and the expected uv intensity is calculated. These results are shown in Table II-1. Based on these data and the known number of visible modes,  $I(\nu_{uv})$  is best described as a nearly Gaussian line shape with a FWHM of 1.55 GHz.

## 2. Etalon Position in Laser Cavity

Figure II-6 shows a schematic of the Chromatix 1050 dye laser cavity as depicted in reference two. Of special interest here are the etalon positions indicated by G and I. Originally, the 1mm, 55% reflective etalon had been positioned at G next to the dye cell, C. This arrangement was and is entirely satisfactory for the internal state measurements. However, in the course of the FTDS experiments, a slight, but noticeable frequency drift (on the order of 50 MHz/min) was observed. This was attributed to temperature fluctuations of the heated (40°C) etalon caused by (1) difficulty in making good thermal contact from the quartz etalon through teflon "pads" to the stainless steel holder (whose temperature was very accurately controlled by a feedback mechanism) and (2) convectional cooling of the etalon to the nearby dye cell through which there was a constant rapid flow of (water cooled, approximately 10-15°C) dye.

In order to alleviate this problem, the etalon was positioned at I and allowed to reach thermal equilibrium by heating for a period of several hours before each experiment. Although this did not entirely eliminate the frequency drift, it was reduced so as to no longer effect the measurements (less than 1MHz/min). If, in the future, better thermal control is required, a copper mount which grips the etalon around its entire circumference would probably be much better suited to

Number of modes	FWHM <sub>uv</sub> (GHZ)	% difference from theoretical results
5	1.44	15%
7	1.55	10%
9	1.55	10%
∞	1.7	---

Table II-1.

Figure II-6

Schematic of the modified Chromatix 1050 dye laser cavity.

- A. Input lens
- B. Input mirror
- C. Dye cell
- D. Doubling crystal
- E. Output mirror
- F. Telescope mirror
- G. Etalon position #1
- H. Prism bank
- I. Etalon position #2
- J. Rear mirror



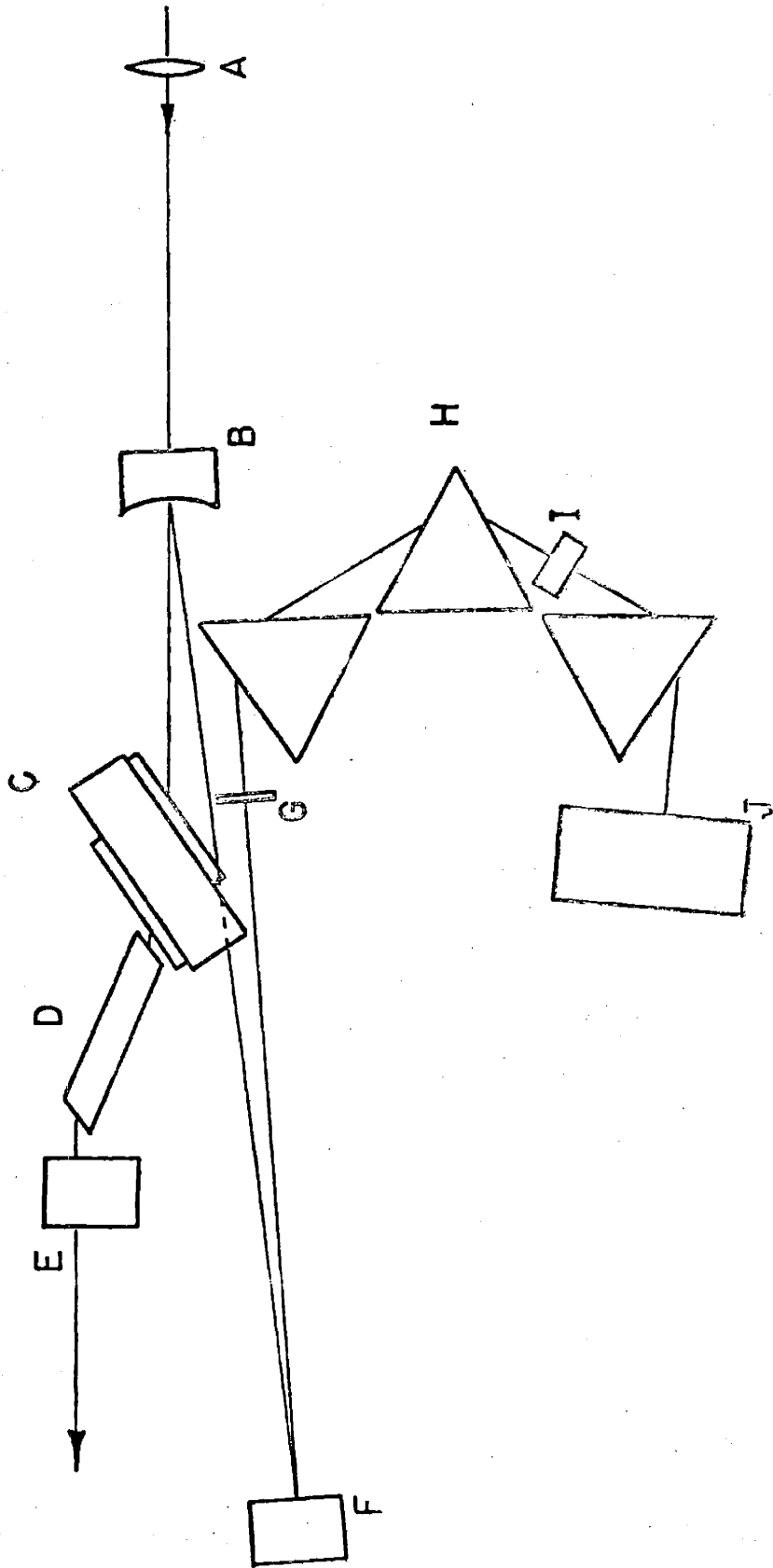


Figure II-6.

the job than the current stainless steel-teflon mount which only contacts the etalon along one-half of its circumference.

### 3. Laser Path through the Apparatus

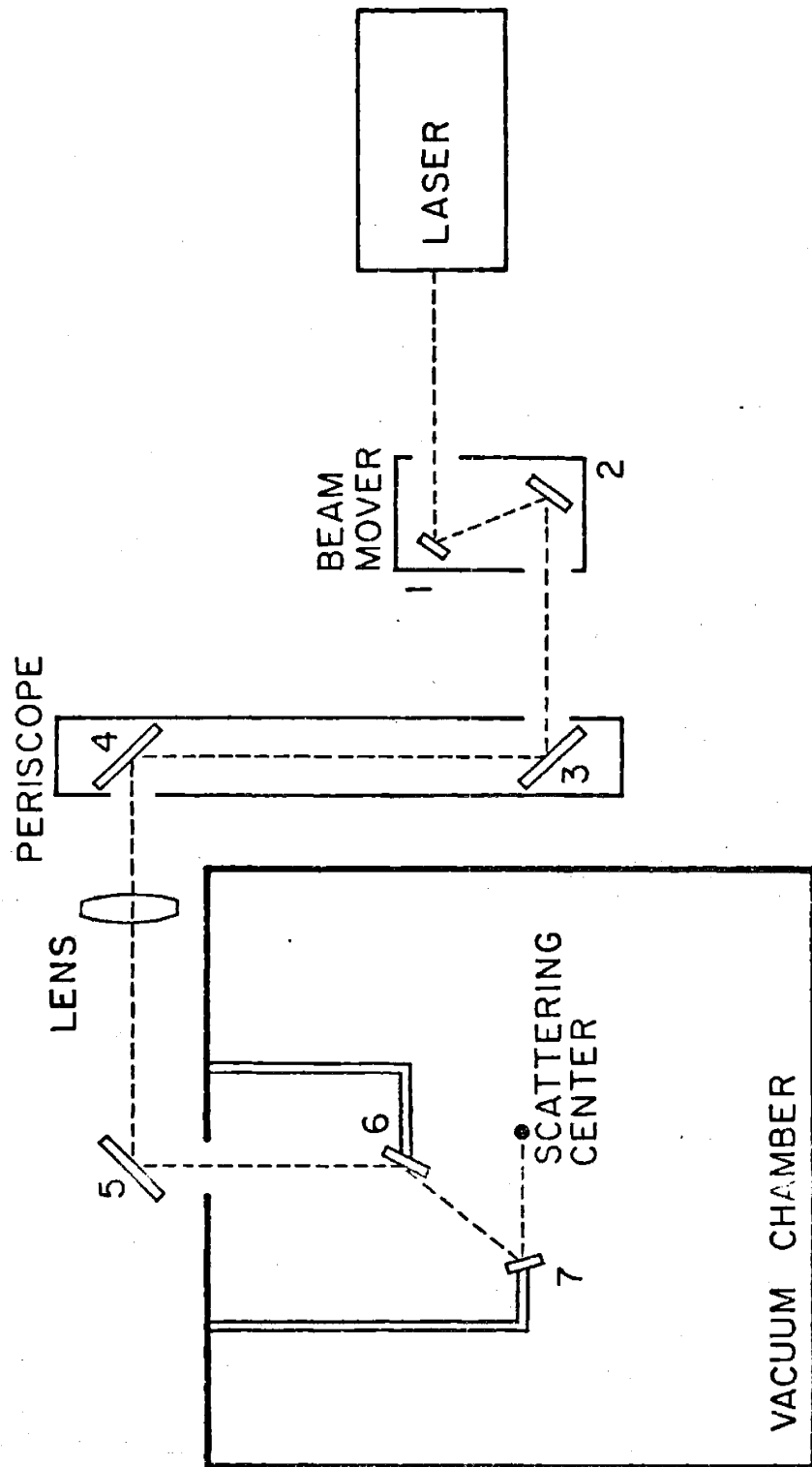
The UV laser output is directed into the scattering center by a system of seven plane mirrors. As shown in Figure II-7, the beam first passes through a beam mover (mirrors 1 and 2) and then through a periscope (mirrors 3 and 4) which directs it across the top of the apparatus. The beam passes through a lens which has its focal point at the scattering center. Then, mirror 5 reflects the beam through a quartz optical flat at the center of the rotating lid and into the vacuum chamber along an axis that is perpendicular to the plane of the rotating lid and thus to the plane of the molecular beams. Mirrors 6 and 7 are suspended in the vacuum system from the rotating lid and serve to re-orient the laser beam such that it propagates in the same plane as the molecular beams. Thus, by rotating the lid, the angle from which the laser beam is incident on the scattering center can be varied over a range of approximately  $190^\circ$  in the plane of the beams. Mirrors 3 through 7 are microscope cover glass slides with a vacuum deposited aluminum coating and a  $MgF_2$  overcoat. A beam splitter is positioned between the quartz flat and mirror 6. It splits off part of the beam to a phototube which is used as a laser power monitor.

### 4. Fluorescence Detection

The problem of scattered laser light interfering with fluorescence collection is dealt with in three ways. First, standard electronic techniques are used to time gate against the laser light. These considerations will be dealt with in a later section. Secondly, all surfaces near the scattering center are blackened either with a flat black paint or with colloidal graphite to minimize reflected light. A blackened

Figure II-7

Laser light path through the apparatus.



piece of aluminum foil is placed around the scattering center to eliminate light from the microwave discharge and scattered laser light from mirror #6. Finally, a series of lenses and baffles and a pinhole are used such that only light originating at the scattering center will reach the phototube. A UV transmitting filter (Corning 7-54) is positioned just above the phototube to eliminate detection of spurious visible radiation. A schematic of this arrangement is shown in Figure 1.

Despite these precautions, scattered laser light produces thirty to fifty counts per second (compared to a few hundred signal counts) at those angles where the beam clips one of the sources near the center. However, at most angles, scattered laser light contributes only five to ten counts per second and, at those angles where the beam does not encounter any surface near the scattering center, a background count rate of one to two counts per second is attainable. Background from other sources (i.e. room lights, microwave discharge, dark noise) is negligible. For the FTDS experiments, angles of illumination can be chosen to minimize measurements at "noisy" angles. For the internal state distribution experiments, a low noise angle is chosen.

#### IID. Signal Processing and Data Collection

The signal processing system is nearly identical to that discussed in reference two. Figure II-8 schematically depicts the system. The major differences between the two systems are: (1) this system uses one less gate and delay generator, (2) average laser power is monitored by a phototube outside of the vacuum system and (3) peak laser power is not monitored. For completeness, a paraphrased version of the description of the electronics system and data processing in reference two is included here.

The components of the system fall into four basic categories: those which process the fluorescence signal, those

which supply diagnostics during an experiment, those used in monitoring laser power and the computer with its peripherals.

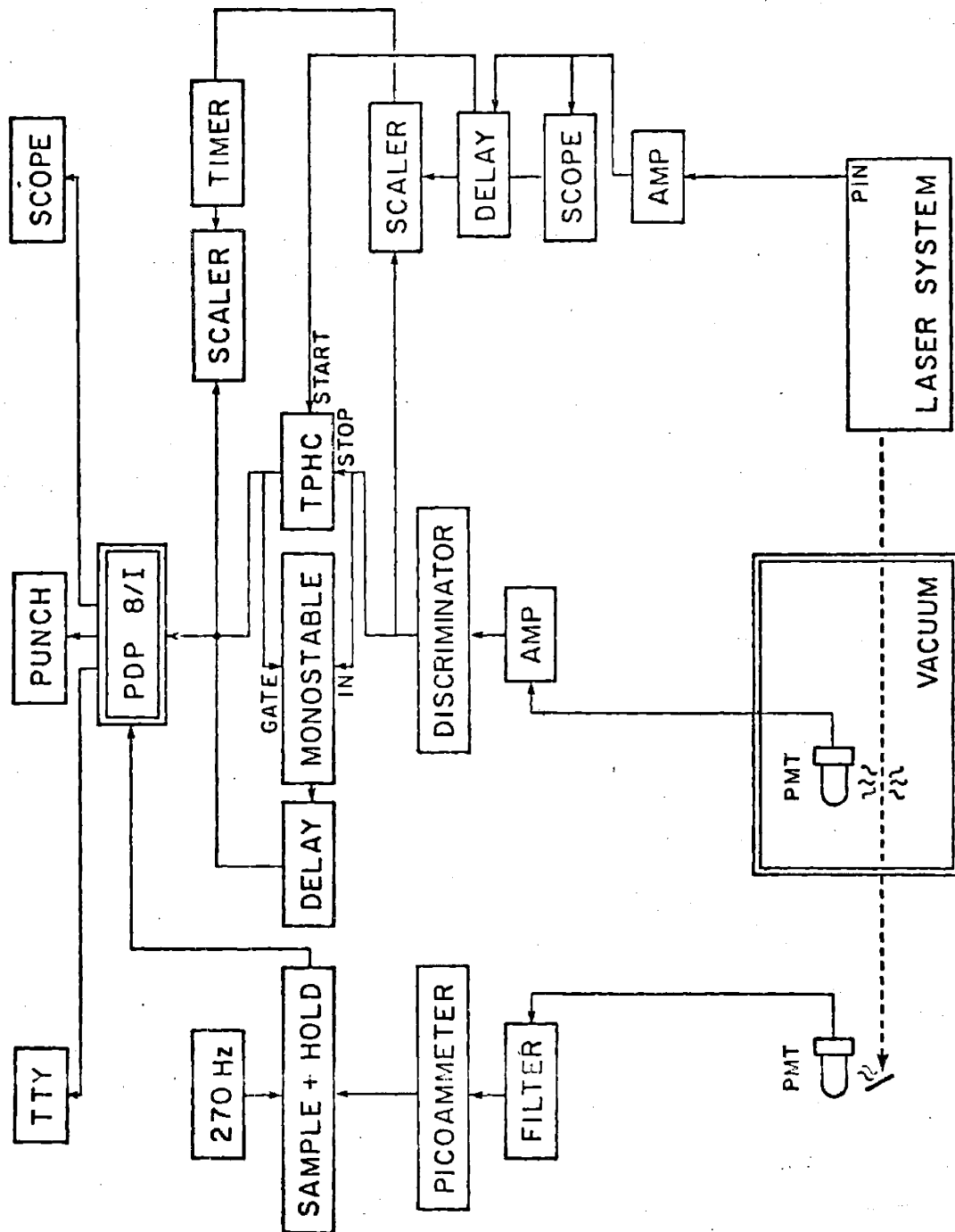
A pin photodiode which detects the visible output pulses of the Nd:YAG laser serves as the trigger for the signal processing by switching on an Ortec 417A Gate and Delay Generator 350 nanoseconds after the laser pulse. The gate remains open for 4.8 microseconds allowing the output of the phototube to be detected during this time.

The output of the phototube is amplified by four stages of an Ortec AN201/N discriminator which generates a NIM standard negative logic pulse for every input pulse. An Ortec 437A Time to Pulse Height Converter (TPHC) is used to convert this negative logic pulse to a positive TTL compatible pulse for the computer interface. (The time to amplitude capability of the TPHC is not used in this application.) As the TPHC can only process one fluorescent photon per laser pulse, a monostable circuit and another gate and delay generator are used to process second photon pulses should they occur. The output of the discriminator and the input to the computer interface are monitored by Ortec 772 counters to insure that no coincidence loss occurs in the signal processing.

Signal averaging is controlled by a PDP 8/I minicomputer which performs the dual functions of laser tuning and digital signal averaging. After the laser is tuned to line center of a single rotational transition it is scanned by tuning the etalon, rear mirror and doubling crystal over a wavelength region of approximately 0.1A in 128 equal steps. The computer uses a multichannel array of 128 bins to digitally store fluorescent intensity versus wavelength as the laser scans. A second such array is simultaneously used to store the laser power monitor readings. The laser is repetitively scanned across an absorption line to build up a good signal to noise spectrum. A single scan takes from a few minutes to one hour depending on number density, laser power and transition probability. A strong line will generate several thousand fluo-

Figure II-8

Block diagram of signal processing electronics.





rescence pulses per second at the absorption peak.

The machine language computer program which controls the experiment is reproduced in Appendix B of reference two.

### III. Apparatus Alignment

The complete alignment of the apparatus which will be described here is naturally partitioned into a three step process. First, the nozzle and collimator for the molecular beam source are aligned outside of the vacuum chamber such that a HeNe laser passes through the skimmer and through the nozzle and emerges from the alignment hole in the back of the oven. Since the laser light diffracts upon passing through the small nozzle and collimator orifices, this alignment is checked with a cathetometer before mounting the source in the apparatus.

The second step is to align the sources in the vacuum chamber. A cathetometer is secured to the rotating lid so that it can be rotated to sight along both beam sources. A plumb bob is suspended from the center of the lid. Using the cross hairs of the cathetometer, the molecular beam source is positioned to give a clear line of sight through the source coincident with the axis defined by the plumb bob. The lid (and cathetometer) is then rotated through  $90^\circ$  and the procedure is repeated for the atom source.

Step three involves the optical alignment. The plumb bob is adjusted so that its tip hangs approximately at the height of the scattering center. The detector housing is then positioned under the plumb bob and the plumb bob is removed. The laser beam is then directed along this central axis, mirrors 6 and 7 are inserted and, by iterative (painful) adjustments of the mirrors, the beam path is tweaked so as to pass directly through the molecular beam source and, when rotated through  $90^\circ$ , to strike the tip of the atomic beam source. A mercury pen light is placed in the detector housing (in the position normally occupied by the phototube) and the focus of the

detector is adjusted to coincide with the scattering center as defined by the beam sources and the laser beam. Finally, the lid is rotated through its full 190° of travel to be sure that the laser beam passes through the detector focus at all angles. The pen lamp is removed and the phototube is inserted. The alignment hole in the back of the molecular beam oven is sealed with a screw that has a photodiode epoxied to its tip. When the rotating lid is turned so as to direct the laser beam into the molecular beam source, output from the photodiode indicates proper alignment. Thus, alignment can be checked after the system is pumped down and at any time during an experiment. Fine tuning of the laser alignment is accomplished during a run by adjusting mirror 5 to maximize the observed signal.

#### IIF. Operational Details

In order to insure that the apparatus has reached a stable equilibrium before data is recorded, the diffusion and cryopumping, the microwave discharge source, the laser, the phototubes and the electronics are given a three to four hour "warming-up" (or cooling down) period. To avoid contaminating the system, the molecular reagent beam typically ran for only one-half to one hour before the measurements were started.

Mirrors 6 and 7 are found to develop an opaque film and required periodic cleaning with methanol and lens tissue. Also, despite the fact that these mirrors are coated with  $MgF_2$ , the aluminum surface slowly oxidizes and the mirrors must be replaced every few weeks.

As discussed earlier, because surface recombination effects are significantly reduced with the new microwave source design, frequent cleaning of the discharge tube is not necessary. Typically, the tube is removed, washed with concentrated HF and rinsed with distilled water every two months.

### Chapter III - Internal State Distributions

As mentioned in the introduction to this work, the dynamics of the  $\text{H(D)} + \text{NO}_2$  reaction have been extensively studied by chemiluminescence, laser induced fluorescence and conventional velocity-angular distribution techniques. These studies will be referred to throughout this chapter. Here, the remeasurement<sup>(2)</sup> of energy partitioning into the energetically available states of CH and OD is reported. This detailed information is exhaustively analyzed and provides an interesting qualitative picture for the reaction mechanism.

#### IIIA. Data Acquisition and Analysis

In order to obtain the data, the laser is scanned across a single absorption peak (in the manner described in Section IIp) until the integrated fluorescence counts total about 14000. This normally takes about ten minutes. The reduction of these raw data to relative cross sections is a multistep process involving: (1) normalization to laser power fluctuations, (2) normalization for the spectroscopic transition probabilities for the detected states and (3) conversion of the measured number densities to flux intensities.

First, one must carefully account for laser power variations during a scan and during the course of a day's experiments. This is accomplished by dividing the number in each bin of the 128 bin signal array by a number proportional to the value recorded in the corresponding bin of the power monitor array. The proportionality constant is taken to be the value of one bin of the power monitor array from the first scan of each day's experiments. This yields the required normalized LIF peak which is next corrected for any contribution from background counts (i.e., scattered laser light, phototube noise). This correction is effected by averaging over the counts in those bins far from the absorption peak which do not contain any LIF signal. This average number is then subtracted

from all bins within the peak. The resulting spectrum is summed to obtain the integrated number density. In order to monitor any unexpected fluctuations in experimental conditions during a day's run, certain peaks were repetitively scanned at 1 to 2 hour intervals. Reproducibility of a particular LIF scan throughout a day was always within 10% and usually within 5%.

Once the relative, integrated observed intensities are obtained, the remaining analysis proceeds as discussed in previous publications.<sup>(1,2,3)</sup> The observed normalized count rate is given by:

$I \propto \rho(\nu) B (1 - \exp(-t_1/\tau)) \exp(-t_2/\tau) (1 - \exp(-t_3/\tau)) n_a^0$   
 where  $\rho(\nu)$  is the laser power, B is the Einstein absorption coefficient,  $\tau$ , the excited state lifetime,  $t_1$ , the width of the laser pulse (80 ns),  $t_2$ , the delay (350 ns),  $t_3$ , the gate open time (4.8 ms), and  $n_a^0$  is the initial number density in internal state 'a' of the ground electronic state. The required lifetimes and Einstein coefficients have been previously reported.<sup>(39)</sup>

Finally, one must convert the measured number density distribution to fluxes by weighting each element of the distribution by its laboratory speed. The center of mass speed of a species in a particular internal state is given by:<sup>(1)</sup>

$$u(\text{m/sec}) = 154.67 \left[ \frac{m_{\text{NO}} P_T}{m_{\text{OD}}(m_{\text{OD}} + m_{\text{NO}})} \right] [E_{\text{Tot}} - E_{\text{OD}}(\nu, J)]^{\frac{1}{2}}$$

where  $m_{\text{CD}}$ ,  $m_{\text{NO}}$  are the masses of CD and NO respectively,  $P_T$  is the fraction of available energy in translation,  $E_{\text{Tot}}$  is taken as  $11,500 \text{ cm}^{-1}$ . The laboratory speed of the CD product is then given by:

$$v(\text{m/sec}) = [u^2 + c^2 - 2uc \cos(\beta)]^{\frac{1}{2}}$$

where c is the center of mass velocity and  $\beta$  is the angle

between the center of mass velocity vector and the OH product velocity vector. The calculation of the absolute lab speeds is very much dependent on the choice of  $P_T$  and  $\beta$  (i.e. the angular and velocity distributions), however the relative speeds have been calculated for  $P_T = 0.25, 0.5$  and  $1.00$  and for values of  $\beta$  describing both a strongly forward peaked and also an isotropic distribution; the maximum deviations found are on the order of a few percent. In accordance with results discussed in Chapter IV, the speeds calculated with  $P_T = 0.25$  were used.

Recently, (31,32,38,40) molecular beamists have become interested in measuring the orientation of species produced in a chemical reaction. Since LIF relies on the interaction between a molecule's dipole moment and the electric vector (and therefore the polarization) of the exciting light, a molecule which is produced in a preferred orientation might show a "polarization" effect not accounted for in the above analysis. In fact, even for randomly oriented samples, cross terms in the transition moment expressions can cause problems (see Appendix). However, since these latter corrections are small and our experimental arrangement is unlikely to produce oriented species in the laboratory coordinate system, any such polarization effects are expected to be negligible.

### IIIB. Fine Structure Partitioning

Because the ground electronic state of OD is of  $^2\Pi$  character, the spectroscopy of this state is complicated by spin-splitting and lambda-doubling. (49,66,67). Thus, for each state designated by rotational quantum number  $N$ , one actually has a total of four states as a result of these fine structure effects. These levels are probed by different branches of the spectrum. One can utilize these spectroscopic features to probe these states. A priori, one would expect a statistical population of these states which are nearly energetically degenerate. Preferential population of any of these states would

therefore indicate some sort of dynamical bias.

Comparison of observed LIF intensities in the  $R_1$  and  $R_2$  branches which originate in the  $\Omega = \frac{1}{2}$  and  $\Omega = 3/2$  spin states respectively were used to probe spin state partitioning; for both spin states, R and Q branches which originate, respectively, from  $\Pi^+$  and  $\Pi^-$  lambda states, were used to probe lambda state partitioning. The resulting intensities were treated as discussed in Section IIIA with one exception. No number density to flux correction is necessary as the fine structure levels are so close in energy that the ratio of these corrective terms is essentially unity for states of the same N quantum number.

The results of these measurements on CD  $v=0$  spin states are shown in Figure III-1. Also shown are the results of Mariella and Luntz<sup>(41)</sup> for CH  $v=0$ . The solid line represents the ratio of populations of the two spin states for a purely statistical distribution:

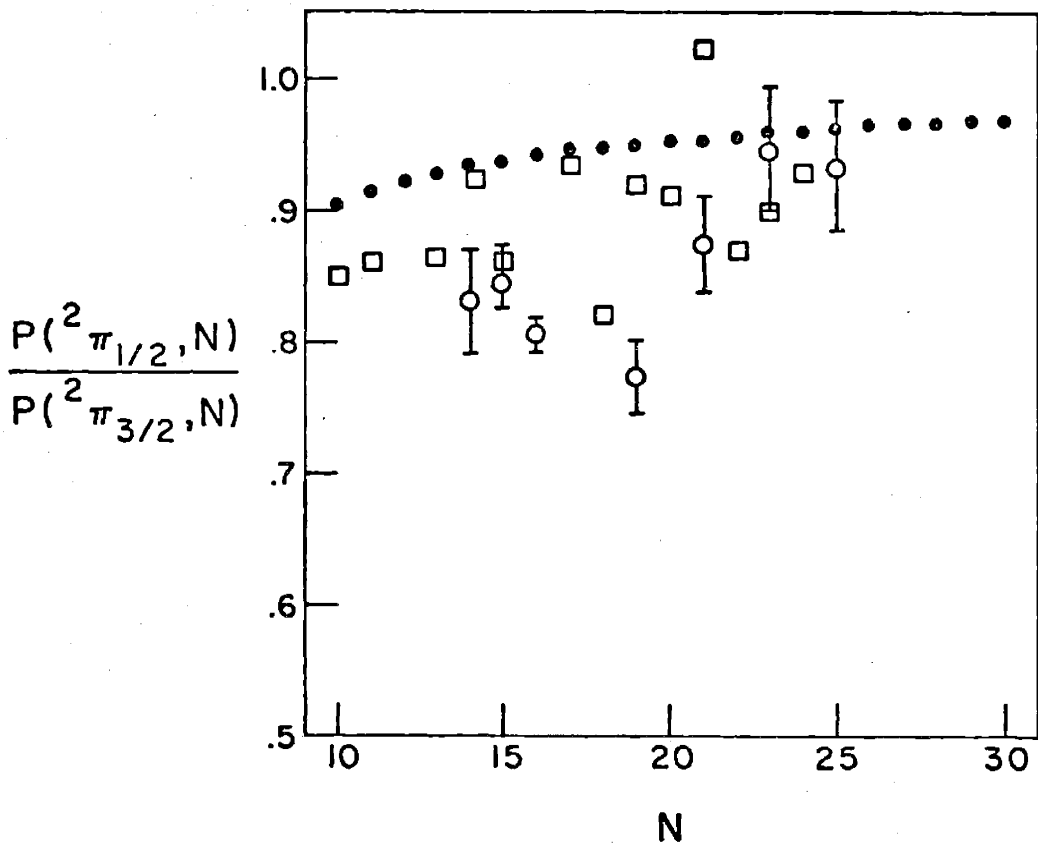
$$P(^2\Pi_{\frac{1}{2}}(N))/P(^2\Pi_{3/2}(N)) \cong N/N+1.$$

The circles with error bars are our experimental points and the squares are the data of Mariella and Luntz as read from Figure 1 in their paper.

The results in Figure III-1 lie systematically below the statistical line although the departure is not large compared to the individual confidence limits. Although partial relaxation would tend to push the data in the observed direction, we rule this out on the basis of the implausibly large cross sections that would be required under our operating conditions. Moreover, Doppler profiles of these transitions show no evidence of translational relaxation even at background pressures an order of magnitude higher than our normal operating pressure. (The Doppler profiles begin to narrow at forty times normal operating pressure.) Thus we conclude that we observe the true spin state distribution and that this distribution is essentially statistical.

Figure III-1

Measured spin state distributions. The open circles with error bars are our measurements on OD  $v=0$ . The squares are measurements on CH  $v=0$  read from a plot in reference 41 and thus are subject to minor error. The solid circles are the predicted ratios for a statistical spin state distribution.





As mentioned above, partitioning into lambda doublet levels was probed for OD  $v=0$  utilizing  $R_1$ ,  $Q_1$ ,  $R_2$  and  $Q_2$  transitions. The measured distributions are highly non-statistical and show a 1.4:1 preferential population (independent of  $N$ ) of the higher energy component of the doublet. This result compares favorably with a ratio of 1.5:1 for OH  $v=0$  as reported by Mariella and Luntz.<sup>(41)</sup> The significance of this result will be discussed in Chapter V.

Very slight preferential population of the higher lambda doublet of the four energetically lowest rotational states of OH produced in reaction 1b has been observed in molecular beam maser and molecular beam electric resonance experiments.<sup>(42)</sup> In fact, this phenomenon is thought to be the cause of observed interstellar OH microwave emission. It has been postulated that preferential population of higher lambda doublets in the  $H + H_2O \rightarrow OH + 2H$  (or  $H_2$ ) are a main source of this radiation.<sup>(43)</sup> Again, we will return to this point and its significance in Chapter V.

### IIIC. Internal State Distribution Results and Information Theoretic Analysis

#### 1. Conventional Information Theoretic Analysis

The measured relative flux distributions for the  $v=0$ , 1, and 2 vibrational states of OD produced in Reaction 1a and  $v=0$  of OH from Reaction 1b are shown in Figures III-2 and III-3. These distributions are the result of approximately 20 separate experiments, each of which measured at least 75% of the rotational lines in a particular vibrational state. Often each line was measured more than once during an experiment. The  $R_1$  branches of the  $OD(CH)A^2\Sigma \rightarrow X^2\Pi$  transition are chosen for this study as they span a relatively compact frequency range and are nearly free from overlapping transitions. The solid line through the points is the result of a three parameter fit to the entire set of data for each reaction based on a reaction scheme to be

Figure III-2

The OD internal state distribution as measured for  $v=0,1,2$ . The points are our data and the line through them is the result of a theoretical fit. The distributions shown for  $v=3$  and 4 are the result of extrapolation of this theoretical fit to these unobserved levels.

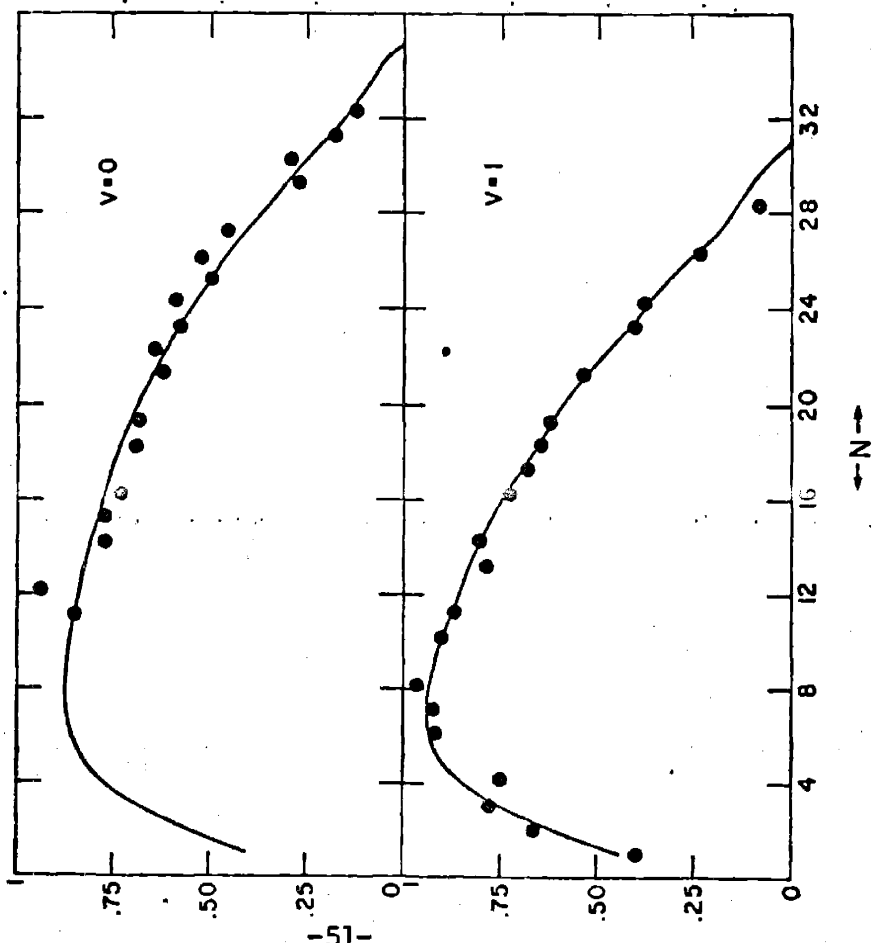
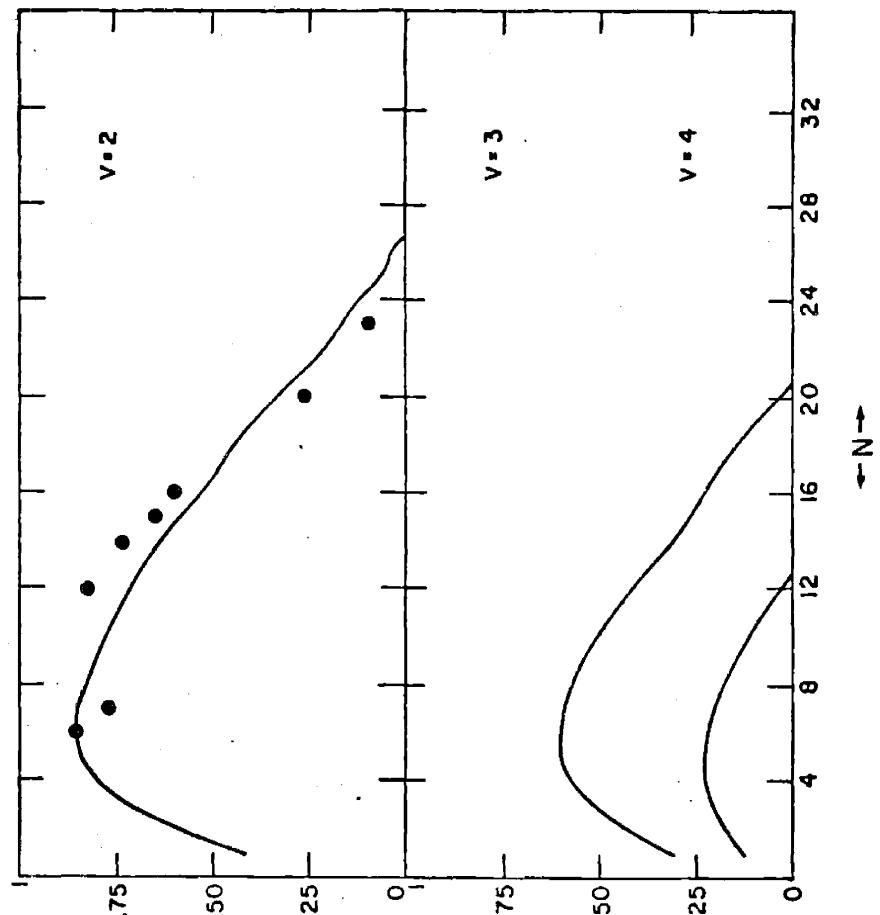
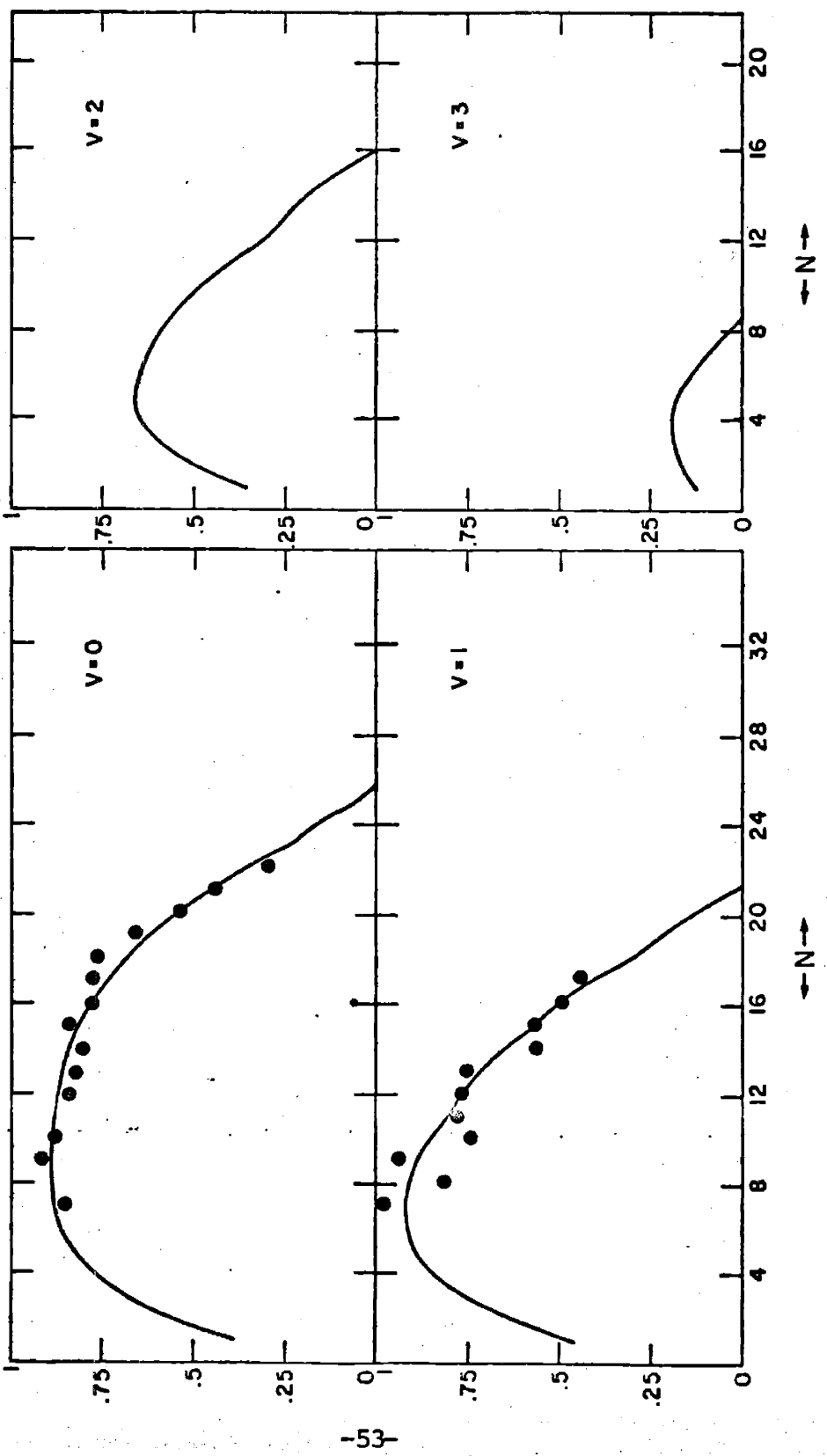


Figure III-3

The CH internal state distribution as measured in this laboratory for  $v=0$ . The  $v=1$  data were read from a surprisal plot in reference 44. The lines through the points are a theoretical fit to the data and the distributions shown for  $v=2$  and  $3$  are the result of extrapolation of this fit to unobserved levels.



discussed later. Included in Figure III-3 are data taken from the surprisal plots of reference 44 for CH ( $v=1$ ) formed in Reaction 1b. The CH  $v=1$  data are subject to some uncertainty as the probabilities (P's) are calculated after being read from the surprisal plots as  $-\ln(P/P^0)$ . The induced distributions (see later discussion in Section C-4) for unobserved vibrational states are also included in Figures III-2 and III-3.

The initial stages of data reduction and analysis followed the standard Levine and Bernstein information theoretic approach. (23,24,25) Figure III-4 shows a plot of the rotational surprisal,  $I_{\text{Rot}} = -\ln[P(N|v)/P^0(N|v)]$  versus  $f_R = E_R/E_{\text{Total}}$  and  $g_R = E_R/(E_{\text{Total}} - E_{\text{vib}})$  for the  $v=0, 1, 2$  states of OD and the  $v=0$  state of CH. P is the experimentally measured probability for the production of a particular internal state and  $P^0$  is a statistical prior calculated by an exact density of states count constrained only by energy conservation:

$$P^0(E_{\text{OD}}(v,J,N), E_{\text{NC}}(v,J,N) | E_T) = [(2J_{\text{OD}} + 1) \sum_{v_{\text{NO}}} \sum_{N_{\text{NO}}} \sum_{S_{\text{NO}}} (2N_{\text{NC}} + 1) (E_T - E_{\text{OD}} - E_{\text{NC}})^{\frac{1}{2}}] / Q$$

Equation III-1.

Here,  $(E_T - E_{\text{OD}} - E_{\text{NC}})^{\frac{1}{2}} = \rho(E_{\text{Trans}})$  is the translational density of states,  $E_T$  is the total energy available to the reaction (i.e.  $\Delta H + E_{\text{reactants}}$ ) which is taken to be  $11,500 \text{ cm}^{-1}$  ( $= 2.3 \times 10^{-12} \text{ erg/molecule}$ ), Q is the total density of available states. The summations for the vibrational, rotational and spin states of NC range over energetically accessible states and  $E_{\text{OD}}(v,J,N)$ ,  $E_{\text{NC}}(v,J,N)$  represent the energy of the given molecule in a quantum state specified by  $v,J,N$ . These levels were calculated from the formula:

$$E(v,N) = B_V[(N+1)^2 - 1 - \frac{1}{2}(4(N+1)^2 + a_V(a_V-4))] - D_V(N+\frac{1}{2})^4 + G(v) \quad \text{Equation III-2.}$$

using constants obtained from Huber and Herzberg,<sup>(45)</sup> and reported here in Table III-1. All energies are referenced to the ground vibrational states.

In some papers on information theory,<sup>(46)</sup>  $g_R$  has been proposed as the variable of choice for rotational surprisal analysis while  $f_V = E_V/E_{Tot}$  is used for the vibrational analysis. We question this choice on the grounds of the asymmetry in treatment of rotational and vibrational degrees of freedom. Otherwise, one is accepting the tacit premise that each collision determines the vibrational energy disposal earlier than the rotational energy disposal so that the rotational distribution is established only after the vibrational distribution is 'known'. Surely, in general, a product molecule obtains its internal energy in a concerted process rather than this inferred two step process. For these reasons we have examined data fits both with  $f_V$ ,  $f_R$  and  $f_V$ ,  $g_R$  as the independent variables.

The solid lines shown in Figure III-4 are based on a quadratic least squares fit to the points. The parameters producing the best fits are given in Table III-2. Unfortunately neither of the rotational parameters is invariant to vibrational state or isotopic substitution. Moreover, there is no obvious pattern for the variation of the parameters.

One can define an analagous vibrational surprisal plot

$$I_{vib} = -\ln [P(v)/P^0(v)]$$

where  $P(v) = \sum_J P(J,v)$  and  $P^0(v) = \sum_J P^0(J,v)$ . A plot of this function versus  $f_V$  for the three OD vibrational states (not reproduced here) does produce a straight line. Since only  $v=0$  of CH was measured in the current set of experiments, no such vibrational surprisal plot can be produced from these data for CH. However, from reference 44, the OH vibrational surprisal

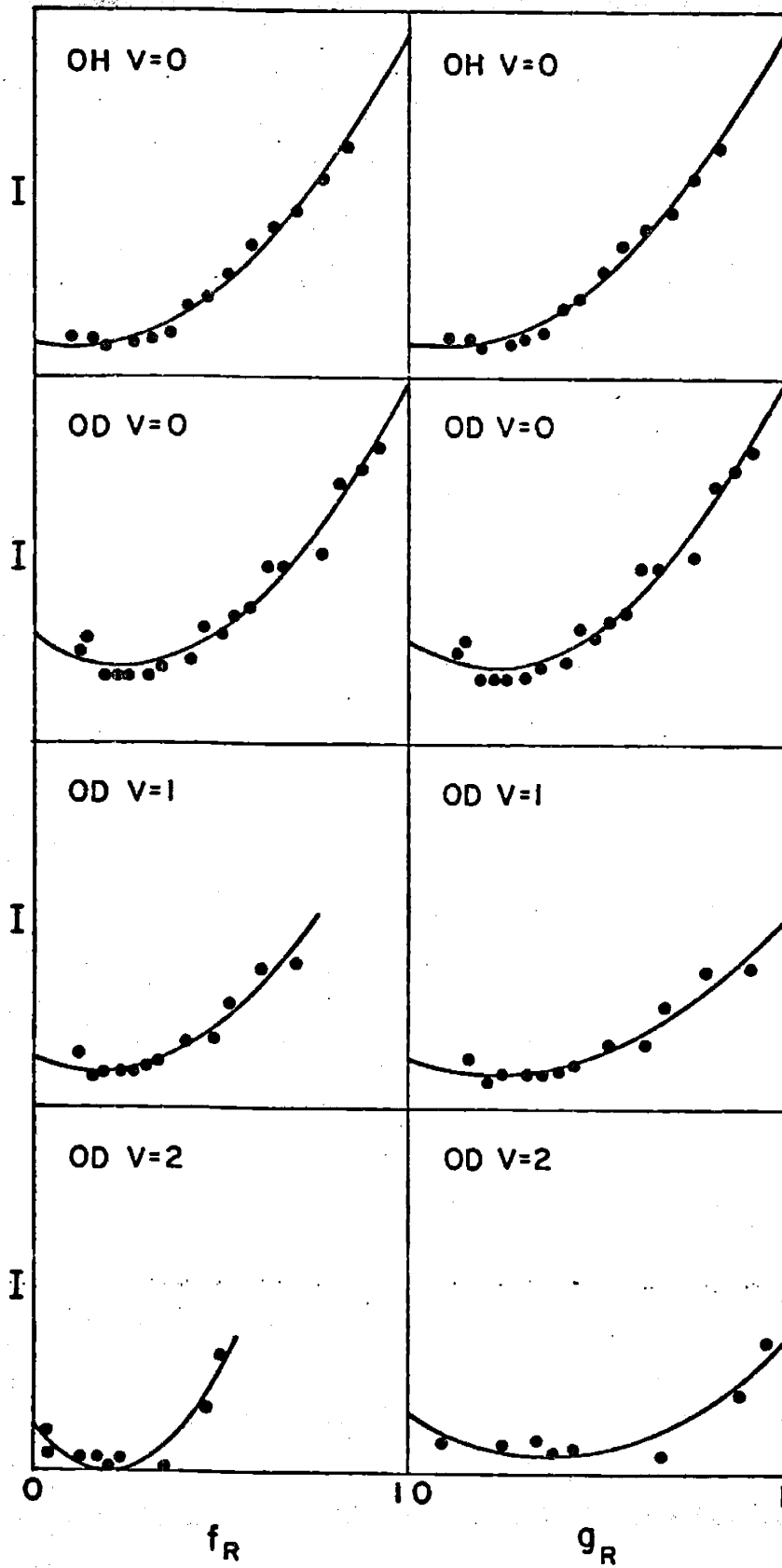
State	$G(v), A$	$B_v, B$	$D_v, D$	$a_v(a_v-4), Y$
OD v=0	0	9.8830	$5.37(10^{-4})$	254.82
OD v=1	2632.13	9.6074	$5.33(10^{-4})$	268.71
OD v=2	5176.15	9.3317	$5.28(10^{-4})$	283.78
OD v=3	7632.06	9.0575	$5.25(10^{-4})^*$	300.15*
OD v=4	9999.96	8.7825	$5.25(10^{-4})^*$	318.20*
CH v=0	0	18.5479	$19.17(10^{-4})$	86.34
CH v=1	3569.43	17.8240	$18.79(10^{-4})$	92.53
CH v=2	6973.67	17.0995	$18.46(10^{-4})$	99.48
CH v=3	10214.87	16.3753	$18.17(10^{-4})$	107.32

Table III-1. Vibrational and rotational constants for CH and OD used in the calculation of energy levels and priors. The conventional spectroscopic symbol and the symbol used in the computer program (see Appendix B) are both given. Values for the NC constants are contained within part three of the program. All constants are taken from reference forty five. Note that  $a_v = A_v/B_v$ .  $G(v), B_v, D_v$  values are in  $\text{cm}(-1)$ .



Figure III-4

Surprisal plots for CD and CH using the conventional prior,  $P^0$ . They are shown plotted against  $f_r$  and  $g_r$ . The lines through the points are the result of a quadratic least squares fit.



parameter (i.e. the slope of the surprisal plot) is found to differ. Since our current and old<sup>(3)</sup> data on OH v=0 are in excellent accord with that of reference 44, a comparison of these OH and CD vibrational parameters seems legitimate.

Since a major intent of information theoretic analysis is to simply parameterize the observed distributions, these above results are unsatisfactory. Basically, we find that the distribution in each vibrational state is characterized by two parameters:

$$P(J|v) \propto P^0(J|v) \exp(\lambda_1 f_R + \lambda_2 f_R^2)$$

or

$$P(J|v) \propto P^0(J|v) \exp(\lambda'_1 \epsilon_R + \lambda'_2 \epsilon_R^2)$$

and that there is no predictable variation of these parameters from state to state, hence no predictive power for unobserved vibrational states is gained. If we consider the four rotational state distributions measured here and the OH v=1 data of reference 44, a total of twelve independent fitting parameters are necessary to represent the data. This unappealing abundance of parameters caused us to critically review our data and the method of analysis we had chosen.

## 2. Relaxation Question Resolved

The most striking feature of the data in Figure III-4 (from an information theoretic viewpoint) is the marked curvature of the surprisal plots. One strong possibility for the cause of this effect was that we might measure a partially relaxed distribution. In fact, Mariella and Luntz, whose OH v=0 surprisal plot is virtually identical to ours, ascribe the curvature to collisional relaxation on the apparatus walls. Such a mechanism seems unlikely, as any species would probably undergo more than one wall collision before it wandered back through the detector region. One expects that several collisions with the microscopically rough walls of

State	$\lambda_1$	$\lambda_2$	$\lambda'_1$	$\lambda'_2$
CH v=0	-0.454	2.653	-0.454	2.653
OD v=0	-1.451	3.296	-1.451	3.296
CD v=1	-0.982	3.043	-0.751	1.749
OD v=2	-3.197	7.835	-1.509	2.001

Table III-2. Least squares quadratic fit parameters for conventional surprisals shown in Figure III-4.

the apparatus would produce a distribution in thermal equilibrium with the walls. However, the rotational states which show the surprisal curvature are energetically too high to be significantly populated in a room temperature thermal equilibrium and thus probably do not result from wall collisions. Relaxation also might occur by molecular collisional relaxation and by 'cascading': molecular collisions which yield rapid vibrational relaxation without rotational relaxation. (47)

A number of experiments were pursued to determine whether we were measuring true nascent distributions. Simple collisional relaxation was convincingly ruled out by measurements on the rotational and vibrational distributions at pressures an order of magnitude higher than normal operating pressure (due to an increase in the  $\text{NO}_2$  partial pressure). The distributions in both pressure regimes were identical. In fact, significant population of high CD rotational states are observed at pressures  $10^5$  times higher than normal operating pressures.

Cascading was ruled out by a set of measurements which compared the populations of given rotational states in  $v=0$  and 1 of CH as a function of pressure. Any change in the ratio  $I(v=0, N)/I(v=1, N)$  for a given N as a function of pressure would indicate cascading. Again, measurements were made for pressures up to ten times normal operating pressure. No cascading was observed. Additionally, as indicated in the previous section, analysis of the Doppler profiles of absorption peaks indicate no translational relaxation at these pressures. Coupling these experiments with the fact that the measured distributions are invariant to two experimental configurations in this laboratory (see Chapter II of this thesis and Chapter II of reference 2) and to two sets of beam conditions in another laboratory (44) provides convincing evidence that the measurements indeed probe nascent chemical products and are not the result of unwanted experimental artifacts.

### 3. Modified Information Theoretic Analysis

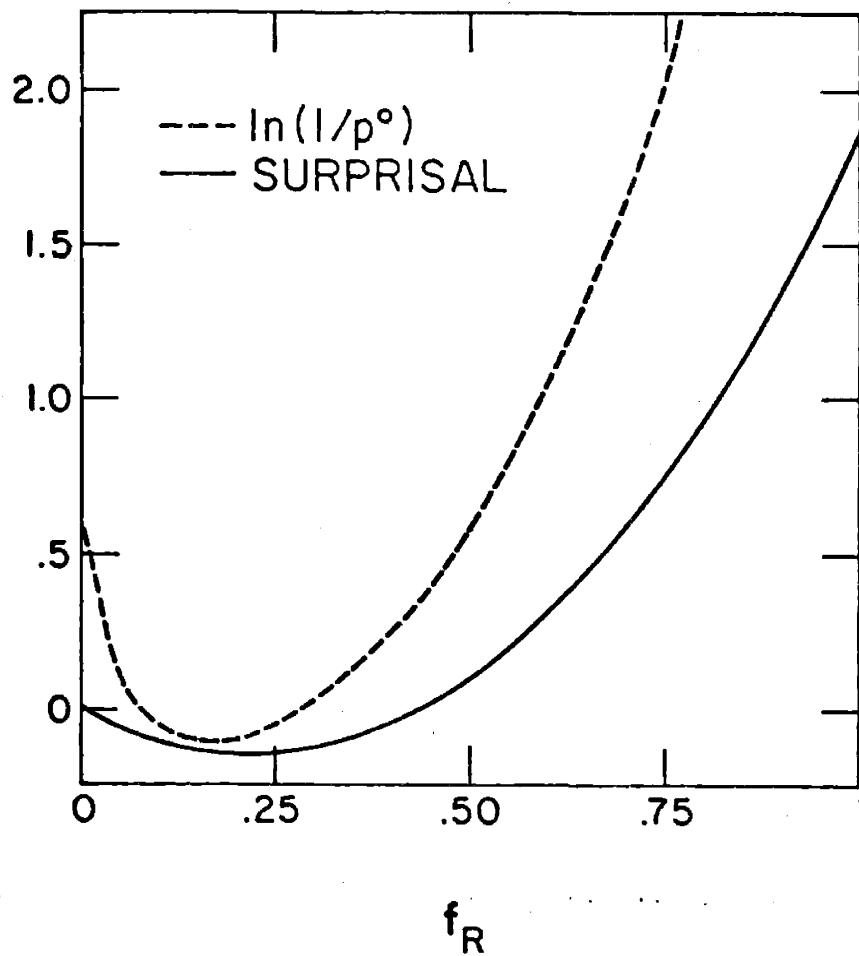
Having fortified our faith in the data but still feeling displeased with the large number of information theoretic parameters required to characterize the distributions, we were drawn to review our chosen method of data analysis. A plot of  $\ln P^{\circ}$  and the surprisal versus  $f_R$  for OD  $v=0$  is shown in Figure III-5. Note that the extrema of these two functions occur at nearly the same point. In fact,  $P^{\circ}$  affects the surprisal much more strongly than does  $P$ . As reference to Equation III-1 will show, the shape of  $P^{\circ}$  is governed by two terms: (1) the rotational degeneracy term,  $(2J+1)$ , which increases with increasing internal energy and (2) the density of unresolved states term which decreases monotonically with increasing CD internal energy.

Other pieces of experimental evidence (in particular the lambda doublet data discussed in Section IIIB and the angular distributions to be discussed in Chapter IV) suggest that the reaction might proceed through an intermediate with a predominately planar geometry. Such a mechanism would tend to produce an orientational constraint on the reaction in the form of a limitation on the allowed projection of the rotational angular momentum vector onto a molecule-fixed coordinate system (where the intermediate complex is the "molecule"). As the purpose of this chapter is merely to present the data, the reader is asked for the moment to take this point on faith; it will be more fully elucidated during the discussion of the reaction model in Chapter V.

Given a reactive trajectory strictly confined to coplanarity for Reactions 1, both diatomic products would be constrained to rotate in this plane. Thus, the projection of their rotational angular momentum vectors onto this plane must vanish. Hence, the rotational degeneracy of the accessible states would be unity rather than the full three dimensional  $(2N_{OD} + 1) (2N_{NO} + 1)$  rotational degeneracy. Therefore, for a planar reaction model, the prior as defined by Equation

Figure III-5

A plot of  $-\ln(P^0)$  and the surprisal versus  $f_r$  for  
CD  $v=0$ .





III-1 counts the accessible states inappropriately. The idea of a predominately coplanar process leads us to define a modified "theoretical" prior:

$$P^T(E_{CD}(v,J,N), E_{NO}(v,J,N) | E_{TOT}) = \left[ \frac{(2J_{CD} + 1)}{(2N_{CD} + 1)} \sum_{v_{NC}} \sum_{N_{NO}} \sum_{S_{NO}} (E_{TOT} - E_{OD} - E_{NC})^{\frac{1}{2}} \right] / Q$$

Equation III-3.

Here, the E's and Q are as defined previously but we have removed the nuclear rotational degeneracy by inclusion of a  $[(2N_{OD} + 1)(2N_{NO} + 1)]^{-1}$  factor.

At first glance, the  $(2J_{OD} + 1)/(2N_{CD} + 1)$  factor seems awkward as one might expect that the proposed confined trajectory would remove any degeneracy dependence from the prior. However, further analysis puts this term on a more solid basis. The factor appears because the suggested restriction on reactive trajectories affects only the rotational degeneracy and not the spin degeneracy. In an uncoupled basis, the angular momentum wave function is described by the quantum numbers N, M, S, and  $M_S$ . N is the nuclear rotational angular momentum quantum number, S, the spin quantum number, and M,  $M_S$  are their respective projections onto a molecule fixed axis. This initial state evolves to final product states which in the case of CD are known to be well described<sup>(39)</sup> by Hund's case (b).<sup>(49)</sup> In case (b), N and S couple strongly to form a resultant total angular momentum vector J which is described by its quantum number J and by  $M_J$ , its projection onto the same molecule fixed axis onto which M and  $M_S$  are projected.

The initial  $|NMSM_S\rangle$  states and the final  $|(NS)JM_J\rangle$  states are complete basis sets and can be related to one another by use of vector coupling or Clebsch-Gordan coefficients. Using Edmonds<sup>(29)</sup> Equation 3.5.2, we have

$$|NMSM_S\rangle = \sum_{J, M_J} \sum \sum | (NS)JM_J \rangle (NMSM_S | (NS)JM_J)$$

where the quantity  $(NMSM_S | (NS)JM_J)$  is a Clebsch-Gordan coefficient. Given the reality of the Clebsch-Gordan coefficients and making use of Edmonds Equations 3.5.14 twice and 3.5.15, we have

$$\begin{aligned} (NMSM_S | (NS)JM_J) &= (-1)^{N+S-J} (SM_S NM | (SN)JM) = \\ &(-1)^{N-J-M_S} \left(\frac{2J+1}{2N+1}\right)^{\frac{1}{2}} (JM_J S - M_S | (JS)NM) = \\ &\left(\frac{2J+1}{2N+1}\right)^{\frac{1}{2}} (S - M_S JM_J | (SJ)NM). \end{aligned}$$

Given the orthonormality of the basis sets and explicitly including a sum over  $M_S$  quantum numbers, we can write the probabilities of the angular momentum states as:

$$\begin{aligned} \sum_{M_S} \langle NMSM_S | NMSM_S \rangle &= \sum \sum \sum \langle (NS)JM_J | (NS)JM_J \rangle \left(\frac{2J+1}{2N+1}\right) \\ & \quad \times (S - M_S JM_J | (SJ)NM)^2 \end{aligned}$$

Finally, if we utilize the unitary property of the Clebsch-Gordan coefficients (in particular, using Edmonds Equation 3.5.6) and restrict  $M$  to having only a single allowed projection onto the molecule fixed coordinate system, we have

$$\sum_{M_S} \langle NMSM_S | NMSM_S \rangle = \sum_J \left(\frac{2J+1}{2N+1}\right) \langle (NS)JM_J | (NS)JM_J \rangle .$$

Thus, the  $\left(\frac{2J_{CD}+1}{2N_{OD}+1}\right)$  factor that appears in the theoretical prior of Equation III-3 occurs quite naturally when one considers the relation between initial states  $|NMSM_S\rangle$  and final product states  $| (NS)JM_J \rangle$ .

One should also note that the functional form of  $P^T$  in equation III-3 is consistent with the observed statistical spin state distribution. The statistical prior for the spin state ratio for a given nuclear rotational quantum state is given by:

$$P_{\text{spin}}({}^2\Pi_{\frac{1}{2}}(J), {}^2\Pi_{3/2}(J') | N) = \frac{P^T({}^2\Pi_{\frac{1}{2}}(J, N))}{P^T({}^2\Pi_{3/2}(J', N))}$$

Equation III-4

where we have simplified the notation of Equation III-3 on the right hand side of Equation III-4 and we define  $J = N - \frac{1}{2}$ ,  $J' = N + \frac{1}{2}$ . Then, from Equation III-3, we have:

$$P_{\text{spin}}({}^2\Pi_{\frac{1}{2}}(J), {}^2\Pi_{3/2}(J') | N) \cong \frac{2J + 1}{2J' + 1} = \frac{N}{N + 1}$$

Equation III-5.

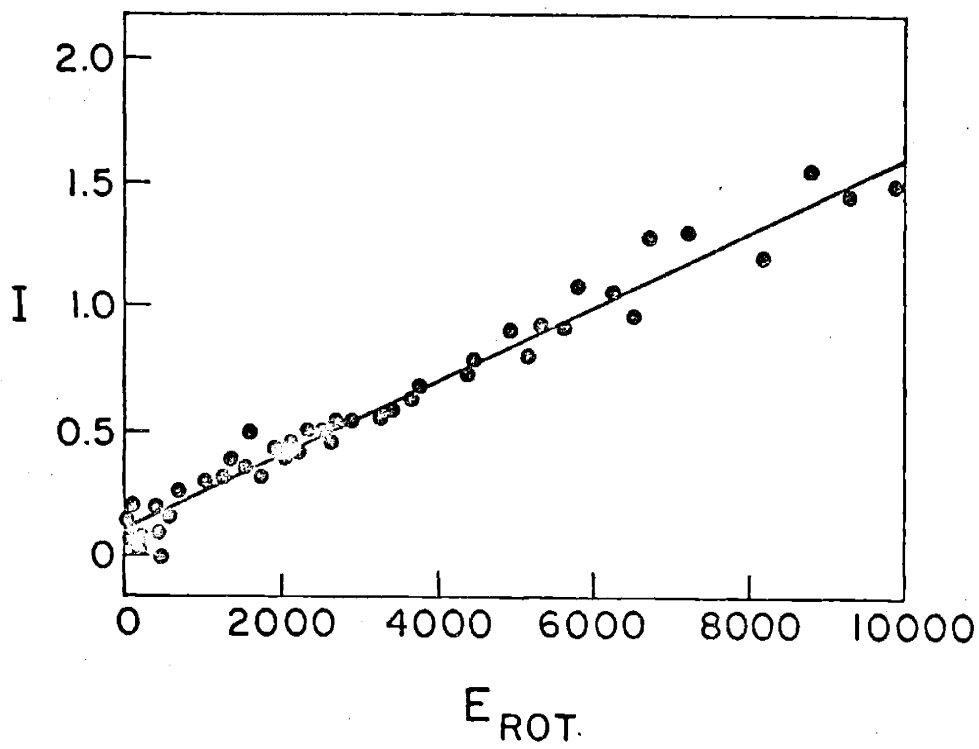
Here, the approximate equality assumes that the density of accessible unresolved translational and NO states is the same for the two spin states. As the two spin states for a given  $N$  are nearly energetically equivalent the assumption is valid; in fact, the magnitude of error decreases with increasing  $N$  and is less than 1% for all experimentally observed states.

#### 4. Results of Surprisal Analysis

The results of analysis on the OD product using this modified prior are shown in Figure III-6, where we have plotted  $I = \ln(P/P^T)$  versus  $f_R$  for  $v=0,1,2$ . The parameters of constraint were determined by minimization of the "persuasion" function<sup>(25)</sup> defined by  $H = \sum_i P_i \ln(P_i/P_i^T)$  where the summation index ranges over experimentally observed states. As discussed in Section C-1 of this chapter, we made use of the conventional set of surprisal variables  $(g_R, f_v)$  as well as the set which we consider to be more reasonable physically

Figure III-6

Surprisal plot for CD  $v=0,1,2$  data using  $P^I$ , the modified prior. The line through the points is the result of our persuasion analysis.



( $f_R, f_v$ ). In fact, based on the persuasion analysis, the latter set gave a slightly better fit to the experimental data.

We find that by using the theoretical prior of Equation III-3, the measured distributions can be characterized in terms of only three parameters! Hence, use of  $P^T$  at the very least results in a great economization of parameters. The parameterized distributions are:

$$P(v, J, N) = P^T(v, J, N) G_{\text{eff}} \exp(-\lambda_v f_v - \lambda_R f_R) \quad \text{Equation III-6}$$

or,

$$P(v, J, N) = P^T(v, J, N) G_{\text{eff}} \exp(-\lambda'_v f_v - \lambda'_R f_R). \quad \text{Equation III-7}$$

Due to the finite life time of the intermediate and the range of possible reaction approach angles (again, further discussion will be given in Chapter V), slight deviations from a strictly confined planar trajectory might be expected. In order to account for this, the term  $G_{\text{eff}} = \sum_{M=-N}^N \exp(-\gamma^2 M^2)$  allows for an effective rotational degeneracy greater than unity. Here,  $N$  is the rotational quantum number,  $M$  its projection, and  $\gamma$  is determined empirically. Inclusion of this term (which does not affect the predicted relative distributions above  $N=8$ ) describes a physically more reasonable picture as the reaction is treated as sampling a range (Gaussian-weighted) of nearly planar trajectories. The analagous  $G_{\text{eff}}$  for the NO product has a negligible effect due to the large range of the  $v$  and  $N$  summations in Equation III-3. Values of the parameters are given in Table III-3.

We also analyzed our CH  $v=0$  data and the CH  $v=1$  data of reference 44 within the constraints of this reaction model. Again, linear surprisals are observed; the fit parameters are given in Table 1. Because low  $N$  states were not observed for CH, the fit to these data is not sensitive to the selection

Variables		CD	CH
	$\lambda_R$	-1.56	-2.17
$f_V, f_R$	$\lambda_V$	-2.54	-2.60
	$\gamma$	.215	.215*
	H/n	.92(10 <sup>-4</sup> )	1.30(10 <sup>-4</sup> )
	$\lambda'_R$	-1.29	-1.92
$f_V, g_R$	$\lambda'_V$	-2.05	-1.85
	$\gamma$	.215	.215*
	H/n	1.43(10 <sup>-4</sup> )	2.24(10 <sup>-4</sup> )

\*See text for discussion.

Table III-3. Surprisal fit parameters for Reactions 1a and 1b for variable sets  $f_V, f_R$  and  $f_V, g_R$ . 'n' is the number of data points: 47 for CD, 25 for CH.

of  $\gamma$  ; accordingly, we used  $\gamma$  as determined from the OD fits. As for OD, the variable set ( $f_v$ ,  $f_R$ ) gives a slightly better fit. The poorer persuasion fit (indicated by H/n) for OH reflects uncertainty in obtaining the v=1 data from the surprisal plots of reference 44.

Using the parameters in Table III-3 and assuming that they hold for unobserved states, the induced distributions which are represented by solid lines in Figures III-2 and III-3 are calculated from Equation III-6. From these induced distributions we find the following average amounts of energy in OD and OH degrees of freedom:

$$\langle f_v \rangle_{OD} = .27 \quad \langle f_R \rangle_{OD} = .17 \quad \langle f_v \rangle_{OH} = .24 \quad \langle f_R \rangle_{OH} = .20$$

These values are accurate to within 10%. As one might expect, these numbers are essentially independent of our choice of surprisal variables as both sets of variables fit the data very well. The fit parameters were used to determine the relative probability for the production of vibrational states:

	v=0	v=1	v=2	v=3	v=4
OD	1.46	1.32	1.00	0.54	0.14
OH	1.25	1.00	0.53	0.08	----

These results are in reasonably good agreement with results from previous studies on the H + NO<sub>2</sub> system which are summarized on the following page. Care should be taken in comparing the  $\langle f_v \rangle$ ,  $\langle f_R \rangle$  results in that these results are sensitive to assumptions made in extrapolating to unobserved states. In particular, the results of Silver et al are affected by inclusion of a cascading effect in their data analysis. This effect was originally suggested by Polanyi and Sloan but now, with the benefit of some hindsight it appears that inclusion of the effect was inappropriate. Comparison of the relative vibrational populations which directly reflect measured distributions and are not sensitive to assumptions about unobserved states show excellent quantitative agreement. Although they are not reproduced here, a comparison of the raw rotational



distributions from these studies also shows good agreement.

=====

Investigators (method)	$\langle f_V \rangle$	$\langle f_R \rangle$	Rel. vib. pop. v=0:v=1:v=2:v=3	Comment
Mariella et al reference 44 (LIF)	.21	.26	1.4:1.0:-:-	a
Silver et al reference 3 (LIF)	.40	.20	1.3:1.0:-:-	a
Spencer & Glass reference 48 (EPR)	.23	---	1.4:1.0:.4:-	
Polanyi & Sloan reference 47 (Chemilumin- escence)	.3-.5	.2-.3	-:1.0:.4:.03 -:1.0:1.0:.1	b c

Comments

- a) Surprisal analysis which produced  $\langle f_V \rangle$ ,  $\langle f_R \rangle$  did not account for a planar intermediate.
- b) No correction for cascading.
- c) Corrected for cascading.

=====

## Chapter IV - Fourier Transform Doppler Spectroscopy

### IVA. Introduction

The importance of molecular beam velocity and angular distribution information in ascertaining details of the intermolecular forces affecting the outcome of elastic, inelastic, and reactive collisions has long been recognized. <sup>(10,11,12)</sup> The variety and sophistication of measurement techniques has grown accordingly. The most significant improvements have involved (1) extension of detection techniques which make possible studies on a wider range of species (i.e., mass spectrometric detectors vs. "hot wire" detectors) and (2) refinements in angular and velocity resolution which provide a stronger handle on the details of reactive surfaces. "Super machines" <sup>(12)</sup> which represent the ultimate in these technologies have been constructed and produce high quality results. <sup>(13)</sup> Unfortunately, even "super machines" do not generally provide the necessary resolution for probing scattering processes as a function of the internal state of product molecules. Only a few (difficult) experiments have succeeded in obtaining this more detailed information. Electric and magnetic deflection techniques have proven useful for some reactive systems. <sup>(12)</sup> Gentry has measured angle resolved rotational energy transfer processes involving HD + He and HD + HD using pulsed beam sources and time of flight analysis. <sup>(14)</sup>

Fourier Transform Doppler Spectroscopy (FTDS) <sup>(15,16)</sup> has been proposed as a total for studying velocity and angular distributions as a function of molecular states. It requires only that the species under study have allowed, resolvable transitions originating in the internal states of interest. Due to practical experimental considerations such as the low number density of species being detected and the narrow linewidth necessary for good velocity resolution, laser induced fluorescence (LIF) is a natural partner to FTDS. After a description of the experimental technique, this

chapter will detail the experiments which have been done in this laboratory using the LIF-FTDS method. It should be noted in passing that experiments which utilize the general concept of FTDS have been carried out in another laboratory.<sup>(17)</sup>

## IVB. The Technique

### 1. The Doppler Effect

The Doppler effect describes the general interaction of a wave (sound, electromagnetic) and an observer (human ear, molecule...) in terms of the motion of the observer with respect to the source of the wave. The frequency at which the observer "sees" the wave depends upon the relative velocity of the source and the observer. For the case of molecules and radiation we have to first order,

$$\Delta v_D = v' - v_0 = v_0 w/c = w/\lambda_0 . \quad (\text{IV-1})$$

Here,  $v_0 (= c/\lambda_0)$  is the rest frequency (i.e., absorption frequency for a stationary molecule) of a molecular absorption feature,  $c$  is the velocity of light and  $w$  is the component of the molecular velocity parallel to the direction of incidence of the radiation. Thus, a molecule in motion will absorb radiation at a frequency which differs from its rest frequency. If the molecule is moving towards (away from) the light source, it will see a higher (lower) effective frequency and the frequency must be decreased (increased) for resonant absorption to occur.

When a laser is used as the excitation source, one projects the molecular velocities onto an axis defined by the propagation direction of the laser and observes this projection through the resulting absorption frequency shift. In principle, one can directly measure the speed and direction of a collection of identical moving molecules by studying shifts in an absorption feature as a function of the angle of illumination. For two collections of the same molecules

moving with different velocities the task is more difficult but still tractable; one must simply make enough measurements to ensure an unambiguous deconvolution of the two absorption frequencies seen at each angle. For an infinite number of collections, each with a different velocity, this simple-minded deconvolution process is no longer adequate. In this case, the full velocity distribution is projected on to the propagation direction of the laser; one sees a continuous rather than a discrete Doppler profile and must invoke a more powerful means of reconstructing the three-dimensional velocity distribution,  $N(\underline{v})$ .

## 2. FTDS

As mentioned, FTDS was proposed as a method for obtaining  $N(\underline{v})$  from Doppler profile measurements. Because the method utilizes a molecule's absorption features, it is inherently sensitive to the internal state. The theorem is derived and the essence of the technique is discussed in reference 15. The algorithm can be outlined as follows. First, one measures the Doppler profiles  $D(w;\theta,\phi)$  for a number of angles  $(\theta,\phi)$  of illumination of the scattering center. Each of these profiles is then Fourier transformed to generate the set of functions  $g(k;\theta,\phi)$ . These functions describe a map (in Fourier space) of the information contained within the Doppler profiles. One must interpolate between each of the lines to obtain the full Fourier space map,  $G(\underline{k})$ . Finally, one does a three-dimensional inverse Fourier transform on  $G(\underline{k})$  to obtain the desired  $N(\underline{v})$ .

In the experiments described here, we did not implement this technique by direct application of the inversion theorem. Molecular beam experiments have an inherent cylindrical symmetry about the relative velocity vector<sup>(9)</sup> and so the Doppler profiles depend only on two variables  $D(w;\theta)$ ; only measurements in the plane of the molecular beams are necessary. In addition, we did not feel that the quality of our data warranted treatment by numerical Fourier analysis.

Although the data were reasonably noise free the laser bandwidth was actually only one fifth as narrow as the observed Doppler profiles. Such a wide resolution element washes out any details one might hope to observe by use of the numerical analysis. Instead, the Doppler profiles were fit to functional forms and the analysis was done analytically. Further details will be given in the following sections.

Figure IV-1 provides a pictorial representation of the measurement process. Shown is a Newton (or velocity vector) diagram<sup>(9)</sup> which depicts nominal velocities for the reagent beams. Let us suppose that the average velocity for the reactively scattered products is represented by the vector  $\underline{v}_0$  and let us suppose that the probability for the scattering at any other velocity falls off as shown by the contours. What would the observed Doppler profiles look like? If we bring the laser onto the scattering center from position b, we would measure a frequency shift due to the projection of  $\underline{v}_0$  onto this direction (i.e., the full length of  $\underline{v}_0$ ) and, the distribution about that point corresponding to the contours. Directing the laser onto the scattering center from any other angle, for instance a or c, we measure the projection of  $\underline{v}_0$  onto that direction and, again, the distribution about that point corresponding to the contours. Measurement of  $D(w;\theta)$  and  $D(w;\theta \pm 180^\circ)$  for any value of  $\theta$  serves to locate  $\underline{v}_0$  as  $D(w;\theta)$  and  $D(w;\theta \pm 180^\circ)$  must be mirror images about  $\underline{v}_0$ . After measuring  $D(w;\theta)$  in this fashion for a number of values of  $\theta$ , one executes the previously mentioned algorithm to regenerate the velocity contour diagram.

### 3. Number Densities to Fluxes; Coordinate System Transformation

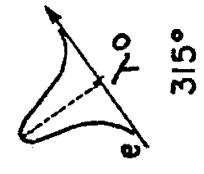
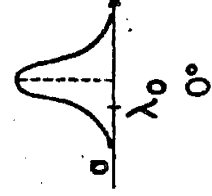
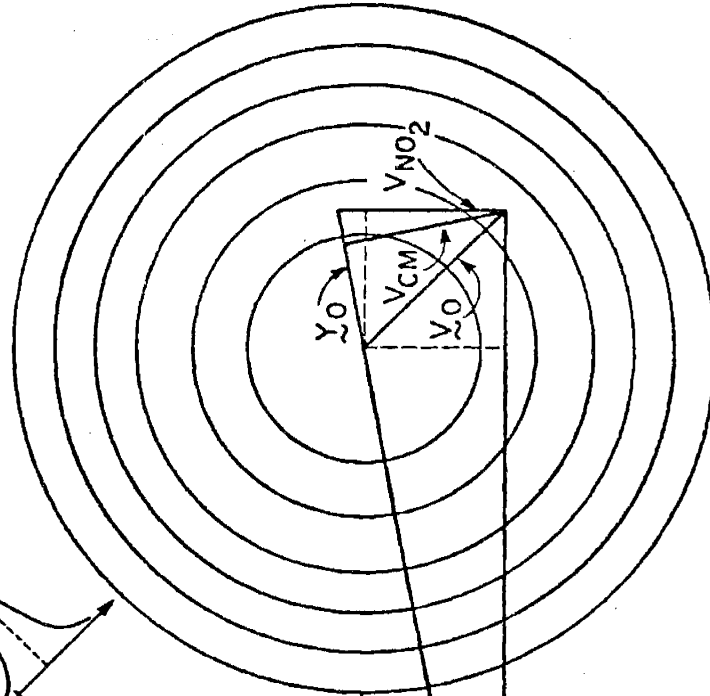
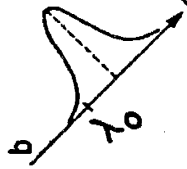
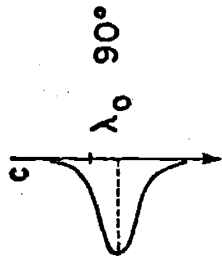
The contours shown in Figure IV-1 are quite similar to the contours actually determined by the experiment. However, they do not represent the final data form. Because we use a short ( $\sim 80$  nanosecond) laser pulse and because the lifetime

Figure IV-1

Velocity vector diagram and number density contour plots for illustration of FTDS. Shown are:

- $\vec{v}_H$       initial H atom velocity
- $\vec{v}_{NO_2}$     initial NO<sub>2</sub> velocity
- $\vec{v}_{cm}$       center of mass velocity
- $\vec{v}_{rel}$      initial relative velocity vector
- $\vec{v}_O$         average velocity shift from zero  
laboratory velocity for OH products
- $\vec{y}_O$         average velocity shift from zero  
center of mass velocity for OH products

VELOCITY VECTOR DIAGRAM  
 DOPPLER EFFECT:  $\Delta v = \lambda_0 \Delta \nu_D$   
 FOR PARALLEL VELOCITY COMPONENTS



of the excited state is short ( $\sim 1$  microsecond) we are essentially taking an instantaneous "snapshot" of the scattering center each time we fire the laser. As such, our measurement technique is sensitive to the number density of molecules in the illumination region at a given instant of time. In a molecular beam experiment one has a continuous flux of molecules into the scattering center so the quantity of interest is the flux of products out of the scattering center. The number density and flux density are simply related  $I(\underline{v}) = vN(\underline{v})$  so that we can calculate either the center of mass or the laboratory flux distributions by multiplying the measured number density distribution by the appropriate velocity.

Discussion of this number density to flux transformation draws attention to an important advantage of FTDS that has not been discussed in previous publications. In conventional velocity-angle distribution measurements one measures either the number density in a volume or the flux through an area in some region outside of the scattering center. This measurement is, of course, done in the laboratory coordinate system and so one must transform the measured distributions from this coordinate system to a center of mass coordinate system. Such transformations have been the subject of much discussion<sup>(9,18)</sup> and can cause added uncertainty in the final center of mass scattering cross sections. The problem arises in that the solid angle subtended at a given region in velocity space is dependent upon the coordinate system. Additional consideration must be included if one resolves internal states. However, FTDS does not suffer from these transformation complications. FTDS measurements are made at the scattering center and thus the measured number densities are not dependent on any solid angle (the expanding volume of product molecules has not yet expanded). As such, the number density distribution is independent of coordinate system. In the laboratory frame of reference, we measure the  $N(\underline{v})$  which describes the average velocity shift from  $v_{lab} = 0$



(designated  $\underline{y}_0$  in Figure IV-4) and the distribution about the average. If we could do the measurement in a center of mass frame, we would measure  $N(\underline{y})$  which would describe the average velocity shift from  $u_{cm} = 0$  (defined now as  $\underline{y}_0$ ) and the distribution about the average. However, these two coordinate systems are directly related by the center of mass velocity vector,  $\underline{V}_{cm}$ . In fact,  $\underline{y}_0 = \underline{v}_0 + \underline{V}_{cm}$  and,  $N(\underline{v}) = N(\underline{y})$  given  $\underline{v}^2 = \underline{y}^2 + \underline{V}_{cm}^2$ . Thus, the need for a Jacobian to transform from the laboratory to the center of mass coordinate system is eliminated and the desired center of mass flux distribution  $I(\underline{y}) = yN(\underline{y})$  is obtained directly.

#### IVC. Data Analysis

##### 1. Analyzing the Doppler Profiles

Data acquisition was carried out as described in Chapters II and III. The Doppler profiles were scanned from 11 angles of incidence onto the scattering center for four OH internal states (those probed by the transitions:  $R_2(14)(0,0)$ ;  $R_1(17)(0,0)$ ;  $R_1(19)(0,0)$ ;  $R_1(11),(1,1)$ ) and for three OD internal states (those probed by  $R_2(19)(0,0)$ ;  $R_1(23)(0,0)$ ;  $R_1(16)(1,1)$ ). The observed profiles were normalized for laser power fluctuations and the small contributions to the signal from background light were subtracted for each scan. At the two angles where the laser radiation struck the atomic source tip after crossing the scattering center, scattered laser light produced a significant background count. However, background light was very low at all other angles.

After normalization, the profiles are smoothed to eliminate minor systematic structure on the profiles. This structure is an artifact of the etalon tuning scheme and arose because the etalon driving signal from the computer passes through a 10 bit D/A converter. The resultant signal does not resolve steps as small as one bin in the multichannel array, but rather resolved three bin steps. Thus, the etalon is repositioned in every third bin of the array and the

signal reflects the decreased laser intensity in the adjacent bins. This effect is not accounted for in the normalization procedure which does not resolve the frequency of the light. To account for this, the profiles are "three bin averaged" by setting the intensity in each bin equal to one third of the sum of the counts in three adjacent bins, i.e.,  
 $c'(n) = 1/3(c(n-1) + c(n) + c(n+1)).$

The next step in the data analysis was to characterize the Doppler profiles at each angle in terms of its first four moments:  $s_1 = \sum_n n c'(n)$  and  $s_m = [\sum_n c'(n) (n-s_1)^m]^{1/m}$  for  $m = 2, 3$  and  $4$ . Here the  $c'(n)$  are taken to be normalized to unity. The first moment describes the average bin number, the second and fourth moments provide information about the width of the profiles and the third moment describes the asymmetry of the profile.

The first moments were used to determine  $v_0$  and  $\underline{v}_0$  for each transition. Measurements at  $135^\circ$  and  $315^\circ$  as indicated in Figure IV-1 serve to locate the bin which corresponds to  $v_0$  (defined as  $s_0$  for future purposes) as the first moments of these  $180^\circ$  opposite measurements must split by equal amounts but in opposite directions from  $v_0$ . Having located  $v_0$ , the remaining first moments can be reexpressed in terms of shifts from this center bin. The next step is to determine  $\underline{v}_0$ . The first moment probes the projection of the average velocity vector on to the direction  $\underline{w}$  defined by the laser, i.e.,

$$s_1 = \int \underline{w} \cdot \underline{v} f(\underline{v}) d\underline{v} = \underline{w} \cdot \int \underline{v} f(\underline{v}) d\underline{v} = \underline{w} \cdot \underline{v}_0$$

Since  $\underline{w}(\theta, \phi) \cdot \underline{v}_0$  defines a circle, this analysis tells us that the set of first moments for each transition defines a circle. The direction and magnitude of the diameter of this circle is  $\underline{v}_0$ . For each set of data on a particular transition we found  $\underline{v}_0$  by least squares fitting the measured  $(s_1 - s_0)$  shifts to a circle. It was observed that this average

velocity vector was approximately the same for all the observed internal states of a given product. We accordingly averaged over the results for each internal state and determined the vectors as shown in Figure IV-2. As mentioned previously, the distributions are kinematically constrained to be cylindrically symmetric about the relative velocity vector. Both  $\underline{v}_O(OD)$  and  $\underline{v}_O(OH)$  fit this requirement within their error bars, so for further calculations the length of the vectors were taken so as to place their tips on the relative velocity vector. The numbers so determined were approximately 400 m/s and 58° for OH and approximately 400 m/s and 46° for OD. The number density distributions about these points could then be determined by the higher moments.

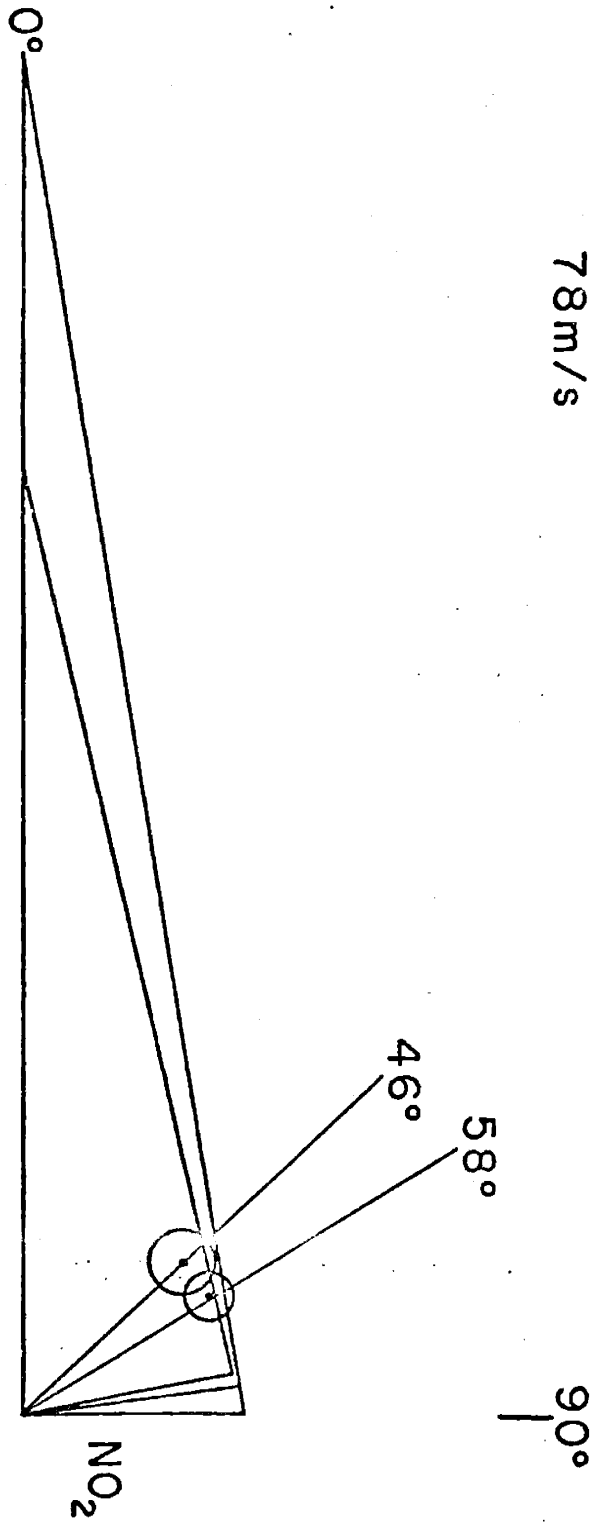
The Newton diagram shown in Figure IV-2 is based on assumed effusive beam conditions. The interpretation of the results of these and all angular distribution experiments depends on the validity of this nominal velocity diagram. If the most probable collision angle differs from 90°, the position of the center of mass velocity vector will shift and a slightly forward peaked distribution might become a symmetric distribution. The best way to eliminate this potential source of error is to use well collimated and well characterized beams. However, the FTDS technique does aid in this regard in that the laser and the focus of the detector optics define a small volume at the 90° intersection point of the two molecular beams. Thus, there is added inherent spatial resolution which defines the most probable intersection angle for detected reactive encounters. This resolution is imperfect in that molecules produced in some other region, with a different intersection angle, might be scattered into the detector region. However, we feel that under our beam conditions and given the above argument, the data and the nominal diagram of Figure IV-2 are accurate.

As discussed in Chapter II, there was an occasional problem with laser frequency drift which was minimized by a

Figure IV-2

The average velocity shifts for the OH ( $\theta=58^\circ$ ) and OD ( $\theta=46^\circ$ ) products. Newton diagrams for both reactions are shown - the diagram with the shorter relative velocity vector represents the deuterium atom reaction.

1 bin  
H  
78m/s



careful choice of the etalon position. In order to ensure that this drift did not effect our conclusions all "good" experiments met the following requirements. (1) For any given angle of illumination  $s_1$  reproduced within 0.5 bins throughout the course of the experiment. One angle was always chosen as the "benchmark" and would be repeated after every few measurements at other angles. Usually the reproducibility was better than 0.5 bins. (2) The higher moments of the "benchmark" had to be internally consistent (within 5%) for a particular day's results. This turned out to be a trivial requirement to meet--the laser drift was negligible on the time scale of a single angle measurement.

The second and fourth moments ( $s_2$  and  $s_4$ ) were found to be very mildly dependent upon the angle of illumination. As shown in Table IV-1, they peak at angles parallel to the relative velocity vector and are smallest for angles perpendicular to the relative velocity vector. However, this smooth variation (essentially cos-dependence) was only on the order of our error bars so, in the end, we chose to treat the distribution about  $\underline{v}_0$  as angle independent. Coupling this with the kinematic constraint of azimuthal symmetry about the relative velocity vector leads one to the conclusion that the scattering process is spherically symmetric about the tip of  $\underline{v}_0$ .

A reproducible determination of the third moment proved to be impossible. This calculation was extremely sensitive to noise and the resultant,  $s_3$ , varied over a wide range of positive and negative values. In fact, after averaging over experiments it appeared that  $\langle s_3 \rangle(\theta) \approx \langle \langle s_3 \rangle(\theta) \rangle \approx 0$ , where the brackets indicate averages over the included quantity. Thus, the third moment confirms spherically symmetric scattering about the tip of  $\underline{v}_0$ . This point is discussed further in section IV-D2.

Table IV-1

Moments as a function of angle for two internal states. The angles are defined in Figures IV-1 and II-2. Moments are given in units of bins in our multichannel array. One bin equals 78 m/s and equals 250 MHz.

OH R<sub>2</sub>14 (0,0)OD R<sub>1</sub>23 (0,0)

Angle	<S <sub>2</sub> >	<S <sub>3</sub> >	<S <sub>4</sub> >	<S <sub>2</sub> >	<S <sub>3</sub> >	<S <sub>4</sub> >
135°	11.50 (.24)	3.42 (3.2)	15.24 (.36)	10.35 (.36)	0.78 (4.4)	13.92 (.63)
115°	11.82 (.42)	5.73 (0.7)	15.51 (.66)	10.86 (.42)	-3.90 (4.5)	14.40 (.36)
95°	12.00 (.24)	5.40 (1.1)	15.81 (.42)	10.83 (.12)	-1.89 (3.9)	14.52 (.48)
75°	11.58 (.10)	5.25 (0.5)	15.60 (.31)	10.41 (.75)	-1.29 (5.7)	14.13 (.57)
55°	11.25 (.39)	-0.84 (3.9)	15.12 (.51)	10.20 (.24)	-2.07 (5.7)	14.37 (.93)
35°	11.67 (.39)	-0.81 (5.5)	15.84 (.84)	10.47 (.48)	1.29 (6.6)	14.58 (.27)
15°	12.03 (.50)	-2.19 (4.8)	16.11 (.63)	10.95 (.63)	-0.33 (4.2)	14.52 (.30)
5°	12.18 (.50)	0.06 (7.4)	16.59 (1.11)	---	---	---
345°	12.59 (.75)	-1.41 (4.7)	16.71 (1.23)	10.92 (.27)	-0.48 (4.8)	14.76 (.66)
335°	12.00 (.36)	2.07 (3.8)	15.81 (.45)	10.80 (.18)	-2.85 (2.0)	14.25 (.36)
315°	11.88 (.36)	-4.20 (2.4)	15.63 (.45)	10.44 (.30)	-2.01 (3.6)	13.98 (.24)
average over angles	11.86 (.36)	2.80 (3.5)	15.82 (.63)	10.62 (.27)	-1.30 (4.5)	14.37 (.30)

Table IV-1



## 2. Gaussian Fits to the Doppler Profiles

After determining the moments of the profiles, we set out to find a convenient functional form which fit the measured profiles and with which we could carry out the necessary Fourier transforms. The obvious "eyeball" similarity of the Doppler profiles to gaussian line shapes was supported by our analysis of the moments. For a gaussian (which is inherently symmetric about its center)  $s_3 = 0$  and, the ratio  $s_4/s_2 = \frac{\int_0^{\infty} x^4 e^{-a^2 x^2} dx}{\int_0^{\infty} x^2 e^{-a^2 x^2} dx}^{1/4} / \frac{\int_0^{\infty} x^2 e^{-a^2 x^2} dx}{\int_0^{\infty} e^{-a^2 x^2} dx}^{1/2} = 1.316$  is found to be in good agreement with our data. Figure IV-3 shows the quality of a gaussian fit to the data.

These fits proved to be a remarkably convenient way of handling the data due to some simple mathematical properties of gaussians. First, the Fourier transform of a gaussian is another gaussian:

$$\int_{-\infty}^{\infty} e^{-a^2 x^2} e^{iky} dx = \int_0^{\infty} 2 e^{-a^2 x^2} \cos kx dx = e^{-k^2/4a^2} \quad (\text{IV-2})$$

This fact has its first application in the deconvolution of the measured profiles over the laser bandwidth. There is a general theorem which states<sup>19</sup> that if one has a function  $h(x)$  which is a convolution of two other functions:

$$h(x) = g(x) \otimes f(x) \equiv \int_{-\infty}^{\infty} g(x-t)f(t)dt$$

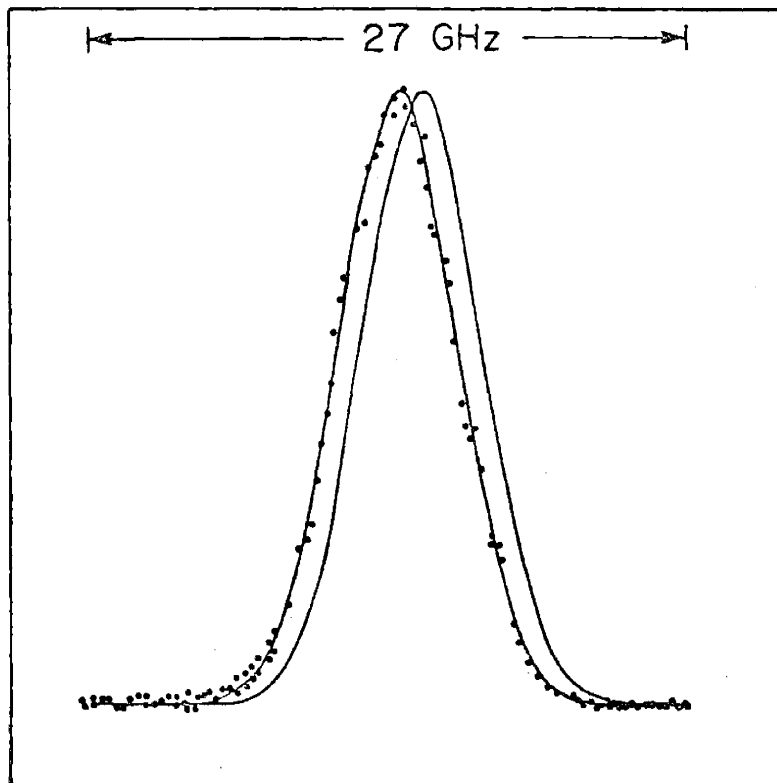
then,

$$g(x) = \text{FT} \left[ \frac{\text{FT}(h(x))}{\text{FT}(f(x))} \right] \quad (\text{IV-3})$$

where FT is to be read as "the Fourier transform of." Thus, if  $h(x)$  is our measured Doppler profile,  $f(x)$  is our laser bandwidth profile, we can deconvolute  $h(x)$  using the above theorem to get the true Doppler profile,  $g(x)$ . Now, since both our measured profile and our laser profile are well characterized by gaussian line shapes, we can use equations

Figure IV-3

Gaussian fit to OH R<sub>17</sub> (0,0) Doppler data illustrating both the data fit and the maximum magnitude of observed frequency shifts. Wavelength increases from left to right in the figure.



IV-2 and IV-3 to obtain the deconvolved Doppler profiles. For a measured distribution given by  $\exp(-a^2 x^2)$  and a laser profile given by  $\exp(-b^2 x^2)$  then, the deconvolved function is represented by  $\exp(-c^2 x^2)$  where  $1/c^2 = 1/a^2 - 1/b^2$ . The effect of this deconvolution on the data was small but observable.

The gaussian fits had an additional pleasing mathematical property which ensured ease in carrying out the necessary transforms. We begin with a set of Doppler profiles:

$$D(w_x, w_y, w_z) \sim \exp(-a^2 w_x^2 - b^2 w_y^2 - c^2 w_z^2) \quad (\text{IV-4})$$

The one dimensional Fourier transform yields

$$g(k_x, k_y, k_z) \sim \exp\left(-\frac{k_x^2}{a^2} - \frac{k_y^2}{b^2} - \frac{k_z^2}{c^2}\right)$$

or, 
$$g(k; \theta, \phi) \sim \exp\left[-k^2 \left(\frac{\sin^2 \theta \cos^2 \phi}{a^2} + \frac{\sin^2 \theta \sin^2 \phi}{b^2} + \frac{\cos^2 \theta}{c^2}\right)\right]$$

Now, if we invoke the known cylindrical symmetry, i.e.,  $a^2 = b^2$ , we have

$$g(k; \theta) \sim \exp\left[-k^2 \left(\frac{\sin^2 \theta}{a^2} + \frac{\cos^2 \theta}{c^2}\right)\right] \quad (\text{IV-5})$$

The back transform of this function gives

$$N(v, \theta) \sim \exp\left[-v^2 / \left(\frac{\sin^2 \theta}{a^2} + \frac{\cos^2 \theta}{c^2}\right)\right] \quad (\text{IV-6})$$

and, for the spherically symmetric case, i.e.,  $a^2 = b^2 = c^2$ , we have

$$N(v) \sim \exp(-a^2 v^2) \sim D(v) !! \quad (\text{IV-7})$$

In other words, if we assume the gaussian fit to the data and spherical symmetry, then the number density velocity-angle

distribution is identical to the measured Doppler profile. This result reflects the additional fortuitous mathematical property of gaussians: for any arbitrary three-dimensional gaussian distribution in any arbitrary coordinate system integration over two variables results in a gaussian distribution in the remaining variable. This fact is used in going from equation IV-5 to equation IV-6 in the above analysis.

Having determined the functional behavior of  $N(\underline{y})$ , we were able to characterize each distribution in terms of one gaussian parameter. The next step was to calculate the center of mass flux plots  $I(\underline{y}) = yN(\underline{y})$  and determine  $f(v)$  - the probability distribution for the product velocities. Figure IV-4 illustrates the definition of the vectors. We begin with

$$I(\underline{y}) = y \exp(-a^2 (\underline{y} - \underline{y}_0)^2)$$

where  $a^2$  is the exponential parameter determined from  $s_2$  for each profile and  $\underline{y}_0$  is the shift from  $v_{cm} = 0$ . Now, switching to polar coordinates gives

$$I(y, \theta, \phi) = y^3 \sin\theta \exp(-a^2 (y^2 - 2yy_0 \cos\theta + y_0^2))$$

and,

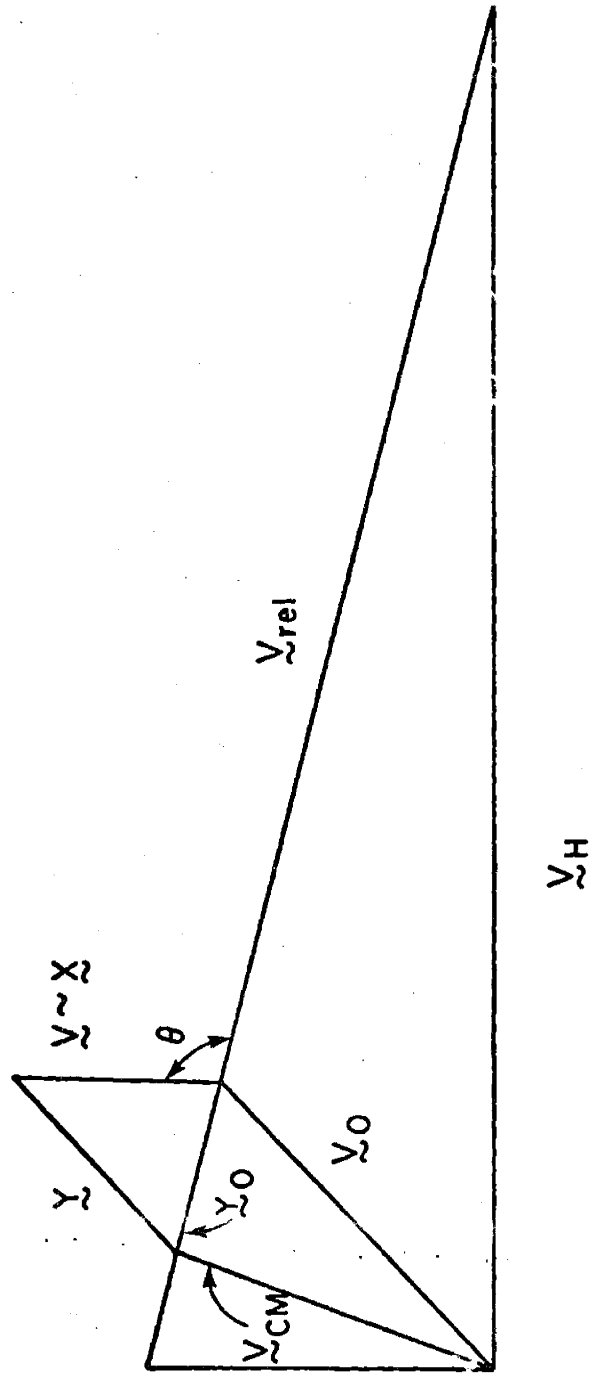
$$\begin{aligned} f(y) &= \frac{1}{2\pi} \int_0^{2\pi} d\phi \int_0^\pi d\theta I(y, \theta, \phi) \\ &= \frac{y^2}{2a^2 y_0} [\exp(-a^2 (y - y_0)^2) - \exp(-a^2 (y + y_0)^2)] . \end{aligned}$$

A flux diagram for the  $R_2(14)(0,0)$  OH transition is plotted in Figure IV-5 and plots of  $f(y)$  vs.  $y$  are shown in Figure IV-6.

The plots of Figure IV-6 make obvious that we had to pay a price for the convenience of the gaussian functionality. The arrows on these plots indicate the maximum allowed velocity for a particular internal state based on energy

Figure IV-4

Nominal Newton diagram to illustrate the various vectors used in the data analysis. Note that  $\bar{x}$  is a reduced variable equal to  $y/v_m$ .



$V \sim NO_2$

Figure IV-5

Flux contour diagram calculated based on a Gaussian fit to the OH R<sub>2</sub> 14 (0,0) data.



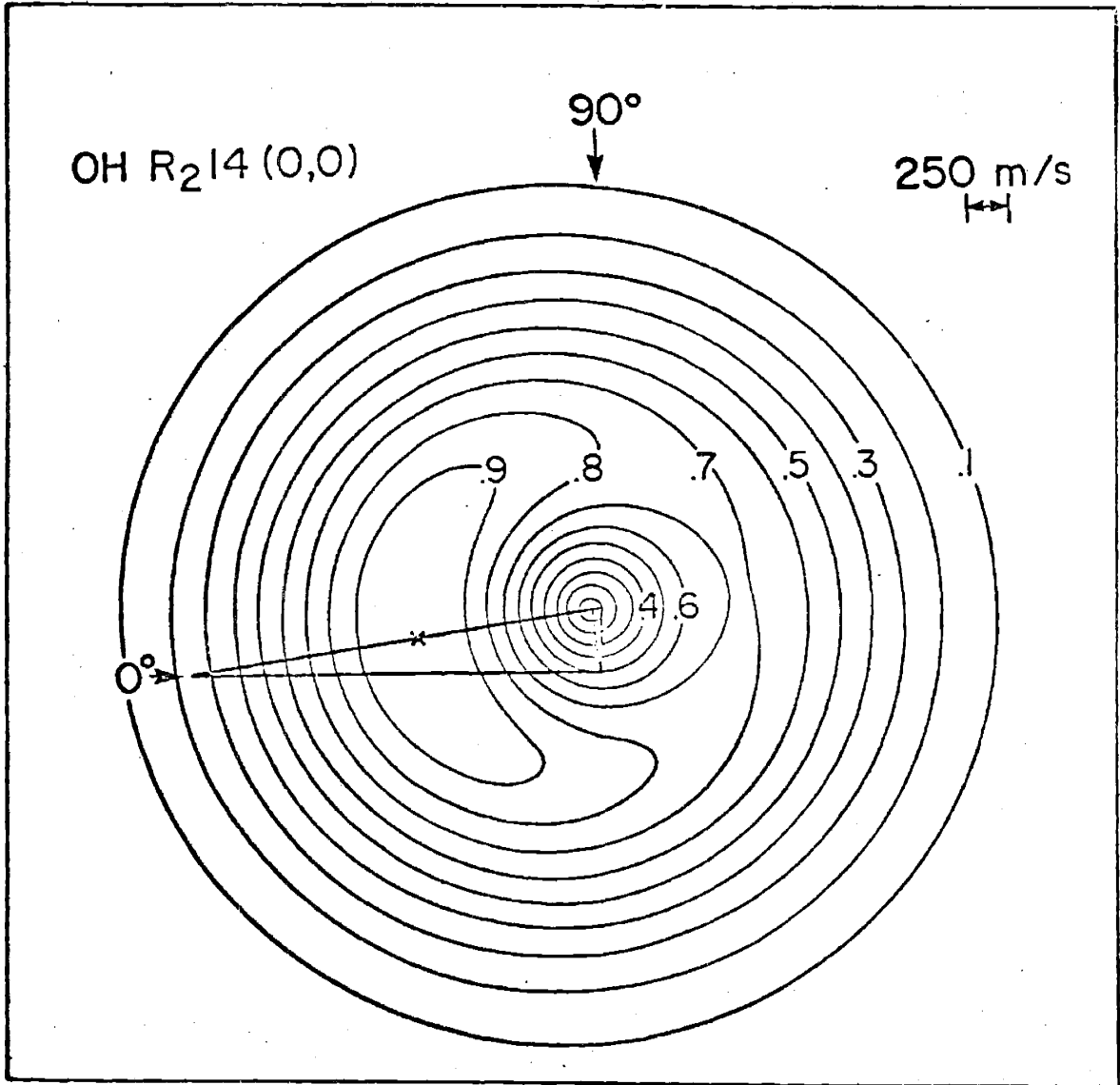
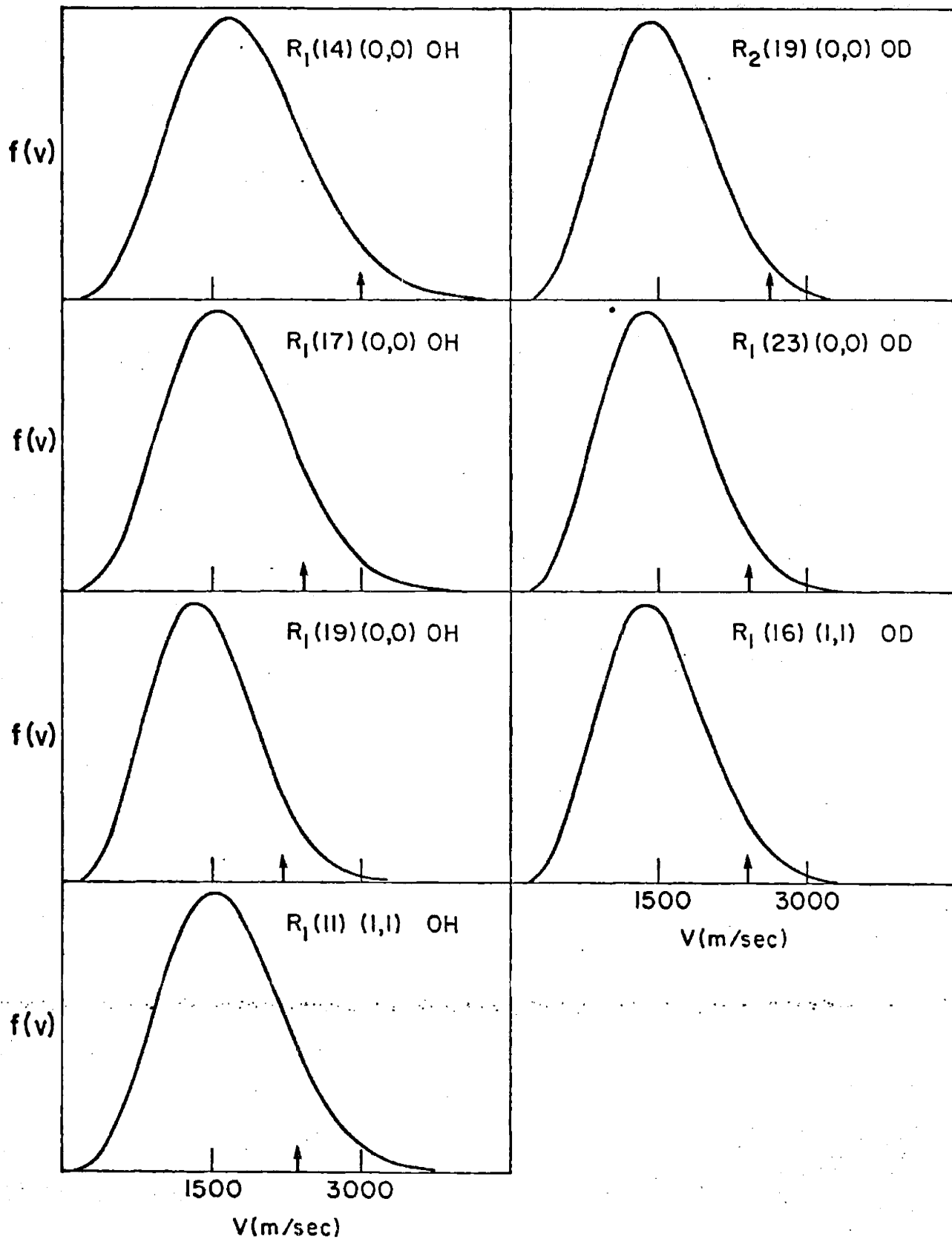


Figure IV-6

The velocity distributions,  $f(y)$ , calculated from the Gaussian fit parameters. The arrows indicate the highest velocities consistent with energy conservation.



conservation! The problem arises because the gaussians, although they get very close to zero for high velocities, never become identically zero. This effect is amplified in  $f(y)$  by the  $y^2$  term. The situation is even more serious for the calculation of the average energy in translation which is proportional to  $\langle y^2 \rangle$ . The gaussian analysis gave entirely unsatisfactory (large) values for translational energy disposal, so we attempted to find a new function which is constrained to satisfy the energy conservation limit.

### 3. Polynomial Fits to the Doppler Profiles

We began by trying very simple functional forms like  $D(v) = (1 - (v - v_0)^m)^n$  or, assuming spherical symmetry about the tip of  $v_0$  and expressing the function in terms of a reduced variable  $x = v/v_m$ ,  $D(x) = (1 - x^m)^n$ . Here,  $v_m$  is the maximum velocity allowed by energy conservation. Profiles were calculated for  $n$  from one through eight, for  $m$  from one through four, and for various values of  $v_m$ , but all of the resultant fits were found to be unacceptable. Polynomial expansions,  $\sum_n a_n x^n$  (where the coefficients were determined by constraining the function to reproduce the moments) were unsatisfactory due to unwanted oscillatory behavior.

The  $D(x) = (1 - x^2)^n$  function nearly fit the profiles but dropped off too quickly in the wings. The wings of the Doppler profiles are largely due to higher energy collisions, i.e., products with high velocities are most likely to be formed in collisions between reactants with greater than the average velocities and therefore greater than average accessible energies. This fact suggests that the Doppler profiles should not be characterized by a single  $v_m$  but rather,  $v_m$  should be a function of  $v$ . This consideration can be simply built into our polynomial fits and produces the desired effect of widening the wings of the profile.

The resulting functionality can be expressed as

$$D(x) = \left(1 - \frac{x^2}{(a+bx)^2}\right)^n. \quad \text{We determined the optimum values for}$$

the closely coupled parameters  $a$ ,  $b$ ,  $v_m$ , and  $n$  in the following manner. First,  $v_m$  was given a fixed value based on a reasonable estimate of the upper limit of the energy available to reaction products,  $E_{tot} = 2.3 \times 10^{-12}$  ergs/molecule.  $v_m$  is then given by

$$v_m = \left( \frac{2m_{NO}}{Mm_{OD}} (E_{tot} - E(v, J)) \right)^{1/2}$$

where  $m_{NO}$  and  $m_{OD}$  represent the masses of the products and  $M = m_{NO} + m_{OD}$ .

Next, the relations among  $a$ ,  $b$ , and  $n$  were determined. In order to insure that  $D(x=1) = 0$ , we must have  $\frac{a}{v_m} + b = 1$ . Using this relation we can determine values for  $a$  and  $b$  by constraining them to reproduce the observed HWHM (half width at half maximum) of the Doppler profiles.

$$D(x_{HWHM}) = \frac{1}{2} = \left( 1 - \frac{x_{HWHM}^2}{(a + bx_{HWHM})^2} \right)^n$$

or

$$a = \frac{c - 1}{\frac{1}{x_{HWHM}} - \frac{1}{v_m}}; \quad c = \left( 1 - \left( \frac{1}{2} \right)^{\frac{1}{n}} \right)^{-\frac{1}{2}}$$

The best value for  $n$  was empirically determined to be  $3/2$ . In fact,  $n$  is the only floating parameter in these fits as  $a$  and  $b$  are determined by normalization and the observed half width at half maximum and  $v_m$  is constrained by the accessible energy. Values of these parameters for each internal state are given in Table IV-2.

The resulting functions were then numerically convoluted over the laser band width. This convolution had only a slight effect. An example of the resulting fits is given in Figure IV-7. These fits actually were found to be far superior to the gaussian fits. They reproduced the half width at half maximum and the moments to a much higher degree of accuracy.

Internal State	a	$v_m$
OH R <sub>2</sub> 14 (0,0)	12.6	33.8
OH R <sub>1</sub> 17 (0,0)	11.2	30.0
OH R <sub>2</sub> 19 (0,0)	12.4	26.6
OH R <sub>1</sub> 11 (1,1)	11.2	29.0
OD R <sub>1</sub> 19 (0,0)	12.5	32.8
OD R <sub>1</sub> 23 (0,0)	10.8	29.2
OD R <sub>1</sub> 16 (1,1)	10.7	29.4

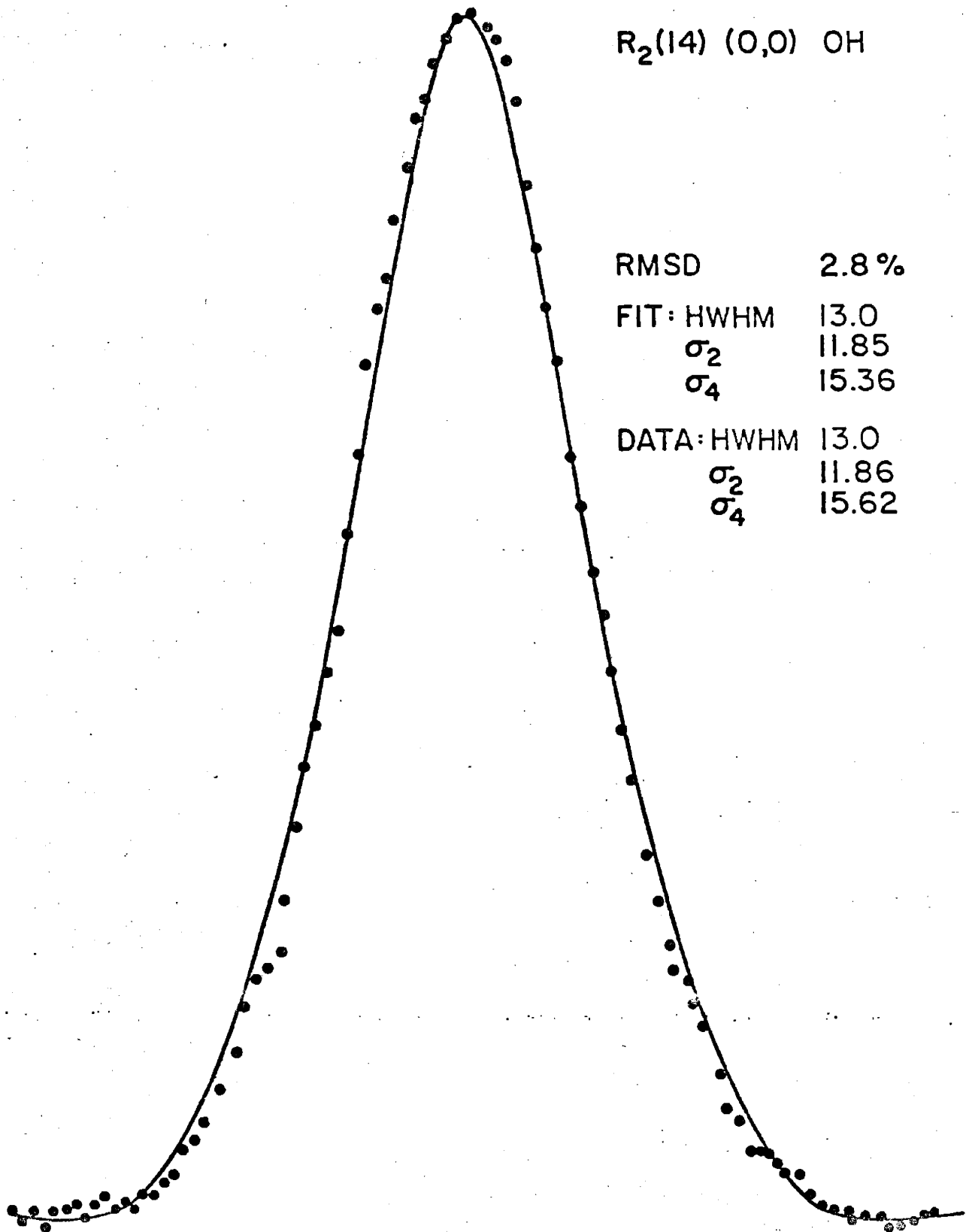
Table IV-2

Parameters for polynomial data fit. The numbers are given in units of bins in our multichannel array. One bin equals 78 m/s and equals 250 MHz.

Figure IV-7

Representative polynomial fit to Doppler data. Shown here is the fit for OH R<sub>2</sub>14 (0,0). The data points result from an average over a number of experiments.

R<sub>2</sub>(14) (0,0) OH



RMSD 2.8 %

FIT: HWHM 13.0  
 $\sigma_2$  11.85  
 $\sigma_4$  15.36

DATA: HWHM 13.0  
 $\sigma_2$  11.86  
 $\sigma_4$  15.62



## IVD. Results

### 1. Doppler Profile Inversion

Given the assumption of spherical symmetry, the Doppler profiles were found to be well characterized by

$$D(x) = \left(1 - \frac{x^2}{(a+bx)^2}\right)^{3/2} \quad (\text{IV-8})$$

as discussed in the previous section. The next step in the analysis is to obtain  $N(v)$  (or, equivalently  $N(x)$ ) from  $D(x)$ . The analysis is greatly simplified in the case of spherical symmetry. We begin by writing the Doppler profile observed for incident radiation directed along the  $v$  axis

$$D(v) = \int_0^{\infty} \int_0^{\infty} dv_x dv_y N(v_x, v_y, v) .$$

Rewriting in cylindrical coordinates and performing the integration over azimuthal angles,

$$D(v) = 2\pi \int_0^{\infty} u du N((u^2+v^2)^{1/2})$$

Then,

$$\begin{aligned} \frac{dD(v)}{dv} &= 2\pi \int_0^{\infty} u du N'((u^2+v^2)^{1/2}) \frac{v}{(u^2+v^2)^{1/2}} \\ &= 2\pi v \int_0^{\infty} \left(\frac{dF}{du}\right) du = 2\pi v N((u^2+v^2)^{1/2}) \Big|_0^{\infty} \end{aligned}$$

For a physically reasonable situation,  $N(\infty)$  must vanish and so we have the result of equation 11 of reference 6a

$$\frac{dD(v)}{dv} = -2\pi v N(v) \quad (\text{IV-9})$$

for spherically symmetric distributions. Thus, we need only take the derivative of the Doppler profiles to determine  $N(v)$ . The following discussion will return to use of the reduced variable,  $x = v/v_m$ .

From equations IV-8 and IV-9 we have,

$$N(x) = \frac{3a}{\pi} \left(1 - \left(\frac{x}{a+by}\right)^2\right)^{1/2} (a+bx)^{-3} \quad (\text{IV-10})$$

## 2. Velocity Distributions

The next step is to write the expression for the center of mass flux and to determine the probability distribution  $f(y)$ .  $y$  and  $y_0$  will hereafter also be defined as reduced variables in terms of  $v_m$ . The flux is given by

$$I(y) = yN(x) .$$

Figure IV-8 shows contour diagrams of several flux distributions. Writing in spherical coordinates and integrating over the azimuthal angle gives

$$I(y, \theta) = 6ay^3 \left(1 - \frac{h^2(y, \theta)}{a+b \cdot h(y, \theta)}\right)^{1/2} (a+b \cdot h(y, \theta))^{-3} \quad (\text{IV-11})$$

where

$$h(y, \theta) = (y^2 + y_0^2 - 2yy_0 \cos \theta)^{1/2} .$$

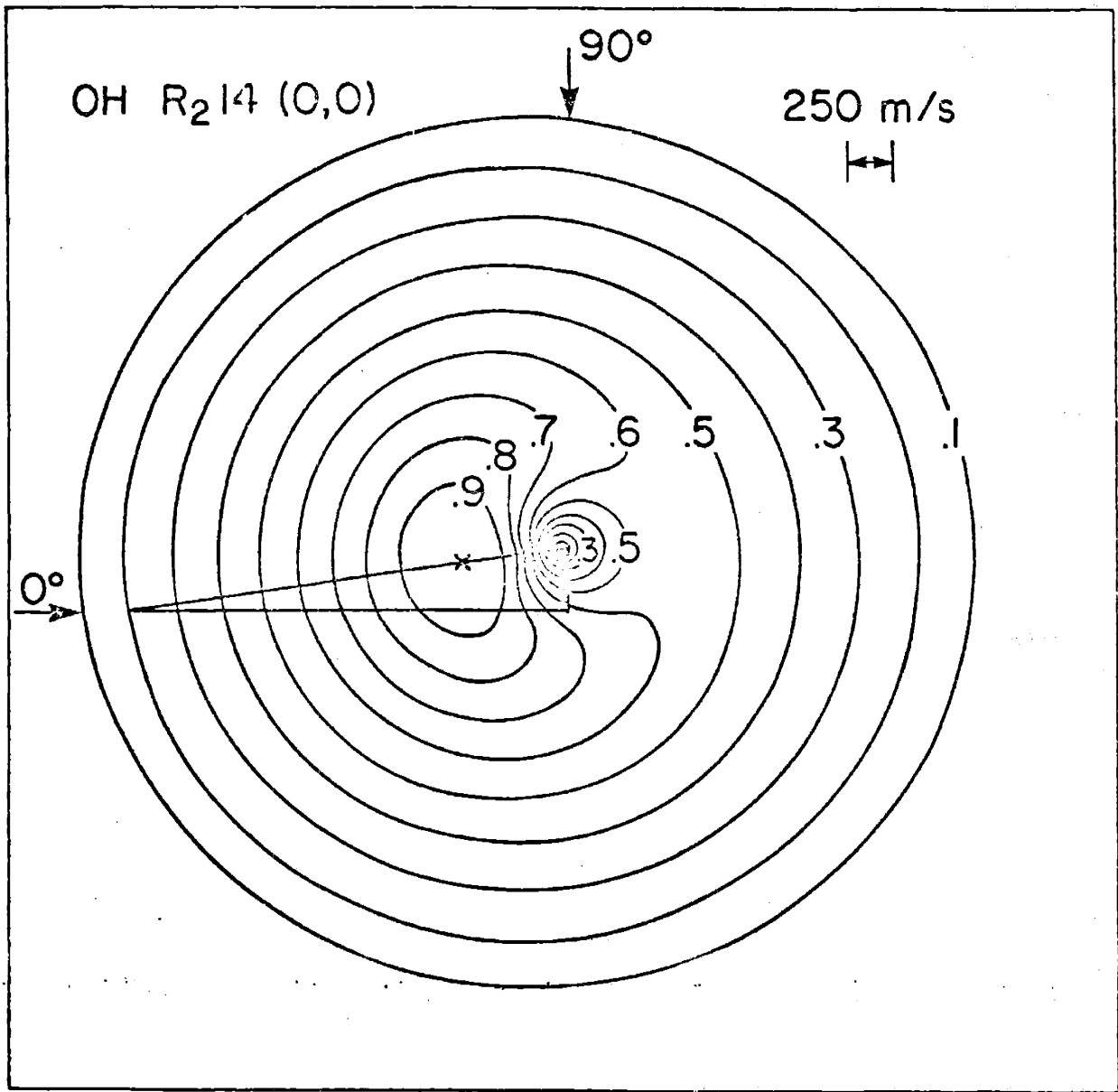
We want to determine

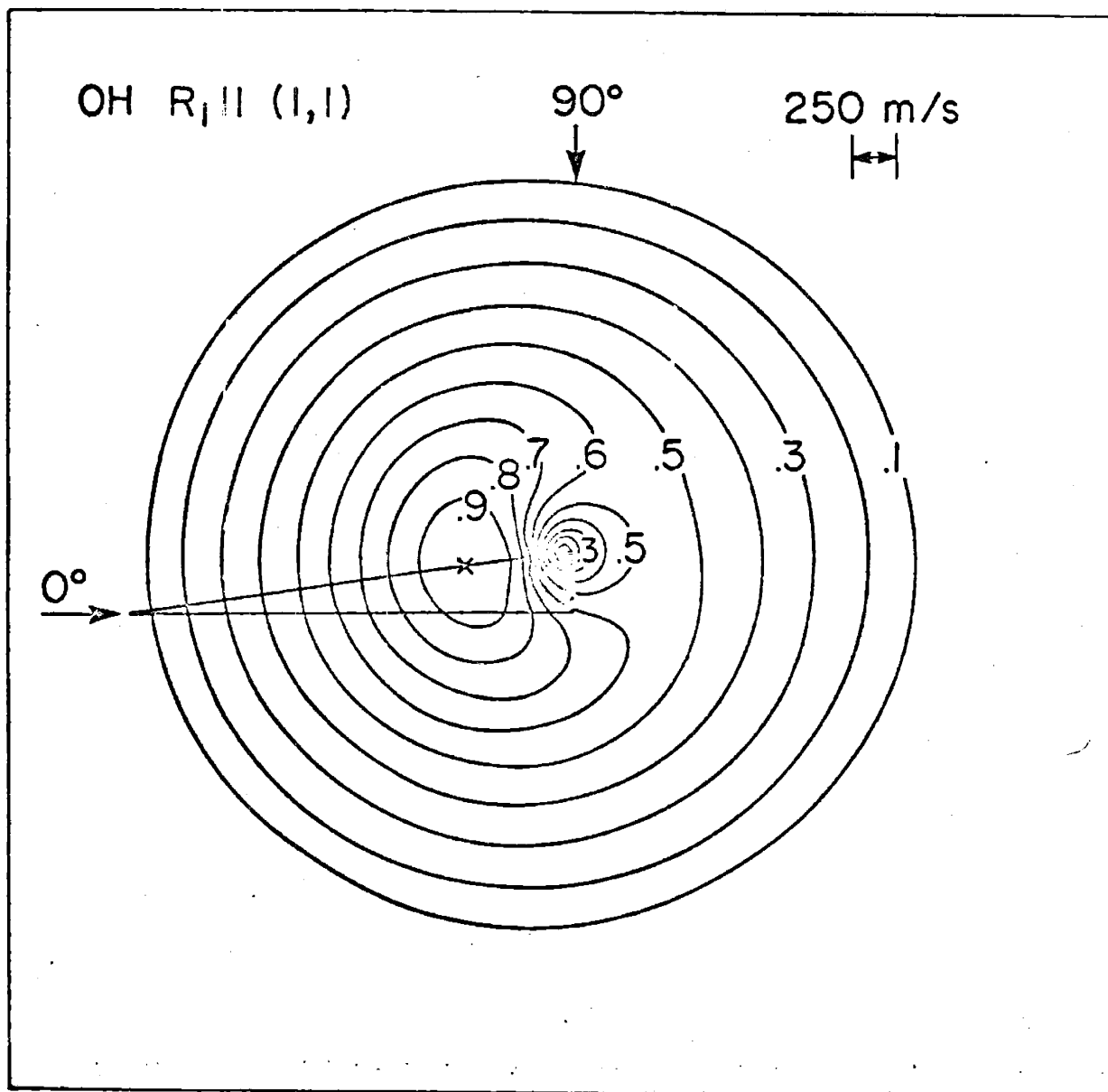
$$f(y) = \int_0^{\theta(y)} \sin \theta d\theta I(y, \theta) \quad (\text{IV-12})$$

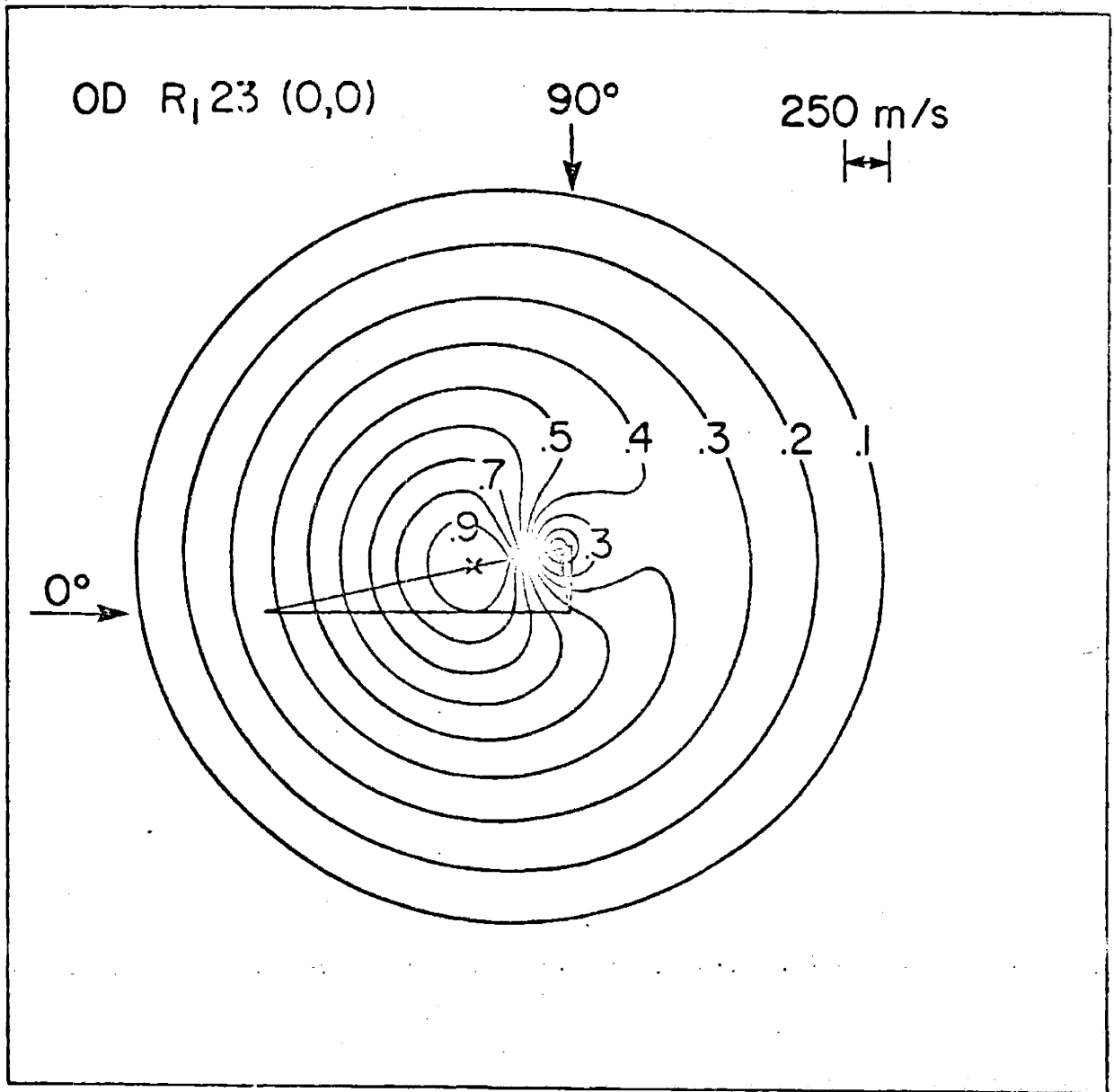
In order to ensure that  $f(y)$  behaves properly, care must be taken in evaluating  $f(y)$ . Recall that  $D(x)$  was defined as symmetric about the tip of  $y_0$  and bounded by a circle of radius  $v_m$ . The problem is illustrated with the aid of Figure IV-9. The range of  $\theta$  must be constrained such that for any combination of  $y$  and  $\theta$  only those regions within the solid circle will be sampled as only this region is consistent with the original definition of  $D(x)$ . We find then that  $y$  must range from 0 to  $v_m + y_0$  to include this entire area.

Figure IV-8a to IV-8d

Flux plots for several internal states calculated from the polynomial fit parameters.







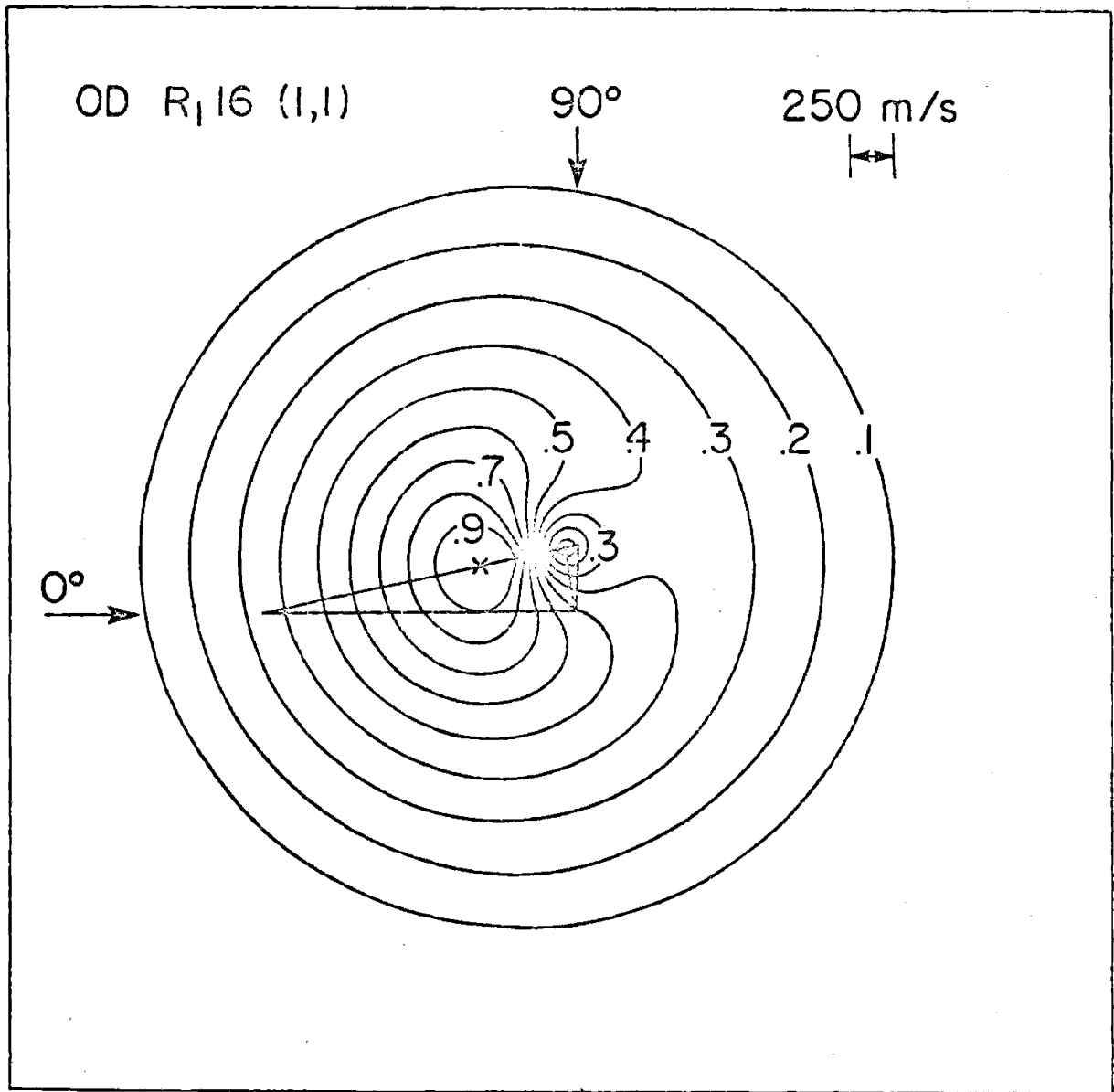
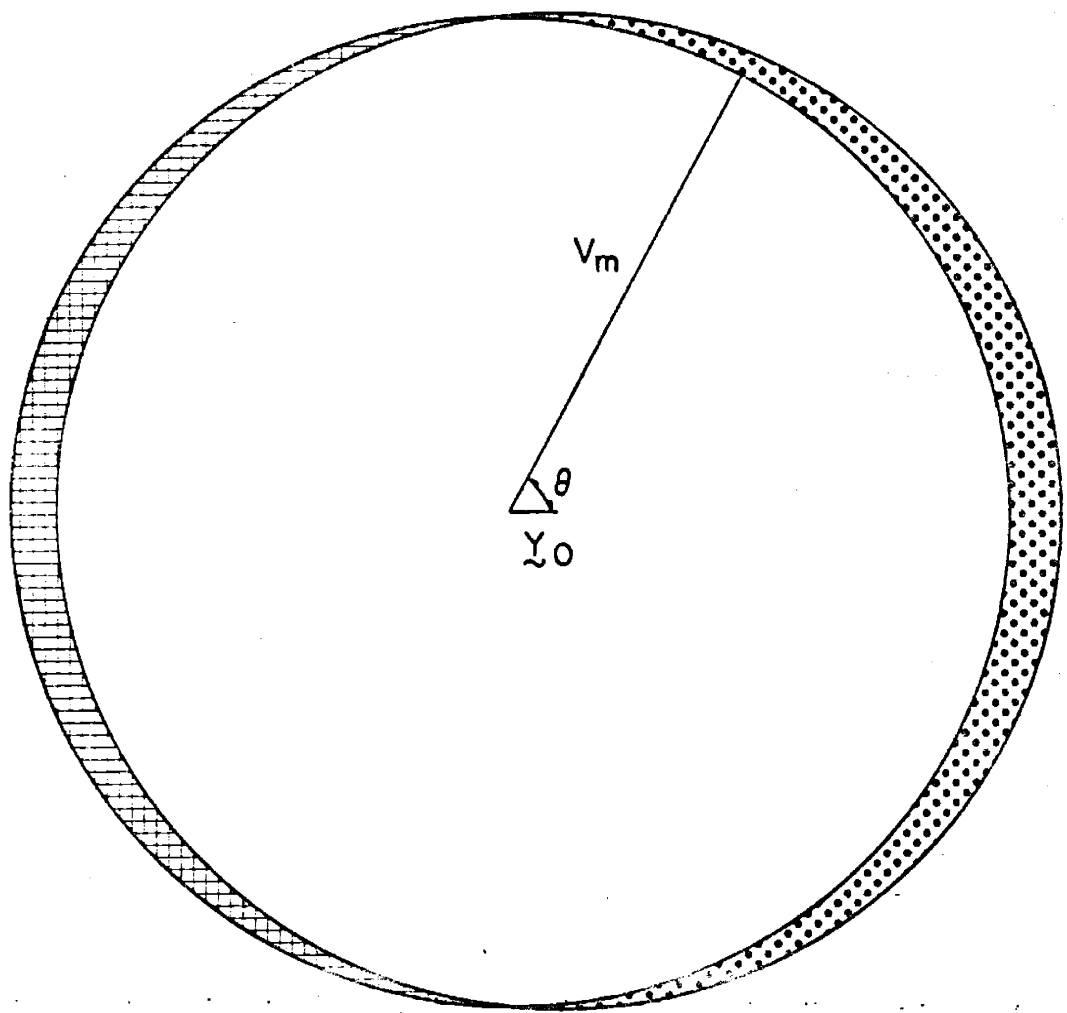


Figure IV-9

Figure for the illustration of the  $D(x)$ ,  $v_m$  symmetry problem. The relative magnitudes of  $v_m$  (the radius of both circles) and  $y_0$  (the distance between the centers of the circles) is consistent with experimental data.





For  $y \leq v_m - y_0$ , all values of  $\theta$  are possible and  $\theta$  ranges from zero to  $\pi$ . For  $v_m - y_0 < y \leq v_m + y_0$ ,  $y$  ranges from zero to  $\theta(y)$  where  $\theta(y)$  is that angle at which a circle of radius  $y$  drawn about the point  $y = 0$  intersects the circle of radius  $v_m$  drawn about the tip of  $y_0$ . This angle is given by

$$\theta(y) = \cos^{-1} \left[ \frac{y^2 - v_m^2 + y_0^2}{2yy_0} \right] \quad . \quad (IV-13)$$

Thus, a small region (the shaded region in Figure IV-9) which is outside the true  $v_m$  is included in  $f(y)$  while a small region which is within  $v_m$  is excluded (the cross hatched region in the figure). These two regions will produce errors which probably are of nearly equal magnitude but are of opposite effect. Between  $v_m - y_0$  and  $v_m$ , the area under  $f(y)$  is decreased while between  $v_m$  and  $v_m + y_0$  the area (which should be zero) is increased. Because  $y_0 \ll v_m$ , this effect should be minimal. In fact, in the calculation of  $\langle y^2 \rangle$  (discussed below) the estimate of the effect of this approximation is within the experimental uncertainty.

As an aside, it is interesting to note that the  $s_3$  moments (previously discussed in section IV-C1) did show a slight trend. To the careful and optimistic eye, there was a smooth variation from positive to negative values as one goes from  $\theta = 135^\circ$  back through  $\theta = 0^\circ$  to  $\theta = 315^\circ$  (see Figure IV-1 for angle definition). This trend is consistent with the asymmetry one would expect given that  $D(x)$  cannot be truly symmetric and still conserve energy. As this trend in the  $s_3$  moments was not well characterized quantitatively, it was not accounted for in the analysis.

Thus,  $f(y)$  is actually represented by two functions: the region  $0 \leq y \leq v_m - y_0$ , will be designated region one and  $v_m - y_0 < y \leq v_m + y_0$  will be designated region two. The integral of equation IV-12 was evaluated by making an "educated guess" at  $f(y, \theta)$  such that

$$\left(\frac{\partial f(y, \theta)}{\partial \theta}\right)_y = I(y, \theta) .$$

The limits were then applied to  $f(y, \theta)$  to obtain

$$f_1(y) = \frac{4y^2}{y_0} \left[ \left(1 - \left(\frac{y - y_0}{a + b(y - y_0)}\right)^2\right)^{3/2} - \left(1 - \left(\frac{y + y_0}{a + b(y + y_0)}\right)^2\right)^{3/2} \right] \quad (\text{IV-14})$$

and

$$f_2(y) = \frac{4y^2}{y_0} \left(1 - \left(\frac{y - y_0}{a + b(y - y_0)}\right)^2\right)^{3/2} . \quad (\text{IV-15})$$

Plots of  $f(y)$  are shown in Figure IV-10.

### 3. Average Translational Energy

In order to calculate the average translational energy, we calculate the integrals

$$\langle y^2 \rangle = \frac{\int_0^{\infty} y^2 f(y) dy}{\int_0^{\infty} f(y) dy} \quad (\text{IV-16})$$

and find  $\langle E_{\text{trans}} \rangle$  as

$$\langle E_{\text{trans}} \rangle = \frac{1}{2} M \frac{m_{\text{OD}}}{m_{\text{NO}}} \langle y^2 \rangle \quad (\text{IV-17})$$

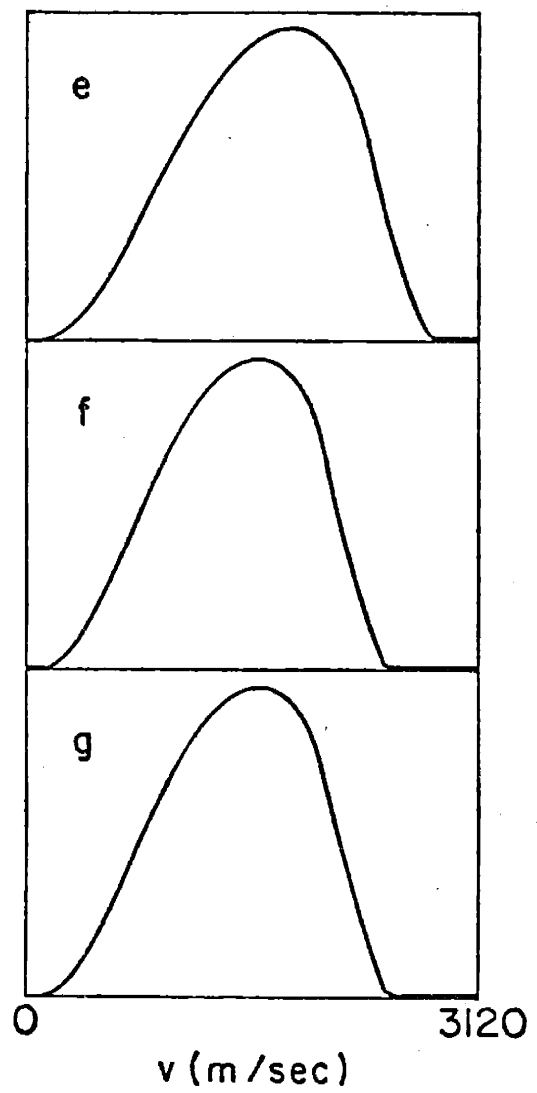
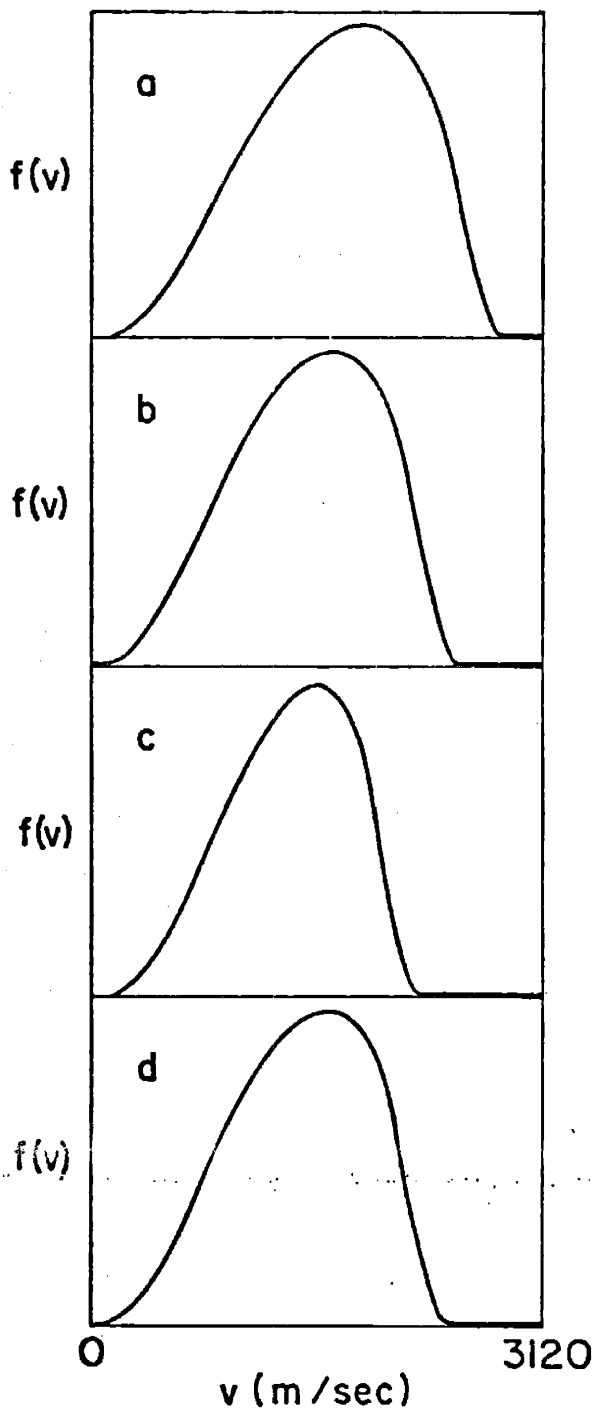
for each internal state. The integrals of equation IV-16 were evaluated numerically using the trapezoidal rule and  $y$  increments of 0.1 bins. The value for  $\langle E_{\text{trans}} \rangle$  for each internal state is given in Table IV-3 and

$f_{\text{trans}} = \langle E_{\text{trans}} \rangle / E_{\text{tot}}$  is plotted versus internal energy in Figure IV-11. The error bars were determined by recalculating  $f_{\text{trans}}$  while accounting for the experimental uncertainty in the FWHM ( $\pm 5\%$ ) and uncertainty in  $E_{\text{tot}}$  ( $\pm 500 \text{ cm}^{-1}$ ). The line through the points is a least squares fit to the data constrained to go through  $f_{\text{T}} = 0$  at  $E_{\text{tot}}$ . The result of this fit was:

Figure IV-10

The velocity distributions,  $f(y)$ , as a function of internal state calculated from the polynomial fit parameters.

- a) OH R<sub>2</sub>14 (0,0)
- b) OH R<sub>1</sub>17 (0,0)
- c) OH R<sub>2</sub>19 (0,0)
- d) OH R<sub>1</sub>11 (1,1)
- e) OD R<sub>1</sub>19 (0,0)
- f) OD R<sub>1</sub>23 (0,0)
- g) OD R<sub>1</sub>16 (1,1)



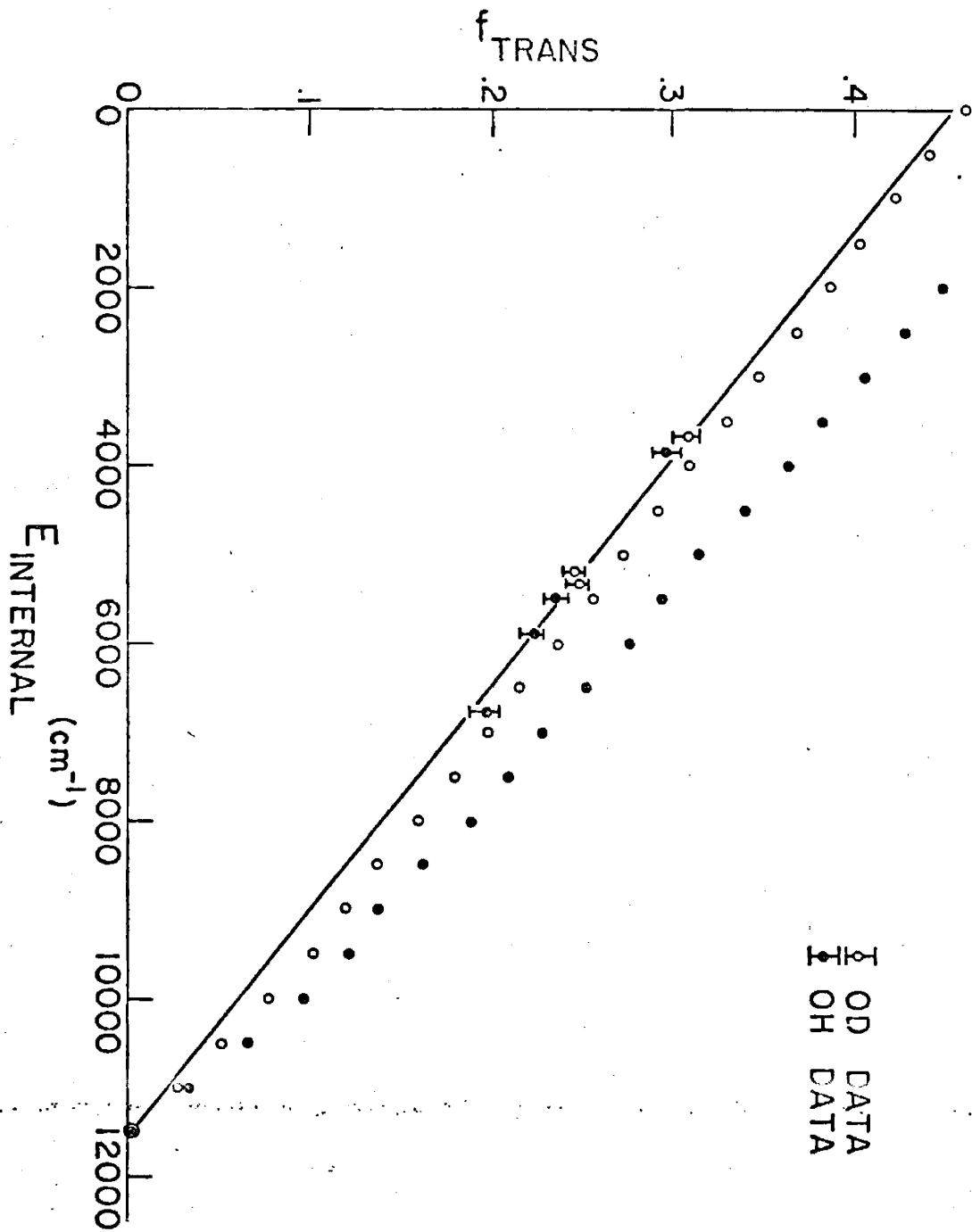
Internal State	Internal Energy ( $\text{cm}^{-1}$ )	$f_{\text{Trans}}$
OH R <sub>2</sub> 14 (0,0)	3841	.297
OH R <sub>1</sub> 17 (0,0)	5498	.235
OH R <sub>2</sub> 19 (0,0)	6776	.198
OH R <sub>1</sub> 11 (1,1)	5890	.222
OD R <sub>1</sub> 19 (0,0)	3689	.309
OD R <sub>1</sub> 23 (0,0)	5320	.245
OD R <sub>1</sub> 16 (1,1)	5230	.247

Table IV-3

Internal energy and fraction of energy in translation for each product state studied by the FTDS technique.

Figure IV-11

Plot of the fraction of available energy in translation versus internal energy. Points with error bars are the measured data. The other points are the result of a calculation and will be discussed in Chapter V.



○ OD DATA  
● OH DATA



$$f_T = 0.45(1 - E_I/E_{tot}) \quad (IV-18)$$

with a root mean square deviation of 0.004.

The results of the internal state measurements were then used in conjunction with equation IV-18 to determine the translational energy disposal averaged over internal states. We have

$$\langle f_T \rangle = \frac{\sum_i P(i) f_T(i)}{\sum_i P(i)} \quad (IV-19)$$

where the  $P(i)$ s are the induced probabilities of equation III-6 and the sum is over all internal states of a particular molecule. The distributions described by equation III-6 apply only to those levels probed by the  $R_1$  branch of the spectrum. However, we know that the upper ( $\lambda_u$ ) and lower ( $\lambda_l$ )  $\lambda$ -doublet levels are related by  $P_{\lambda_u} = 1.4 P_{\lambda_l}$  and that  $f_T(\lambda_u) \sim f_T(\lambda_l)$  because  $E_{\lambda_u} \sim E_{\lambda_l}$ . Thus the difference in  $\lambda$ -doublet propensities will cancel out of equation IV-19. The spin states are also nearly equivalent energetically, so that the spin state distribution can be accounted for by replacing  $P(i)$  in equation IV-19 by  $P(i)(1 + \frac{N}{N+1})$ . We find  $\langle f_T \rangle_{OD} = \langle f_T \rangle_{OH} = 0.25 \pm 0.02$ .

#### 4. Angular Distributions

The final step in the analysis of the Doppler data was the calculation of the angular distributions

$$f(\theta) \equiv \int_0^{y(\theta)} I(\underline{y}) dy \quad (IV-20)$$

where  $I(\underline{y})$  is given by equation IV-11. The integral was calculated numerically using the trapezoidal rule with velocity intervals of 0.1 bins for angles from  $0^\circ$  to  $180^\circ$  in  $10^\circ$  intervals. The integration limit is given by (see equation IV-13)

$$y(\theta) = y_0 \cos\theta + (v_m^2 + y_0^2 (\cos^2\theta - 1))^{1/2} .$$

Figure IV-12 shows plots of  $f(\theta)$  vs.  $\theta$  in the center of mass coordinate system. Each curve is normalized to  $f(\theta = 90^\circ) = 0.5$ . Integration over forward ( $\theta < 90^\circ$ ) and backward ( $\theta > 90^\circ$ ) angles shows approximately 60% of the OH product and 65% of the OD product to be scattered into the forward hemisphere. In order to probe the effect of the  $v_m$ ,  $D(x)$  symmetry problem as discussed in section IV-D2, angular distributions were calculated over the range  $0 \leq y \leq v_m - y_0$ . These results are identical to those of Figure IV-12.

#### IVE. Comparison to Other Data

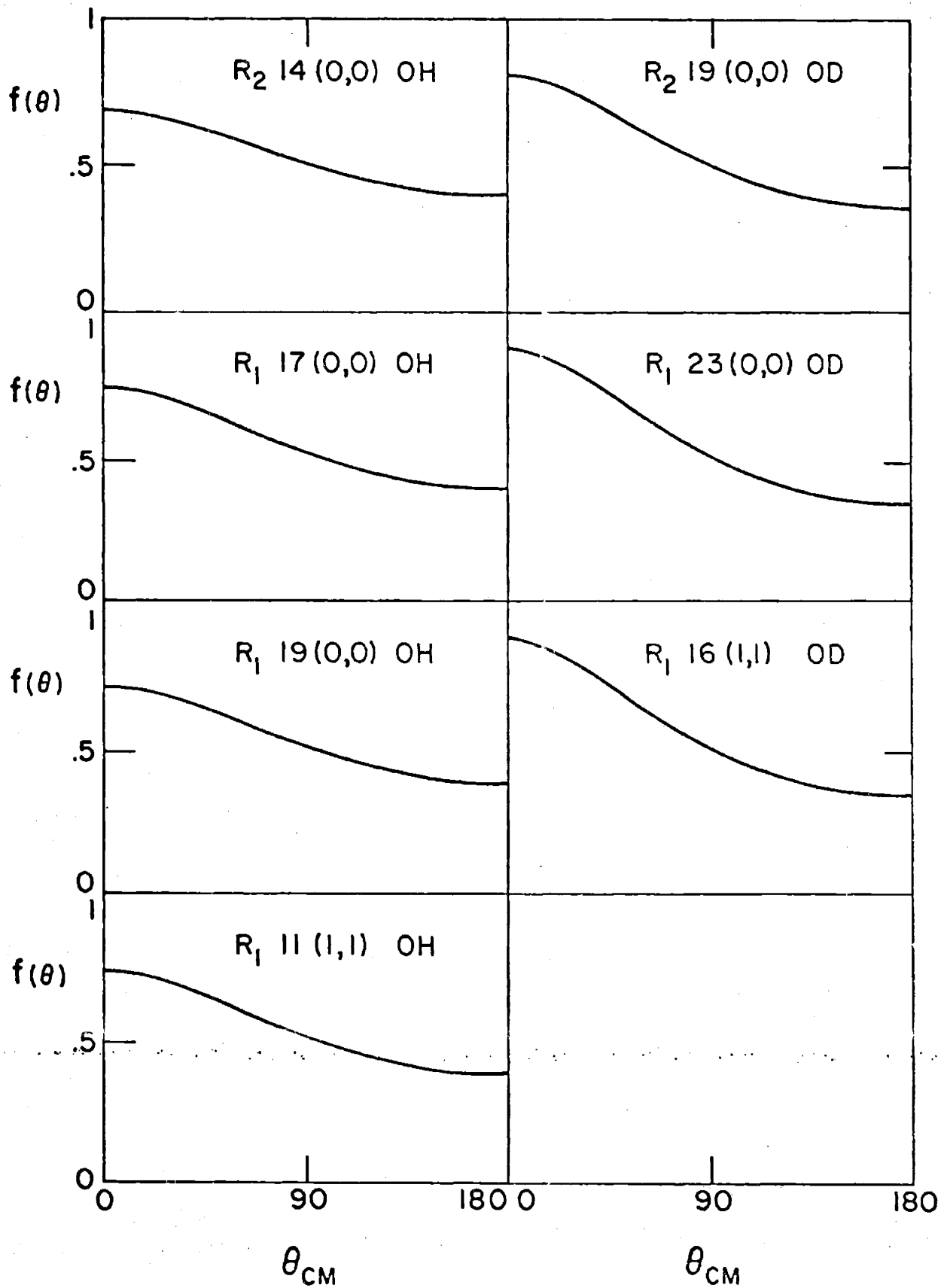
The  $H(D) + NO_2$  system was a natural and prudent choice for this first experimental study using the FTDS technique. The system has been studied in this laboratory for some time so that the spectroscopy of OH and OD was well understood and many of the experimental problems had been solved. A more important consideration is the fact that the velocity and angular distributions for this system has previously been studied<sup>(20)</sup> by the conventional technique and so our results can be compared directly to other data.

Despite the fact that our technique and experimental conditions differ significantly from those of Haberland,<sup>(20)</sup> there is excellent qualitative and quantitative agreement between the results. In the most recent publication, Haberland reports the following:

- (1)  $\langle f_T \rangle_{OD} \approx \langle f_T \rangle_{OH} = .21 \pm .03$ ;
- (2) the velocity distributions are isotopically independent and peak at 750 m/sec in the center of mass system;
- (3) most probable velocity is  $v_m/4$ ;
- (4) the angular distributions are nearly isotopically independent but may have a weak forward maximum in the center of mass system.

Figure IV-12

The angular distributions,  $f(\theta)$ , calculated from the polynomial fit parameters.



The important differences in the experiments are

(1) Haberland's technique is not sensitive to the internal state of the product molecules.

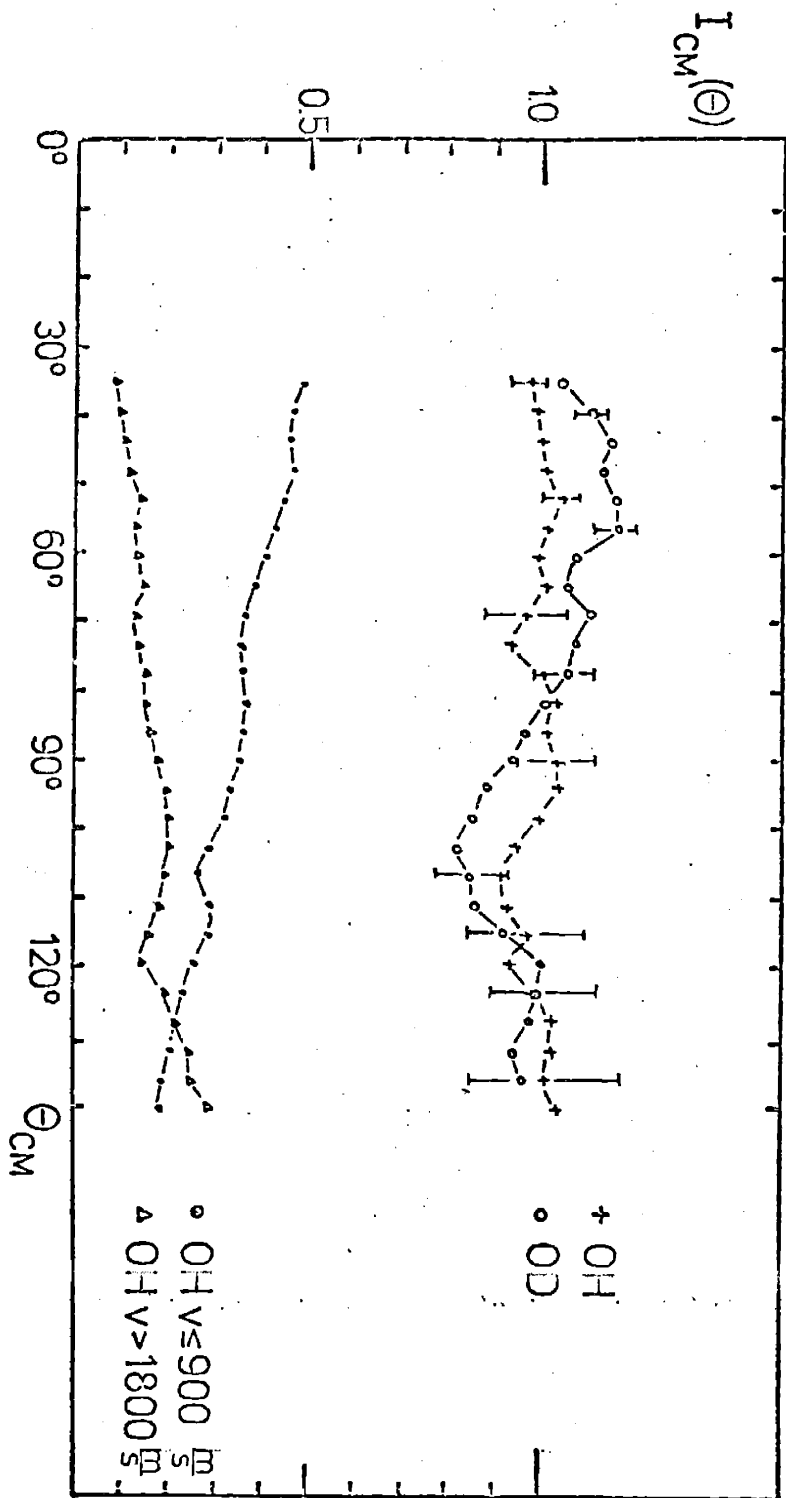
(2) Haberland uses a thermal dissociation source to produce the atomic reagent. The mean kinetic energy under his conditions is significantly higher than ours. Additionally, he will have a much broader spread in reactant velocities. The total available energy in these studies is approximately 75% of the available energy in Haberland's studies.

The agreement between the two determinations of  $\langle f_T \rangle$  is impressive given the difference in experimental conditions. Aside from the possibility of a reaction mechanism which depends weakly on initial kinetic energy, the uncertainties in our internal state probabilities or, the uncertainties in the total available energy are more than sufficient to account for the minor difference in the average translational energy results. A comparison of the velocity distributions shows additional impressive similarities. Aside from energetic constraints, our velocity distribution (Figure IV-10) are independent of isotope and internal state. Furthermore although the most probable product velocity (peak of the flux distribution) occurs at a lower absolute velocity (around 500 m/s) than measured by Haberland, the discrepancy is entirely explained in terms of the differences in total available energy. The position of the velocity maximum is a function of the internal state and occurs near  $v_m/4$  for all states!

At first glance, the observed angular distribution seem at odds, but a closer look helps to resolve this difficulty. The angular distribution plot taken from Haberland's most recent publication is shown in Figure IV-13. The upper curves show the angular distribution summed over all accessible velocities for both OH and OD to be essentially independent of angle. However, the first point to note is that their measurements have only sampled a range of angles between

Figure IV-13

Angular distributions for reactions 1a and 1b as reported  
in reference 20a.



$\theta = 30^\circ$  and  $\theta = 150^\circ$ . In our angular distributions which sample the entire angular range ( $0^\circ$  to  $180^\circ$ ) a slight forward scattering is clearly discernible. Because the variation of flux with angle in the  $30^\circ$ - $150^\circ$  range is on the order of Haberland's error bars quantitative data comparison is difficult. It is interesting that Haberland's data appear to be composed of two velocity groups with opposite angular dependences while we observe angular distributions without a strong velocity dependence. This result may be an experimental artifact relating to the speed and direction characteristics of the beam sources. However, it may also be due to the two fundamental differences in the experiments (state resolution and total energy) as mentioned above. The two velocity regions depicted in the lower curves of Figure IV-13 will result, on average, from different sets of internal states. In addition, the significant difference in total available energy due primarily to differences in the atomic reagent's linear momentum will effect the observed distributions if initial and final linear momenta are strongly coupled. At any rate, these results suggest that a study of the velocity-angle distributions as a function of initial energy (in various degrees of freedom) and of final internal state under well collimated beam conditions would provide a very detailed insight into the reaction mechanism.



## Chapter V. Conclusions

### VA. Background.

With the completion of these studies, Reactions 1a and 1b have become extremely well characterized experimentally. As discussed, a number of groups have utilized a variety of techniques which have probed the OD and OH products of these reactions. The agreement among the results is impressive. Unfortunately there is no tractable procedure for unraveling this detailed data in terms of a quantitative theoretical model. Rather we postulate a reaction model in qualitative classical terms. Before discussing the reaction scheme some background information will be presented. The reader is reminded that in all appropriate sections D and OD are used to symbolize both H,D and OH,OD respectively.

*Ab Initio* calculations have been done in an effort to determine the electronic structure of  $\text{NO}_2$ .<sup>(51)</sup> From a simple Walsh diagram analysis<sup>(52)</sup> the unpaired electron of  $\text{NO}_2$  is thought to be in an  $sp_2$  hybridized orbital on the nitrogen nucleus. However, the *ab initio* calculations which do not constrain the molecule to  $C_{2v}$  symmetry show higher electron density on the oxygen atoms as the molecule is bent from its equilibrium position. Guillory and Hunter<sup>(53)</sup> have studied the  $\text{H} + \text{NO}_2$  reaction in a solid argon matrix at approximately 10K. They observed production of an H-O-N-O species but no production of an H-N-O<sub>2</sub> species. If one assumes that the reaction is initiated by an interaction between the unpaired electrons which bends the  $\text{NO}_2$  from its equilibrium position then these studies are consistent with the electron configuration calculations.

Various isotopic nitrous acids (HONO) have been studied in the gas phase by infrared<sup>(54,55)</sup> and ultraviolet spectroscopy.<sup>(56,57)</sup> Again, H-N-O<sub>2</sub> is not observed but *cis* and *trans* isomers of H-O-N-O have been spectrally assigned. The *trans* form has been determined to be approximately 500 cal/mole more stable than the *cis* form and the barrier to internal

rotation has been estimated to be 11.5 kcal/mole above the *trans* equilibrium level with the maxima occurring at azimuthal angles of  $\pm 88^\circ$  from the position. To our knowledge no information on the shape of these potential wells is available.

As mentioned in Chapter III, the OD product is observed to preferentially populate the energetically higher lambda doublet level. (Mariella et al<sup>(41,44)</sup> incorrectly assign the preferentially populated level as the lower level.) The physical difference between the two lambda doublets is in the orientation of the lobes of the unpaired electron relative to the plane of molecular rotation. The higher energy level has this electron lobe in the plane of molecular rotation while the electron lobe is perpendicular to that plane for the lower energy state.<sup>(42b,43)</sup> A propensity for the upper lambda level has also been observed for low J states of OH produced in Reaction 1b under multiple collision conditions.<sup>(42)</sup> In addition it has been postulated that the reaction  $H + H_2O$  produces atmospheric OH maser emission by preferentially populating the upper lambda doublets of low J states.<sup>(43)</sup> For the sake of completeness, it should be noted that inelastic collisional processes have been postulated as a source of lambda doublet inversion for OH and CH<sup>(58-61)</sup> and that energy transfer processes which have lambda state dependent cross sections have been observed in  $Li_2(B^1\Pi)$ .<sup>(62,63)</sup>

Although there is a marked dearth of detailed information on  $A + BCD \rightarrow AB + CD$  reactions, a few specific systems have been discussed in the literature. The systems<sup>(13,64)</sup>  $O + CS_2$ ,  $O + NO_2$ ,  $O + ClO_2$ ,  $H + NOCl$ ,  $H + O_3$ , and  $H + ClO_2$ <sup>(44)</sup> all manifest a significantly greater fraction of the available energy in vibration of the 'new' (AB) bond than in the 'old' (CD) bond. The reaction  $Li + NO_2$ <sup>(65)</sup> has been studied using a magnetic deflection technique; nearly half of its available energy is channeled into product translation. Thus all of these systems apparently react via a direct mechanism.

The  $D + NO_2$  reaction differs from these systems in that a large fraction ( $\sim 30\%$ ) of the reaction exoergicity appears as NO internal energy.

Since angular momentum conservation prevents any significant NO rotational excitation, <sup>(44)</sup> this reaction appears to place nearly equal amounts of energy in the 'old' (NO) bond and in the 'new' (OD) bond. Hence the dynamics of Reactions 1a and 1b differ significantly from that of the systems mentioned in the preceding paragraph.

#### VB. Reaction Scheme.

The reaction scheme to be discussed here is based on ideas originally suggested by Mariella et al. <sup>(44)</sup> It will be presented in a series of steps corresponding to the actual evolution of a single reactive collision.

The initial approach of the reactant atom and molecule is considered to involve an interaction due to the presence of an unpaired electron on each reagent. This electron interaction presumably occurs on a singlet surface as such an interaction on a triplet surface would involve initial repulsion and the reaction is known to have no significant activation barrier. Next, a planar intermediate results as the deep potential wells of DONO are sampled. After a lifetime on the order of a rotational period (approximately 3 psec) the intermediate undergoes a coplanar dissociation to form the product molecules. In other words, the force which breaks apart the intermediate is exerted primarily along the breaking NO bond. Since no force is exerted perpendicular to the plane, the product molecules are constrained to rotate in the plane defined by the intermediate. This orientation constraint is in a molecule fixed coordinate system and is not observable in the laboratory frame as all molecular orientations are possible under our experimental conditions.

This simple scheme qualitatively accounts for all of the observed data. The formation of a short lived intermediate complex results in the nearly isotropic angular distribution. The formation of an intermediate is not inconsistent with the large amount of internal energy (greater than statistical) imparted to the OD. <sup>(68,69)</sup> The suggestion that this intermediate is planar is based on the known stability of DONO. The large barrier to internal rotation suggests that this species is strongly confined to a plane. The experimental observation that one lambda doublet, that which has its unpaired electron in the plane of molecular rotation,

is preferentially populated implies a coplanar dissociation; the unpaired electron, which results from the broken NO bond, has an enhanced probability of occupying a lobe in the plane of the intermediate and hence, in the plane of molecular rotation. Unfortunately there is no way to quantitatively predict vibrational and rotational distributions from this simple reaction scheme. However, the information theoretic analysis which included a coplanar constraint through the removal of the rotational degeneracy term can at least provide a consistency check. The compacting of the large data sets (given this coplanar trajectory) to two simple parameters is compelling. As such, the information theoretic result completes the entirely self consistent picture of this reaction scheme. Finally, neither the model nor the data contains a spin state preference.

#### VC. Discussion

In this final section, a few additional thoughts on the reaction scheme will be presented.

First of all, it should be noted that in addition to the conventional and modified information theoretic analyses discussed above we did conduct another such analysis based on a third reaction model. This idea was couched in terms of a DIPR - like (direct interaction with product repulsion) model. <sup>(72,73)</sup> If we consider a deuterium atom approaching an NO<sub>2</sub> molecule at some arbitrary angle, there is a plane defined by the deuterium, the nitrogen and the closest oxygen atom:



The other oxygen atom is randomly oriented relative to this plane. If product repulsion occurs along the planar NO bond, the OD product will be constrained to rotate in the plane but the NO product is free to take any orientation relative to that plane. Thus the OD rotational degeneracy is restricted without any corresponding restriction on the NO degeneracy. Although information theoretic analysis based on this scheme also resulted in simple parameterization, this model could be ruled out because we observe a forward scattered angular distribution with respect to the atomic reagent. Simple steric and kinematic considerations show that the DIPR - like model would result in predominately sideways and backwards scattering.

In Figure IV-11 we have shown a plot of the observed product translational energy as a function of internal energy. The open circles on the graph are the result of statistical calculation; using the conventional prior of Chapter III we have:

$$f_t(E_I) = \frac{\sum_i [(2N_{NO} + 1) \rho(E_t) E_t] / E_{Tot}}{\sum_i [(2N_{NO} + 1) \rho(E_t)]}$$

where the summation ranges over energetically accessible NO states. The filled circles are the result of another statistical calculation; using the modified prior of Chapter III we have:

$$f_t(E_I) = \frac{\sum_i [\rho(E_t) E_t] / E_{Tot}}{\sum_i [\rho(E_t)]}$$

In both of these equations  $f_t(E_I)$  is the fraction of energy in translation for OD internal state I,  $\rho(E_t)$  is the density of translational states at energy  $E_t$  ( $=E_{Tot} - E_I - E_i$ ),  $E_{Tot}$  is the total available energy and  $E_i$  is the energy of the 'i'th NO state.

The experimental results mimic very closely the statistical results which assumed no degeneracy restriction and they fall below the results which include this constraint. However since we know that the OD vibrational and rotational degrees of freedom and the NO vibrational degree of freedom receive more than a statistical amount of energy we expect that translational and NO rotational degrees of freedom must receive a less than statistical amount of energy. These calculations are thus consistent with the overall reaction scheme.

Preliminary results on the reaction  $O(^1D) + NH_3(ND_3) \rightarrow OH(OD) + NH_2(ND_2)$  also show a lambda doublet propensity.<sup>(74)</sup> A possible intermediate in this reaction,  $H_2-N-O-H$ , is known to have a stable 'chair' configuration (which has a 12 kcal/mole barrier to internal rotation).<sup>(75)</sup> Given these facts and the results presented in this thesis one can postulate that lambda doublet propensities might provide a probe of orientational constraints on reaction intermediates.

As in many other studies of reaction dynamics, the results of this work suggest additional experiments. First, the OD and OH products of Reactions 1a and 1b have been extensively studied. However, there are currently no results available on the NO product. Although one can infer the degree of energy disposal into NO from conservation laws, experimental confirmation would be preferable. Moreover, observation of a lambda doublet propensity in the  $X^2\Pi$  state of NO would corroborate this observation for OD and OH. Unfortunately, NO does not lend itself readily to LIF as it absorbs in an inconvenient spectral region and, attempts to observe infrared chemiluminescence from Reaction 1b have, to this time, been unsuccessful. <sup>(70)</sup>

The importance of reagent orientation and product alignment in reaction dynamics has been discussed <sup>(22,35)</sup> and demonstrated in the literature. <sup>(34,71)</sup> McClelland and Herschbach <sup>(36)</sup> have emphasized that measurements of vector quantities (ie angular distributions, molecular orientation) provide a more direct insight into the potential surface than do scalar measurements (ie state distributions). This fact is underscored by the detailed analysis necessary to interpret our state distributions and the much more straight-forward interpretation of our FTDS results. Although the lambda doublet argument and the surprisal analysis provide a novel method for inferring alignment constraints, a measurement of this apparently planar trajectory (planar in a molecule fixed frame) in the laboratory coordinate system would firmly establish the proposed mechanism. Although one can conceive of experiments which would provide a direct probe of any alignment constraints on Reactions 1 (ie aligning the  $\text{NO}_2$  reagent and probing OD,OH orientation or, possibly correlating OD,OH signals with NO signals and determining any correlation between the molecular orientations) such experiments are not feasible in the foreseeable future.

## REFERENCES

1. J.A. Silver; Ph.D. Thesis, Massachusetts Institute of Technology, (1976).
2. G.S. Arnold; Ph.D. Thesis, Massachusetts Institute of Technology, (1978).
3. J.A. Silver, W.L. Dimpfl, J.H. Brophy, J.L. Kinsey; *J. Chem. Phys.* 65, 1811 (1976).
4. E.J. Murphy, J.H. Brophy; *Rev. Sci. Instrum.* 50, 635, (1979).
5. F.C. Fehsenfeld, R.M. Evenson, H.P. Broida; *Rev. Sci. Instrum.* 36, 294 (1965).
6. S. Ramo, J.R. Whinnery; Fields and Waves in Modern Radio, Wiley, New York, (1953), p. 439.
7. A. Yariv, Introduction to Optical Electronics, Holt, Rinehart and Winston, New York, (1971).
8. M.A.D. Fluendy, K.P. Lawley; "Chemical Applications of Molecular Beam Scattering", Chapman and Hall, London, (1973) Chapter 3.
9. N.F. Ramsey; "Molecular Beams", Oxford University Press, London, (1956).
10. H. Pauly, J.P. Toennies in Advances in Atomic and Molecular Physics; D.R. Bates and I. Estermann, ed.; Vol. 1, p. 197; Academic Press, New York, (1965).
11. J. Ross, ed.; Advances in Chemical Physics - Molecular Beams, Vol. 10; Wiley and Sons, New York, (1966).
12. J.L. Kinsey in MTP International Review of Science; J.C. Polanyi, ed. Vol. 9, Chap. 6; Butterworths, London, (1972).
13. M.R. Levy in Progress in Reaction Kinetics, Vol. 10; Pergamon Press, Great Britain, (1979).
14. W.R. Gentry, C.F. Giese; *J. Chem. Phys.* 67, 5389, (1977).
15. J.L. Kinsey; *J. Chem. Phys.* 66, 2560, (1977).
16. J.L. Kinsey; ACS Symposium Series, No. 56, P.R. Brooks, E.F. Hayes, ed., (1977).
17. W.D. Phillips, J.A. Serri, D.J. Ely, D.E. Pritchard, K.R. Way, J.L. Kinsey; *Phys. Rev. Lett.*, 41, 937, (1978).
18. T.T. Warnock, R.B. Bernstein; *J. Chem. Phys.* 49, 1878, (1968); 51, 4682, (1969).
19. R. Bracewell; The Fourier Transform and Its Applications, McGraw-Hill, New York, (1965). An excellent general introduction.

20. a) H. Haberland, W. von Lucadou, P. Rohwer; preprint submitted to *Berichte der Bunsengesellschaft für Physikalische Chemie* (1979).  
b) H. Haberland, P. Rohwer, K. Schmidt; *Chem. Phys.* 5, 298, (1974).
21. R.N. Zare and P.J. Dagdigian; *Science*, 185, 739, (1974).
22. J.L. Kinsey in *Ann. Rev. Phys. Chem.* 28, 349, (1977).
23. a) L. Brillouin; *Science and Information Theory*, Academic Press, New York, (1962).  
b) E.T. Jaynes; *Phys. Rev.* 108, 171, (1957).
24. R.D. Levine, R.B. Bernstein; *Acct Chem. Res.* 7, 393, (1974).
25. R.D. Levine, J.L. Kinsey in *Atom - Molecule Collision Theory*, R.B. Bernstein, ed., Plenum Press, New York, (1979).
26. J.A. Serri, A. Morales, W. Moskowitz, D.E. Pritchard, C.H. Becker, J.L. Kinsey; *J. Chem. Phys.*, in press (1980).
27. a) M.E. Rose; *Elementary Theory of Angular Momentum*, Wiley, New York, (1955).  
b) M.E. Rose; *Multipole Fields*, Wiley, New York, (1955).
28. P.P. Feofilov; *The Physical Basis of Polarized Emission*, Consultants Bureau Enterprises, Inc., (1961).
29. A.R. Edmonds; *Angular Momentum in Quantum Mechanics*, Princeton Univ. Press, Princeton, New Jersey, (1960).
30. W. Shurcliff; *Polarized Light*, Harvard Univ. Press, Cambridge, Massachusetts, (1962).
31. D.A. Case, G.M. McClelland, D.R. Herschbach; *Mol. Phys.* 35, 541, (1978).
32. a) M.P. Sinha, C.D. Caldwell, R.N. Zare; *J. Chem. Phys.* 61, 491, (1974).  
b) S.R. Jeyes, A.J. McCaffery, M.D. Rowe; *Mol. Phys.* 36, 1865, (1978).
33. P.R. Brooks; *J. Chem. Phys.* 50, 5031, (1969).
34. D.S.Y. Hsu, N.D. Weinstein, D.R. Herschbach; *Mol. Phys.* 29, 257, (1975).
35. A. Kafri, R. Kosloff; *Chem Phys.* 23, 257, (1977).
36. G.M. McClelland, D.R. Herschbach; preprint 1979, submitted to *J. Chem. Phys.*
37. A. Messiah; *Quantum Mechanics*, John Wiley, New York, (1958).
38. J.L. Kinsey; in *Ann. Rev. Phys. Chem.* 28, 349, (1977).
39. W. L. Dimpfl, J.L. Kinsey; *J. Quant Spectrosc. Radiat. Transfer* 21, 233, (1979).
40. A.G. Visser, J.P. Bekooij, L.K. van der Meij, C. de Vreugd, J. Korving; *Chem. Phys.* 20, 391, (1977).
41. R.P. Mariella, A.C. Luntz; *J. Chem. Phys.* 67, 5388, (1977).



42. a) J.J. ter Meulen, W.L. Meerts, G.W.M. van Mierlo, A. Dymanus; *Phys. Rev. Lett.* 36, 1031, (1976).  
 b) J.J. ter Meulen; Ph.D. Thesis, Fysich Laboratorium, Katholieke Universiteit, Nijmegen, The Netherlands, (1975).
43. W.D. Gwinn, B.E. Turner, W.M. Goss, G.L. Blackman; *Astrophys. J.* 179, 789, (1973).
44. R.D. Mariella, B. Lantzsich, V.T. Maxson, A.C. Luntz; *J. Chem. Phys.* 69, 5411, (1978).
45. K.P. Huber, G. Herzberg; Constants of Diatomic Molecules, Van Nostrand, New York, (1979).
46. R.D. Levine, B.R. Johnson, R.B. Bernstein; *Chem Phys. Lett.* 19, 1, (1973).
47. a) J.C. Polanyi, J.J. Sloan; Int. J. of Chem.Kinetics, p. 55, Wiley, New York, (1975).  
 b) M.A. Nazer, J.C. Polanyi, W.J. Skrlac; J.J. Sloan, *Chem. Phys.* 16, 411, (1976).
48. J.E. Spencer, G.P. Glass; *Chem. Phys.* 15, 35, (1976).
49. G. Herzberg; Spectra of Diatomic Molecules, Van Nostrand, New York, (1950).
50. G.R. Fowles; Introduction to Modern Optics, Holt, Rinehart and Winston, New York, (1975).
51. C.F. Jackels, E.R. Davidson; *J. Chem. Phys.* 63, 4672, (1975); 64, 2908, (1976).
52. A.D. Walsh; *J. Chem Soc.* 2272, (1953).
53. W.A. Guillory, C.E. Hunter; *J. Chem. Phys.* 54, 598, (1971).
54. L.H. Jones, R.M. Badger, G.E. Moore; *J. Chem. Phys.* 19, 1599, (1951).
55. G.E. McGraw, D.L. Bernitt, I.C. Hisatune; *J. Chem. Phys.* 45, 1392, (1966).
56. G. W. King, D. Moule; *Can. J. Chem.* 40, 2057, (1962).
57. R.C. Mitchell, J.P. Simons; *Discuss. Farad. Soc.* 44, 208, (1967).
58. M. Bertogo, A.C. Cheung, C.H. Townes; *Astrophys. J.* 208, 914, (1976).
59. D.R. Flower; *Chem. Phys. Lett.* 67, 475, (1979).
60. R.W. Dixon, D. Field; *Proc Roy. Soc. A* 368, 99, (1979).
61. H. Kaplan, M. Shapiro; *Astrophys. J.* 229, L 91, (1979).
62. C. Ottinger, R. Velasco, R.N. Zare; *J. Chem. Phys.* 52, 1636, (1970).
63. S. Green, R.N. Zare; *Chem. Phys.* 7, 62, (1975).
64. a) T. Carrington, J.C. Polanyi, in MTP International Review of Science; J.C. Polanyi, ed., Vol. 9, Chap. 5; Butterworths, London, (1972).

64. b) I.W.M. Smith; Discuss. Farad. Soc. 44, 194, (1967).
65. a) D.D. Parrish, R.R. Herm; J. Chem. Phys. 49, 5544, (1968);  
51, 5467, (1969); 54, 2518, (1971).  
b) C.M. Scholeen, R.R. Herm; J. Chem. Phys. 64, 5261, (1976).
66. a) J.A. Coxon; J. Mol Spectros. 58, 1, (1975).  
b) J.A. Coxon, R.E. Hammersley; J. Mol. Spectros. 58, 29, (1975).  
c) M.A.A. Clyne, J.A. Coxon, A.R. Woon Fat; J. Mol. Spectros.  
46, 146, (1973).
67. G.H. Dieke, H.M. Crosswhite; J. Quant. Spectros. Radiat. Transf.  
2, 97, (1962).
68. J.M. Farrar, Y.T. Lee; J. Chem. Phys. 65, 1414, (1976).
69. W.L. Hase; Chem. Phys. Lett. 67, 263, (1979).
70. D. Setser; private communication, Feb., 1980
71. P.R. Brooks; Discuss. Farad. Soc. 55, (1973) and references therein.
72. D.S.Y. Hsu, G.M. McClelland, D.R. Herschbach; J. Chem. Phys. 61,  
4927, (1974).
73. D.S.Y. Hsu; Ph.D. Thesis, Harvard, (1974).
74. J. Cordova; Ph.D. Thesis, Massachusetts Institute of Technology,  
in preparation.
75. a) P.A. Giguere, I.D. Liu; Can. J. Chem. 30, 948, (1952).  
b) J. Howell, A. Olsen; J. Fluorine Chem. 12, 123, (1978).  
c) Comprehensive Inorganic Chemistry, Vol. 2, A.F. Trotman-Dickenson, ed.,  
Pergamon Press, New York, (1973).

## Appendix A. Orientation and Polarization Effects in LIF Experiments

This appendix is divided into four parts each of which considers one aspect of the orientation - polarization problem. The words orientation and alignment will refer to molecular properties while polarization will refer to the laser radiation. The first section will consider a general treatment of the dependence of absorption and emission matrix elements on orientation and polarization. The second section will consider the spatial distribution of radiation fields emanating from an oscillating dipole. The third and fourth sections will deal with aspects of these problems which directly pertain to the measurements discussed in Chapters III and IV.

The discussion is intended to be brief and it is assumed that the reader has some familiarity with texts such as references 27 to 30. In addition, a familiarity with reference 31 is necessary for section four. A variety of interesting papers are included in reference 32 which, along with references 33 and 34 should provide a good overview of experiments and theory that have dealt with oriented molecule considerations. The importance of measurements on oriented molecules has been mentioned in Chapters I and V and is discussed in references 35 and 36. As mentioned this discussion is intended to be brief - additional notes are available from the author and his thesis supervisor.

### 1. Transition Moment Dependence on Orientation and Polarization.

The matrix element describing the interaction of two states  $a$  and  $b$  with an external electromagnetic field is written as:  $\langle a | \underline{d} \cdot \underline{E} | b \rangle$ . Here  $\underline{d}$  is the molecular dipole moment and  $\underline{E}$  is the electric field of the radiation. Because the matrix element involves a dot product between these quantities any process involving the matrix element will depend on the orientation of the molecule relative to the electric vector. One can make use of the Wigner - Eckart theorem<sup>(37)</sup> to separate out the orientation dependent part of the matrix element:

$$\langle a | \underline{d} \cdot \underline{E} | b \rangle = \langle a | | d E | | b \rangle \begin{pmatrix} J_a & J_b & 1 \\ M_a & M_b & \mu \end{pmatrix} \equiv S(a,b) \begin{pmatrix} J_a & J_b & 1 \\ M_a & M_b & \mu \end{pmatrix}$$

where the quantity in parentheses is a 3j symbol. For a process which involves absorption of radiation followed by emission (i.e. LIF) one obtains a Breit formula such as equation 1 of reference 38 which tells us that the observed fluorescence intensity when one pumps with  $\mu$  polarized light from state a to state b which then fluoresces to state c and emits  $\mu'$  polarized light is given by:

$$I(a,b,c;\mu,\mu') \propto \nu_{bc}^3 S(a,b) S(b,c) \sum_{M_a} \sum_{M_b} \sum_{M_c} f(M_a) \begin{pmatrix} J_a & 1 & J_b \\ -M_a & \mu & M_b \end{pmatrix}^2 \begin{pmatrix} J_b & 1 & J_c \\ -M_b & \mu' & M_c \end{pmatrix}^2$$

Equation A-1.

where  $\nu_{bc}$  is the frequency of emitted light and  $f(M_a)$  is the fraction of molecules in the sublevel  $M_a$  of state a. From Equation A-1 it is obvious that fluorescence intensity is dependent on molecular orientation at least in a molecule fixed coordinate system. If we assume that the detected species are isotropically oriented in space (which is likely to be the case under our experimental conditions) then it is appropriate to set  $f(M_a)$  equal to a constant in Equation A-1. If absorption and emission were uncorrelated then we could sum over  $M_a$  and  $M_b$  and the M dependence would drop out by virtue of the unitary properties of the 3j's, and we would obtain:

$$I(a,b,c) \propto \nu_{bc}^3 S(a,b) S(b,c) \quad \text{Equation A-2.}$$

However, the absorption process prepares only a specific subset of  $M_b$  levels and so we must treat absorption and emission simultaneously. We find:

$$I(a,b,c) \propto \nu_{bc}^3 S(a,b) S(b,c) F(a,b,c) \quad \text{Equation A-3.}$$

The term  $F(a,b,c)$  comes from the dependence of the summation over the

product of  $3j$ 's on the absorption - emission branch being probed. Thus, even for an isotropic distribution the fluorescence intensity is sensitive to orientation - polarization terms in the matrix element. We have calculated the effects of  $F(a,b,c)$  on relative internal state, spin state and lambda state distributions and found a very small effect in the case of isotropically oriented molecules. Further details are given in section three of this appendix.

We have also performed extensive algebraic manipulations of Equation A-1 assuming an oriented sample. The work was aimed at developing an LIF probe of oriented molecules which could be expressed in terms of the moments of their  $M_a$  distribution in a space fixed coordinate system. The work was geared towards a Hund's case b molecule (i.e. OH, OD) and will not be detailed here.

## 2. Spatial Distribution of Emitted Fluorescence Intensity.

The spatial distribution of radiation is a function of the type of radiation (dipole, quadrupole...) and its state of polarization. The vector potential of a  $2^L$  pole field is given by:

$$\underline{A}_{-L}^M(\underline{e}) = \sum_{\lambda} c_{\lambda} \rho(kr) \underline{T}_{-L\lambda}^M$$

where  $M$  is the state of polarization,  $\lambda = L \pm 1$ ,  $\rho(kr)$  is a radial function describing the propagation of the wave and  $c_{\lambda}$  is an expansion coefficient. The tensors are defined as:

$$\underline{T}_{-L\lambda}^M = \sum_{\mu} C(L\lambda L; -\mu, M+\mu) Y_{\lambda}^{M+\mu}(\underline{r}) \underline{\xi}_{-\mu}$$

where  $C(L\lambda L; -\mu, M+\mu)$  is a Clebsch - Gordan coefficient,  $Y_{\lambda}^{M+\mu}$  is a spherical harmonic and  $\underline{\xi}_{-\mu}$  is a polarization vector. The vector potentials can then be written as:

$$\begin{aligned}
\underline{A}_1^M(e) = & (1/\sqrt{3}) \rho(kr) \{ [C(1,2,1;0,M) Y_2^M + \sqrt{2} C(1,0,1;0,M) Y_0^M] \underline{\xi}_0 \\
& + [C(1,2,1;-1,M+1) Y_2^{M+1} + \sqrt{2} C(1,0,1;-1,M+1) Y_0^{M+1}] \underline{\xi}_{-1} \\
& + [C(1,2,1;1,M-1) Y_2^{M-1} + \sqrt{2} C(1,0,1;1,M-1) Y_0^{M-1}] \underline{\xi}_1 \}
\end{aligned}$$

Equation A-4.

One can evaluate the above expressions for  $M=0, \pm 1$  and obtain the potentials in the  $\underline{\xi}_{0,\pm 1}$  basis or transform to a Cartesian basis  $\underline{\xi}_0 = \underline{\xi}_z$ ,  $\underline{\xi}_{\pm 1} = \mp (1/\sqrt{2}) (\underline{\xi}_x \pm i \underline{\xi}_y)$ .

Next we apply a rotation matrix to this arbitrary coordinate system and define the z direction as the propagation direction of the light:

$$\underline{A}_1^M = \sum_{\mu} a_{\mu}^M \underline{\xi}_{\mu} = \sum_{\mu} \sum_{\mu'} a_{\mu}^M d_{\mu\mu'}^1 \sigma_{\mu'} \equiv \sum_{\mu'} b_{\mu'}^M \sigma_{\mu'}$$

So that in this rotated coordinate system we have:

$$\underline{A}_1^1(e) \propto \left[ \exp(i\phi) \frac{(1+\cos\theta)}{2} \sigma_1 + \exp(i\phi) \frac{(1-\cos\theta)}{2} \sigma_{-1} \right]$$

$$\underline{A}_1^0(e) \propto \left[ \sin\theta / (\sqrt{2}) \sigma_1 - \sin\theta / (\sqrt{2}) \sigma_{-1} \right]$$

$$\underline{A}_1^{-1}(e) \propto \left[ \exp(-i\phi) \frac{(1-\cos\theta)}{2} \sigma_1 + \exp(-i\phi) \frac{(1+\cos\theta)}{2} \sigma_{-1} \right]$$

Using these equations we can determine the spatial distribution of light emitted from an oscillating dipole.

### 3. Effect of Transition Moment Orientation - Polarization Dependence on an Unoriented Sample.

We have utilized the considerations of parts one and two of this appendix to probe the influence of  $F(a,b,c)$  on the relative populations of internal, spin and lambda states. We consider the interaction of a vector potential,  $\underline{A}$ , for light of polarization  $\underline{\mu}_p$  with the initial state  $|\Psi(0)\rangle = |J_a M_a n\rangle$  where  $n$  indicates all non-explicit quantum numbers. Under the influence of electromagnetic radiation we will generate a superposition of final states  $|J_b M_b n'\rangle$  given by:

$$|\Psi'\rangle = \sum_{M_b} |J_b M_b n'\rangle \langle J_b M_b n' | \underline{A} \cdot \underline{d} | J_a M_a n \rangle .$$

Using equations 2.63, 2.65, 6.8 of reference 28 and 7.26, 7.32b, and 7.38 of reference 27 and treating only orientation dependent terms explicitly we have:

$$|\Psi'\rangle = \sum_{M_b} \sum_{M_a} \begin{pmatrix} J_b & 1 & J_a \\ M_b & M & M_a \end{pmatrix} |J_b M_b n'\rangle \mathcal{D}_{M_p}^1(\phi, \theta, 0)$$

which, for plane polarized light incident along  $z$ , becomes:

$$|\Psi'\rangle \propto \begin{pmatrix} J_b & 1 & J_a \\ M_b & 0 & M_a \end{pmatrix} |J_b M_a n'\rangle$$

Subsequent radiation can be treated equivalently to give the time evolution of  $|\Psi'\rangle$  as:

$$|\Psi'\rangle \propto \sum_{M'_c} \sum_{M_c} \sum_{M_b} \begin{pmatrix} J_b & 1 & J_c \\ -M_b & M' & M_c \end{pmatrix} \begin{pmatrix} J_b & 1 & J_a \\ -M_b & M & M_c \end{pmatrix} \mathcal{D}_{M_p}^1(\phi, \theta, 0) \\ \times \mathcal{D}_{M'_p}^1(\phi', \theta', 0) |J_c M_c n''\rangle .$$

Now we can define our coordinate system such that we need only consider right (+1) and left (-1) circularly polarized light. Then the total intensity of fluorescence at some angle  $\theta'$ ,  $\phi'$  is given by:

$$I(\theta', \phi') \propto \langle \dot{\Psi}' | \dot{\Psi}' \rangle \propto \begin{pmatrix} J_b & 1 & J_a \\ -M_b & 0 & M_a \end{pmatrix}^2 \sum_{M'_M_C} \sum_{M'_M_C} \begin{pmatrix} J_b & 1 & J_c \\ -M_b & M'_M_C & M'_M_C \end{pmatrix}^2$$

$$\times \{ |D_{M'_1}^1(\phi', \theta', 0)|^2 + |D_{M', -1}^1(\phi', \theta', 0)|^2 \}$$

Now, if we calculate the rotation matrices and write the full Breit formula:

$$I(J_a, J_b, J_c, \theta) \propto v_{bc}^3 S(a, b) S(b, c) (2J_b + 1)$$

$$\times \sum_{M_a} \begin{pmatrix} J_b & 1 & J_a \\ -M_a & 0 & M_a \end{pmatrix}^2 \{ (1/2) (1 + \cos^2 \theta) \begin{pmatrix} J_b & 1 & J_c \\ -M_a & 1 & M_a - 1 \end{pmatrix}^2 + \sin^2 \theta \begin{pmatrix} J_b & 1 & J_c \\ -M_a & 0 & M_a \end{pmatrix}^2$$

$$+ (1/2) (1 + \cos^2 \theta) \begin{pmatrix} J_b & 1 & J_c \\ -M_a - 1 & M_a + 1 \end{pmatrix}^2 \} .$$

By comparison to Equation A-3 one can determine the  $F(a, b, c)$  term which we have calculated for various values of  $J_a$ ,  $J_b$ , and  $\theta$ . Because our experiment does not resolve fluorescence,  $J_c$  is summed over allowed P, Q, R transitions. For relative internal state and spin state distributions of OH and OD (we use the  $R_1$  branch for internal states and the  $R_1$ ,  $R_2$  branches for spin states) the correction factor differs from unity by less than 0.5%. For the lambda state distributions, (Q and R



branches) the correction factor differs from unity by a few percent - well within the experimental error bars.

#### 4. Orientation - Polarization Effects and the FTDS Experiment.

In the FTDS experiment (discussed in Chapter IV) we probe the velocity vectors of product molecules as a function of angle of illumination of the scattering center. If there is a correlation between scattering angle and molecular orientation the Doppler profiles will be affected because the observed fluorescence intensity from molecules scattered into different angular regions will vary with the orientation of those molecules. In other words, the intensity observed due to the projection of the molecular velocities onto the axis defined by the propagation direction of the radiation will depend upon the projection of the molecular orientation onto the axis defined by the electric vector of the radiation. This problem is complicated from a practical point of view in that the final polarization of the radiation will depend upon its angle of incidence onto the mirrors which direct the beam.<sup>(50)</sup> Thus, as we move the mirrors to change the angle of incidence onto the scattering center we also change the polarization.

Under our experimental conditions it is highly unlikely that there is any preferential orientation of the detected species in a space fixed coordinate system. Nevertheless, we were interested in determining how much information about molecular orientation we could measure if the scattering center is illuminated from a single direction. If the orientation could be probed we, presumably, could fold any such effect into the interpretation of the Doppler profiles.

Basically, equation 2-26 of reference 31 tells us that for incident radiation whose polarization properties are indexed by a and b and for fluorescence polarization indexed by c and d, we can write the observed LIF intensity as:

$$I(a,b,c,d) = \sum_{M_{\mu}} C_{M_{\mu}} \Gamma(L\lambda, N\nu, M_{\mu}:a,b,c,d)$$

where the  $C_{M\mu}$ 's are coefficients which describe the molecular orientation (ie they are the coefficients of a spherical harmonic expansion). For electric dipole radiation, L and N can range from 0 to 2 and M ranges from 0 to 4. Each of the polarization indices can take on three values (0,  $\pm 1$  or x,y,z) which means that there are 81 different observable intensities which can be measured to determine the 25 possible  $C_{M\mu}$ 's, or in other words, the  $C_{M\mu}$ 's are overdetermined. However, if we limit ourselves to a given propagation direction, we limit ourselves to a subset of the measurable  $I(a,b,c,d)$ 's (polarization must be perpendicular to propagation direction) and we find that none of the  $C_{M\mu}$ 's can be uniquely determined. Thus a very extensive analysis would be necessary if we were to determine any scattering angle - orientation correlation.

APPENDIX B

Computer Programs

- 1) Focal routine for the calculation of prior distributions.
- 2) Focal routine for Doppler profile normalization and moment calculations.

0C-8K M0DV 11-219

01.01 T "PLANAR PRIORS FOR 0H AND 0D",!

01.02 T "TOTAL ENERGY = " ; A TOT

01.03 T !!!!!

01.05 Tz," K F1(K)

EXACT",!!!

01.10 F N=1,1,36 ; D 2

01.11 S 0=0D(1)-A

01.12 F N=1,1,36; S 0D(N)=0D(N)-0

01.15 F V=0,1,6 ; D 3

01.20 F N=1,1,36; D 4

01.21 T !!!!!!!!!!!!!!!!!!!!!!!

01.22 F N=1,1,36 ; D 9

01.30 Q

02.10 S 0D(N)=B\*((N+1)^2-1-0.5\*FSQT(4\*(N+1)^2+Y))

02.15 S 0D(N)=0D(N)-D\*(N+0.5)^4+A

03.10 S A(V)=123.26-0.191\*(V+0.5)

03.15 S V1(V)=1904.04\*(V+0.5)-14.1\*(V+0.5)^2

03.20 S V2(V)=1904.20\*(V+0.5)-14.075\*(V+0.5)^2

03.25 S B1(V)=1.72+0.0182\*(V+0.5)

03.30 S B2(V)=1.672+0.0171\*(V+0.5)

03.35 S Z1(V)=(A(V)/B1(V))\*((A(V)/B1(V))-4)

03.40 S Z2(V)=(A(V)/B2(V))\*((A(V)/B2(V))-4)

04.05 S SUM(N)=0.0 ; S R(N)=0.0

04.10 S S1(N)=0.0 ; S S2(N)=0.0

04.12 S L(N)=TOT-0D(N)

04.14 F V=0,1,6 ; D 5

04.16 F V=0,1,6 ; D 6

04.20 S SUM(N)=S1(N)+S2(N)

04.25 S SUM(N)=SUM(N)\*((2\*(N+.5)+1)^2\*(2\*N+1))

04.26 T z2.00," "N,z," "0D(N)," "SUM(N),!

05.10 F K=1,1,85 ; D 7

06.10 F K=1,1,85 ; D 8

CONTINUED

```

07.01 S P1=0.0
07.02 S N1(K)=B1(V)*((K+1)+2-1-0.5*FSQT(4*(K+1)+2+Z1(V)))
07.03 S N1(K)=N1(K)-10.2E-6*(K+0.5)+4+V1(V)-V1(0)
07.04 I (L(N)-N1(K))7.16,7.16,7.10
07.10 S P1=FSQT(L(N)-N1(K))
07.12 G 7.18
07.16 S P1(K)=0; S K=85
07.18 S S1(N)=S1(N)+P1
07.20 R

08.01 S P2=0.0
08.02 S N2(K)=B2(V)*(K+2-1+0.5*FSQT(4*K+2+Z2(V)))
08.03 S N2(K)=N2(K)-0.5E-6*(K+0.5)+4+V2(V)-V2(0)
08.04 I (L(N)-N2(K))8.16,8.16,8.10
08.10 S P2=FSQT(L(N)-N2(K))
08.12 G 8.18
08.16 S P2(K)=0; S K=85
08.18 S S2(N)=S2(N)+P2
08.20 R

09.10 S X1(N)=SUM(N)/SUM(18)
09.14 T %2.00,"      ",N,%6.05,"      ",SD(N),"      ",X1(N),I
*
```

C-8K MØDV 11-219

```
01.03 T "=====",!  
01.05 A W;T "EXP #";A W  
01.06 E  
01.07 T "   ANG ";A W;T "   "  
01.10 *  
01.15 A W  
01.20 I (W)1.15,1.15;S T=W  
01.30 F I=1,1,128;A S(I)  
01.35 A W  
01.40 F I=1,1,128;A M(I)  
01.45 *  
01.50 S MN=M(64);T %, "MN=",MN,!  
01.56 S CS=0;S MS=0;S MI=0  
01.60 F I=1,1,128;DØ 8  
01.65 T %4, "MAX1= ",M1, " AT",N1, "      TØTAL SPEC CØUNTS= ",%6,CS,!  
01.71 T %4.02, "MEAS TIME= ",T, " MIN      ",%, "MSUM=",MS,!  
01.72 G 3.1  
  
02.03 T !  
02.04 F J=1,1,5;S MØ(J)=0  
02.06 F I=1,1,43;D 6  
02.08 S MØ(1)=MØ(1)/MØ(5)  
02.10 F I=1,1,43;D 7  
02.11 S S2=FSQT(MØ(2)/MØ(5))  
02.12 S S3=MØ(3)/MØ(5);S SG=FSGN(S3)  
02.16 S S3=FLØG(FABS(S3))/3  
02.18 S S3=SG*FEXP(S3)  
02.20 S S4=MØ(4)/MØ(5)  
02.21 I (0-S4)2.22,2.22;S S4=0  
02.22 S S4=FSQT(FSQT(S4))  
02.24 T "N=",%5.00,MØ(5),!  
02.25 T "NO=",%5.03,MØ(1), "      S2=",S2,!  
02.28 T "S3=",S3, "      S4=",S4,!  
02.30 T "S4/S2=",S4/S2,!  
02.40 G 14.1
```

CONTINUED

```

03.10 F I=1,1,128; S M(I)=0
03.12 S S(129)=S(128)
03.14 F I=1,1,43; S M(I)=(S(3*I-2)+S(3*I-1)+S(3*I))/3
03.15 S N1=FITR(N1/3)
03.22 S K=N1-13; S L=N1+13
03.30 T "PEAK RANGE",%3,N1,"-",K,"=",N1-K," " ",L,"-",N1,"=",L-N1,!
03.32 S BK=0; S TL=0
03.35 F I=1,1,K-1; S BK=BK+M(I)
03.37 F I=L+1,1,43; S BK=BK+M(I)
03.39 S TL=K+42-L; S BK=BK/TL
03.41 T %6.02,"AV BK=",BK," " ",%3,TL,"BINS TØT BK",%6,BK*43,!
03.43 T "SPEC CØUNTS=",CS/3-(BK*43)," " "
03.45 F I=1,1,43; S M(I)=M(I)-BK
03.47 F I=1,1,K-1; S M(I)=0
03.49 F I=L+1,1,43; S M(I)=0
03.51 F I=K,1,L; I (M(I))3.55
03.53 G 3.57
03.55 S M(I)=0; T I,":":"
03.57 T I,"PUNCH??",A W
03.58 I (W)2.03,2.03,11.03

```

```

06.02 S MØ(5)=MØ(5)+M(I)
06.04 S MØ(I)=MØ(I)+M(I)*I
06.06 R

```

```

07.02 F J=2,1,4; S MØ(J)=MØ(J)+M(I)*(1-MØ(I))^J
07.04 R

```

```

08.10 S M(I)=(M(I)-1)/MN
08.20 S S(I)=(S(I)-1)/M(I)
08.30 I (S(I)-M1)8.6,8.4,8.4
08.40 S M1=S(I); S N1=I
08.60 S CS=CS+S(I); S MS=MS+M(I)
08.70 R

```

```

09.10 S .Z=FDIS(I*94.5,M(I)*YS)
09.20 F J=1,1,3; S W=W+1
09.30 R

```

CONTINUED

11.03 S Z=FNEW(2)  
11.10 F R=0,1,9;D 12  
11.15 T M(41)," ",M(42)," ",M(43),!  
11.20 S Z=FNEW(1)  
11.30 G 2.04

12.05 F X=1,1,3;D 13  
12.10 S I=4\*R+4  
12.20 T %4,M(I),!  
12.30 R

13.05 S I=4\*R+X  
13.10 T %4,M(I)," "  
13.20 R

14.10 T "YMAX=",%6,1.04\*(M1-BK)  
14.15 S YS=4095/(M1-BK)  
14.30 S Z=FDIS(4095,4095)  
14.33 T " PL0T??" ;A W  
14.35 I (W)1.03,1.03  
14.40 F I=1,1,43;D 9  
14.50 G 1.03

\*



APPENDIX C

Suppliers of Materials

1. Mirror Coatings  
Evaporated Metal Films  
701 Spencer Road  
Ithaca, New York 14850
2. High Intensity Lamps  
ILC Technology  
399 Java Drive  
Sunnyvale, California
3. Optics and Mounts  
Oriental Corporation  
15 Market Street  
Stamford, Conn. 06902
4. Phototubes  
EMI Gencon Inc.  
80 Express Street  
Plainview, New York 11803
5. Handheld Spectroscope  
Edmund Scientific Corporation  
7977 Edscorp Building  
Barrington, New Jersey 08007
6. Mercury Pen Light  
Spectronics Corporation  
956 Brush Hollow Road  
Westbury, New York 11590
7. Lenses  
Esco Optics  
171 Oak Ridge Road  
Oak Ridge, New Jersey 07438
8. Magnetic Tool Base  
Ralmike  
4405 South Clinton Ave.  
South Plainfield, New Jersey 07580
9. Gears  
Racks  
Pinion Wire  
Springs  
a) Chandler and Farquhar  
900 Commonwealth Ave.  
Boston, Mass. 02215  
b) Dynamic Gear Company  
175 Dixon Ave.  
Amityville, Long Island, N.Y.  
c) PIC Design  
P.O. Box 335  
Benrus Center  
Ridgefield, Conn. 06877
10. Cajons  
Swagelocks  
Cambridge Valve & Fitting  
50 Manning Road  
Billerica, Mass. 01821
11. Bellows  
Robert Shaw Controls Co.  
P.O. Box 400  
Knoxville, Tenn. 37919

- |   |  |
|---|--|
| 12. Ball Bearings                                 | Atlantic Bearing Company<br>65 Innerbelt Road<br>Somerville, Mass.                   |
| 13. O - rings                                     | I.B. Moore<br>30 Rindge Ave. Ext.<br>Cambridge, Mass.                                |
| 14. Vacuum Leak Sealant                           | Space Environment Laboratory<br>P.O. Box 1061<br>Boulder, Colorado 80302             |
| 15. Vacuum Guages                                 | Hasting-Raydist Inc.<br>P.O. Box 1275<br>Hampton, Virginia 23661                     |
| 16. Aquadag<br>(colloidal graphite<br>suspension) | Acheson Colloid Co.<br>Port Huron, Michigan 48060                                    |
| 17. Thermistors                                   | Newark Electronics<br>13A Wheeling Ave.<br>Woburn, Mass. 01801                       |
| 18. Heating Tape                                  | Fischer Scientific Co.<br>466 Riverside Ave.<br>P.O. Box 379<br>Medford, Mass. 02155 |
| 19. D/A Converter                                 | Datel Systems Inc.<br>1020 Turnpike St.<br>Canton, Mass. 02021                       |

BIOGRAPHICAL NOTE

The author was born in Cambridge, Massachusetts on January 3, 1955 and attended schools in Cambridge and Arlington. He graduated magna cum laude from Boston College in 1976 with a B.S. in Chemistry. While at M.I.T. he was a recipient of the John A. Lyons Memorial Fellowship. He is a member of Phi Beta Kappa and the American Physical Society.